Experimental and Computational Exploration of the Fracture Energy in Fiber Composites When Subject to Crack Parallel Compression

Jeremy Brockmann

A thesis
submitted in partial fulfillment of the
requirements for the degree of

Master of Science in Aeronautics & Astronautics

University of Washington

2022

Committee:

Marco Salviato

Francesco Deleo

Program Authorized to Offer Degree:
Aeronautics & Astronautics

University of Washington

Abstract

Experimental and Computational Exploration of the
Fracture Energy in Fiber Composites When Subject to
Crack Parallel Compression

Jeremy Brockmann

Chair of the Supervisory Committee:
Associate Professor Marco Salviato
Department of Aeronautics & Astronautics

This paper explores the global Mode I fracture energy of a carbon fiber composite subject to a biaxial stress state at a crack tip. Both an experimental campaign, in which a novel test setup for composite materials is designed and developed, and a computational campaign are performed to quantify the effects of the biaxial stress state. Using photomicroscopy (PMG) the results from these efforts are explained via meso-scale damage mechanisms at the crack tip. This research represents a gradational step in the continued development of composite fracture mechanics and, as a salient result, indicates the criticality of modeling fiber composites with a finite width fracture process zone (FPZ) and a fully tensorial damage law when simulating quasi-static fracture.

Experimentation is performed via a simple modification to the standard three-point-bend (3PB) test on a single edge notched bend (SENB) specimen. Polypropylene pads with a near perfectly plastic yield plateau are placed adjacent to the crack mouth and are used to apply a constant crack parallel compression prior to a bending moment which is induced by rigid rollers that are engaged only once the pads have yielded. Three different size test specimens, geometrically scaled in-plane and held at a constant thickness, are tested. A pre-impregnated, Toray T800H/3900-2 material

system is used, and composite panels are manufactured via hand layup, vacuum bagging, and autoclave curing processes. All test specimens are symmetric cross-ply laminates (comprised only of 0° and 90° plies). Cracks are installed into the specimens manually with a mitre box that guides a thin kerf blade (0.508 mm thick) to the desired crack length. Testing is performed on an Instron 5585H load frame where force data is obtained via a transducer on the load frame and displacement is measured through 2D digital image correlation (DIC).

The fracture energy is determined using Bažant's Type II Size Effect Law (SEL). From which it is found that there is a monotonic decrease in the Mode I fracture energy as the crack parallel compressive stress increases. Compared to the nominal value of fracture energy, where no crack parallel compression is applied, the fracture energy is observed to decrease by up to 37% for a compressive stress equal to 44% of the compressive failure limit of the composite. This weakening effect is attributed to splitting cracks that are induced at the crack tip due to the crack parallel compression. This is a novel result that challenges the century old hypothesis of fracture energy being a constant material property.

The experiments are also repeated computationally using finite element analysis (FEA) where two modeling approaches are employed. First, the Hashin damage criterion in conjunction with a crack band model and second, cohesive elements are used to define the crack band with a max stress damage criterion. When using the Hashin damage criterion in the crack band the weakening effect and decrease in fracture energy observed experimentally are accurately captured. Conversely, when cohesive elements and the maximum stress criterion model the crack band the simulations overpredict the fracture energy and are grossly off compared to the experimental results. This is explained by the complexity of the constitutive equations that govern damage initiation within the crack band. That is, the Hashin criteria is fully tensorial, including all experienced crack tip stresses in its failure calculation whereas the maximum stress criteria is a reduced tensorial damage law and the presence of a crack parallel compression is absent. This emphasizes the importance of using a crack band model coupled with a full tensorial damage law to accurately predict fracture in composites.

Table of Contents

List of Figures

List of Tables

Acronyms

3PB 3 Point Bend

4PB 4 Point Bend

ASTM American Society for Testing and Materials

CNC Computerized Numerical Control

DIC Digital Image Correlation

FEA Finite Element Analysis

FOD Foreign Object Damage or Foreign Object Debris

FPZ Fracture Process Zone

LEFM Linear Elastic Fracture Mechanics

PMG Photo Microscopy

QBFM Quasi-Brittle Fracture Mechanics

SEL Size Effect Law

SENB Single Edge Notched Bend

U.S. United States

Acknowledgements

Achievements such as a graduate degree seldomly come without the support of family, friends, and mentors. An abundance of aid was certainly the case during my graduate school tenure and there are many instrumental individuals to whom I owe thanks.

First, I would like to thank my advisor and committee chair Professor Marco Salviato. Professor Salviato is a constant encourager with high expectations for his students, pushing me to achieve many research milestones and hone my skills as a researcher and engineer. I came to graduate school to understand my intellectual capabilities and Professor Salviato's support led me to understand that I will only be limited by the barriers that I choose to place in front of myself. Professor Salviato also possesses an expertise in structures and mechanics which is coupled with kind mentorship and a willingness to teach anyone with the curiosity to learn. It is because of this that I am deeply appreciative to have worked under his guidance and I view him as a role model, I will draw often on the many lessons he taught me.

Similarly, I am indebted to Professor Francesco Deleo who served as my second committee member. Professor Deleo is a full-time practicing engineer who also leverages his expertise to teach graduate courses at UW. On top of this he volunteers his time to support and advise graduate students like myself. Professor Deleo's efforts in helping me graduate are much appreciated and specifically, his knowledge of finite element analysis which ultimately led to my research results being more accurate and of higher quality.

I also extend thanks to my fellow MAMs lab members who were always eager to help with my challenges. Most notably, Troy Nakagawa for his support with experimentation, Eunsik Phenisee for his computational support, and Seunghyun Ko for his lab leadership.

To my father, Ted Brockmann, and mother, Tammy Brockmann, I am eternally grateful for their incessant support and assistance throughout my entire life and specifically over the last 2 years of graduate school. I am extremely lucky to have 2 amazing parents.

Lastly, I would like to thank my girlfriend of 6 years, Ellie Komen, who provided constant love, unconditional support and understanding of my graduate workload, and perhaps the most impactful – making me many late-night meals while I studied.

Dedication

to my late brother Jason Brockmann, you are missed dearly

Page intentionally left blank

Chapter 1 Introduction

1.1 Composite Materials

A composite material, in the most general sense of the term, refers to a material comprised of two or more different constituent components bonded together. By this casual definition it is implied that virtually *all* materials are a composite. For example, at room temperature and pressure the nominal percent composition of water is 11.11% hydrogen and 88.89% oxygen by mass [1]. Though water is never referred to as a composite material in common language or scientific literature. Thus, to ameliorate this apparent misnomer, reference to a characteristic scale is introduced to the general definition. A more apt definition for a composite material is a material system comprised of two or more materials that are distinct at a physical scale greater than $\sim 1 \times 10^{-6}$ m and are bonded together at the atomic or molecular levels [2].

Within this specific definition of a composite material much diversity still exists although, for structural applications a few commonalities are present. Structural composites typically are a high strength, high stiffness reinforcing material embedded into a low strength, low stiffness matrix material. The combination of the reinforcing and matrix materials should then result in a composite material that is of greater properties than the two individual components. A common practice to partition the different types of composite materials is to the identify them based on the matrix material type. That is, metal, ceramic, or polymeric matrix composites. These types of composites are linked via definition, but they vary greatly in their applications and performance capabilities.

In this paper only polymeric matrix composite structures are considered where a carbon fiber reinforcing material is used. The extension of the results discussed herein would then be inappropriate to blindly apply to metal or ceramic matrix composites. Similarly, caution should be exercised when considering a polymeric matrix composite with a vastly different reinforcing material than carbon fiber. With this nuance in mind, there are points within this paper where *composite* is used as a stand-alone term. In these circumstances *composite* is intended to represent only a unidirectional carbon fiber reinforcement embedded in a polymeric matrix.

1.2 Carbon Fiber Composite Applications

Carbon fiber composites have experienced an exponential increase in their structural applications over the recent decades. They are found ubiquitously today in the aerospace [3], energy [4], automotive [5], recreational [6], and civil [7] industries. A primary driver for this phenomenon is a composites superior strength-to-weight ratio when compared to traditional metals such as steel, aluminum, and titanium. Furthermore, composites offer greater corrosion resistance, impact energy adsorption, and fatigue life while their mechanical properties are also tailorable.

The commercial flight industry is perhaps the domain that has seen the most dramatic uptick in structural composite use. The ever-increasing demand for lightweight and consequently fuel-efficient structures with high strengths and stiffnesses elicits composite materials as a clear front runner. As an example, Boeing's 787 and Airbus' A350 passenger vehicles are both comprised of ~50% composites by weight and ~80% by volume, values notably higher than previous generation aircrafts from these two aerospace giants [8]. In a similar fashion military aircraft have prospered from the stronger and lighter structures possible with a composite. Most notably, the B2 Stealth Bomber manufactured by Northrup and Grumman which has achieved unparalleled performance gains due to advancement with composites [9].

Similar growth is prevalent in all the aforementioned industries and, it is likely that due to their incredible potential composite materials will find utility in many new applications that are not yet considered. What is certain though, is that the market for composites will continue to grow and the demand for accurate and efficient composite design tools will grow with it. Towards this result, the present study is intended to contribute to engineers' understanding of composites and how they may be used to better meet our societal needs.

1.3 Supporting Fracture Theory

Fracture is a formidable problem that has been studied by engineers for over a century. Alan Griffith posited the first fracture mechanics concept, the Griffith energy balance, in 1921 and these concepts are still studied and applied today – this study included [10]. Many continued

lessons in fracture have unfortunately been learned through fatal accidents. Airline crashes [11], civil structure failures, and pressure vessel explosions [12] are examples. Advances in fracture theory function to mitigate these fatal occurrences but large financial impacts are also present. A famous economic study estimated that the annual cost of fracture in the U.S. in 1978 was $119 billion, ~4% of today's gross domestic product in the U.S., of which it was estimated that the cost could be reduced by $63 billion through current fracture resistant technologies and further fracture research [13]. Clearly fracture theory is imperative to guarantee safety and reliability in the increasingly complex technology of today.

1.3.1 Linear Elastic Fracture Mechanics

Initial fracture theory stemmed from what was of utility at the time. Infamously, a large number of U.S. manufactured Liberty ships fractured at sea in World War II [14]. This catapulted fracture into a full engineering discipline and decades of dedicated research were performed, eventually developing into what is known today as Linear Elastic Fracture Mechanics (LEFM). The concepts of LEFM are applicable only to materials that behave in an ideally brittle manner. The Liberty ships were made of steel and fracture occurred in frigid sea water hence, an ideally brittle assumption was appropriate. Additional foundational assumptions of LEFM are that any damage or plasticity that occur as a crack propagates are negligible in size compared to the structure size and the overall response of the structure is linear-elastic (i.e. Hooke's law defines the global stress-strain relationship) [15]. Stemming from this, cracks in LEFM are modeled as a line, mathematically having zero width and a crack tip radius equal to zero. Lastly, LEFM leverages a single parameter description of fracture. Most commonly the parameters critical fracture energy G_c or the critical stress intensity factor K_c are used to predict fracture and are assumed to be constant material properties. These parameters are unique to the mode of loading (see section 1.3.3) and are denoted in the literature accordingly as: G_{Ic}, G_{IIc}, G_{IIIc} or K_{Ic}, K_{IIc}, K_{IIIc}.

1.3.2 Quasi-Brittle Fracture Mechanics

The assumptions defining LEFM are often too restrictive to apply to many modern engineering materials. Specifically, when a material deviates from ideally brittle behavior LEFM is not applicable. This behavior was discovered in concrete and later extended

experimentally to shale, fiber composites, sea ice, rocks, ceramics, bone, and many more [16]. In these circumstances the material may exhibit a quasi-brittle behavior and hence a new fracture theory, Quasi-Brittle Fracture Mechanics (QBFM), is needed. The present paper focuses on QBFM as its assumptions are the most appropriate for fracture in composites [16, 17, 18, 19, 20, 21, 22, 23, 24, 25].

A key characteristic of QBFM is the size effect. The size effect is understood as a material's structural strength dependence on structure size. This is a departure from classical strength predictions such as plastic-limit or strength of materials analysis, which predict no size effect. On a very small scale quasi-brittle materials display pseudo-plastic behavior, on a medium scale they display quasi-brittleness, and on large scales they display closer to ideal brittleness. This transition in material behavior implies the presence of a non-negligible characteristic length of the material. This is taken to be the size of the Fracture Process Zone (FPZ). The FPZ is a large, non-linear region of damage that surrounds the crack tip during fracture in a quasi-brittle media. The concept of a FPZ is shown in Figure 1.1 for a concrete structure. LEFM theory does not account for the effects of a FPZ nor does it

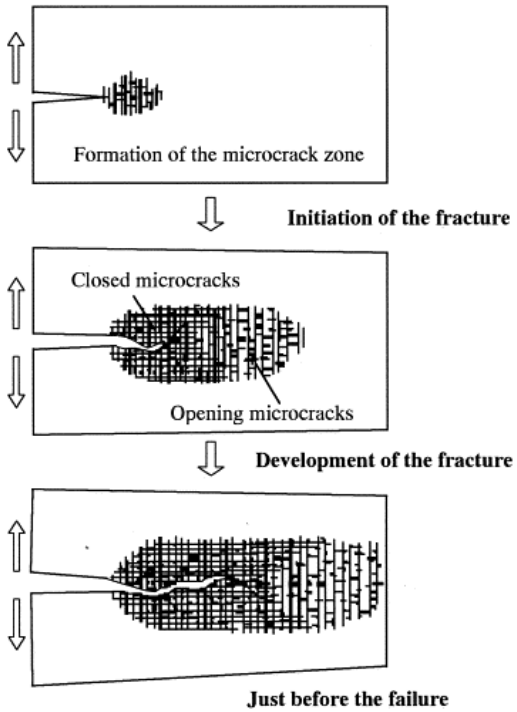

Figure 1.1 Concept of a fracture process zone in concrete. [26]

account for the transitional behavior of a quasi-brittle material. To define the size effect in quasi-brittle materials Bažant's Type II Size Effect Law (SEL) must be used [27]. The SEL is shown in equation (1.1)

$$\sigma_N = \sigma_o(1 + D/D_o)^{-1/2} \tag{1.1}$$

where D denotes a characteristic length, σ_N denotes structural strength, σ_o is an arbitrary measure of material strength, and D_o is a reference geometric size. Equation (1.1) may also be written in terms of more familiar fracture parameters as shown in equation (1.2).

$$\sigma_N = \sqrt{\frac{EG_f}{Dg(\alpha_o) + c_f g'(\alpha_o)}} \tag{1.2}$$

In this form E is the modulus of elasticity, G_f is the fracture energy, c_f is a measure of the fracture process zone size, $g(\alpha_o)$ is the dimensionless energy release rate evaluated at α_o, $g'(\alpha_o)$ is the derivative of g with respect to α evaluated at α_o, and α is the crack length normalized by D. A log-log plot of equation (1.1) is shown in Figure 1.2 with the size effect predictions of LEFM and strength criteria analysis superimposed. Notice that LEFM predicts a constant negative size effect with a slope of -1/2 while strength of materials analysis is a constant, both of which are inadequate to describe quasi-brittle materials at varying size scales [16].

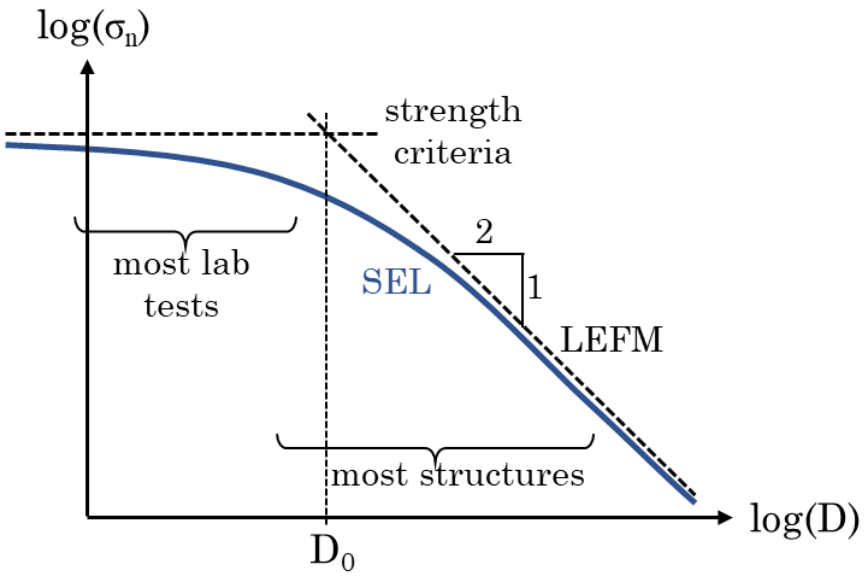

Figure 1.2 Graphical representation of Bažant's Type II Size Effect Law compared to LEFM and strength of materials criteria.

The Bažant SEL is one of the most critical conclusions of QBFM. It is used in the analysis section of this paper, and it dictates the type of experiments that were performed. Size effect testing is a general term that has been adopted to indicate an experimental and analytical method that leverages equation (1.2).

1.3.3 Fracture Modes

Within LEFM, QBFM, and all fracture theories, different modes of fracture exist. Fracture modes refer to the decomposition of the crack tip stresses into individual stress components. There are 3 distinct modes of fracture currently: Mode I – opening, Mode II – in plane shear, and Mode III – out of plane shear, which are illustrated in Figure 1.3. Most materials behave differently under different modes of loading and consequently the fracture behavior of a structure under Mode I, II, or III will differ substantially [15]. In practical applications Mode I is the most prevalent form of loading and crack propagation, thus a majority of fracture research has gone into characterizing the Mode I performance of many engineering materials while Mode II and III are less explored [28]. For the present study an investigation of Mode I is also adopted without any palpable work directed towards Modes II or III. As a remark,

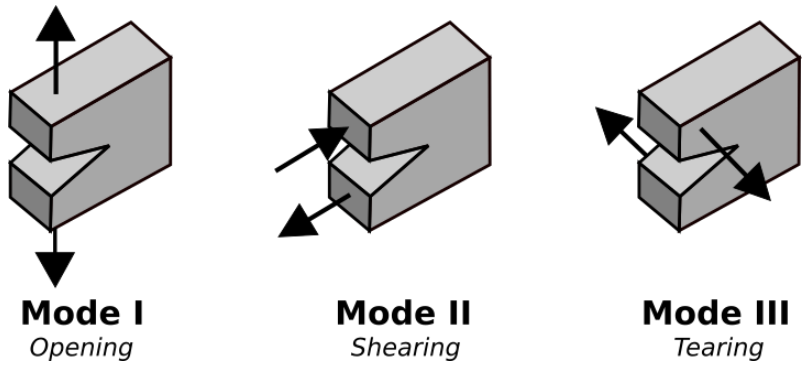

Figure 1.3 The three distinct modes of fracture applied to a cracked structure. [29]

the reader is encouraged to exercise caution when referring to strictly Mode I, II, or III in a composite material. Whilst a composite structure may undergo a Mode I loading condition at the macroscopic level, the stresses at the crack tip, on a microscopic level, are almost certain to be representative of a mixed-mode loading condition. This is due to the damage that

accompanies fracture in quasi-brittle materials and the anisotropic behavior of composites in general. As a consequence of this behavior, Mode II and III loading are inherently more important in composite structures in comparison with metallic structures. Nonetheless, an investigation of the micro-scale stresses, or mixed modality, at a composite crack tip is not included in the present study but it must be understood that the distinction between fracture modes can vary simply by nature of the scale at which the structure is analyzed. In the ensuing chapters Mode I is referred to in a global sense, but it is incorrect to assume that the micro-scale stresses are purely Mode I.

1.4 Thesis Motivation and Goal

All existing fracture theories rest upon a century old hypothesis that a material's critical fracture energy is constant [10, 15], being defined as a material's resistance to crack propagation. This is of great utility for the practicing engineer as the fracture energy may be calculated for a structure, either computationally or through classical analytical solutions, and simply compared against the known and constant fracture energy of the material. If the structure's fracture energy is larger than the material property, crack propagation is expected and if it is lower, no propagation is expected. This is known as the single parameter description of fracture, and it is generally accepted within LEFM [15].

One attributor to constant fracture energy is the modeling of a crack as a line, as done in LEFM. When line crack models are used the crack may only be opened via the 3 modes shown in Figure 1.3. If a planar biaxial stress state is then considered, in which one stress component is perpendicular to the crack plane and one is parallel, the parallel stress has no ability to open the crack. The biaxial stress state is thus equivalent to a uniaxial stress state, at least regarding fracture, when a line crack model is used. This is illustrated in Figure 1.4 where any damage or plasticity at the crack tip is considered negligibly small according to LEFM. So, because the X direction line crack in Figure 1.4 has no change on σ_{xx}, the biaxial stress state has no impact on the structure's ability to resist fracture. Thus, it is concluded that the fracture energy is constant under the shown uni-axial and bi-axial stress states.

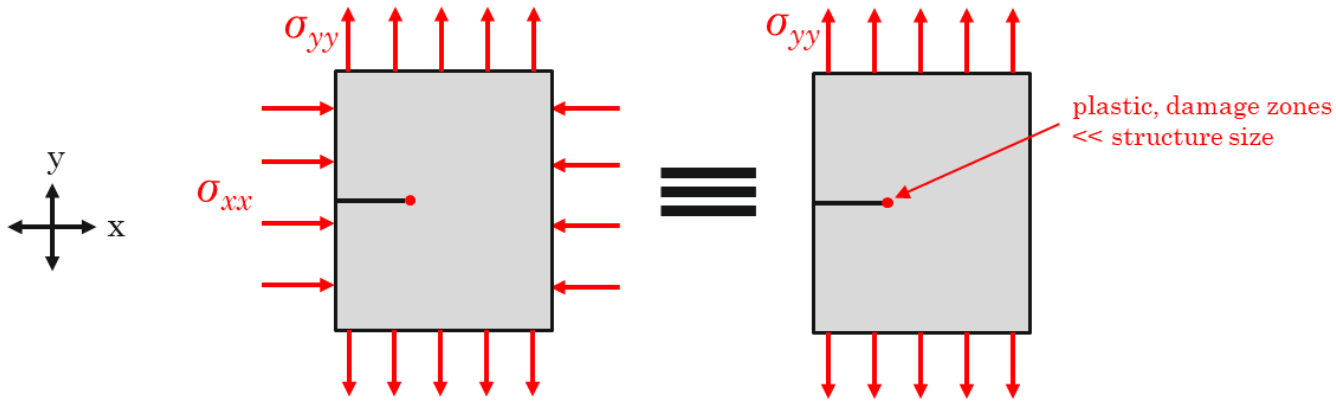

Figure 1.4 Equivalence of a biaxial and uniaxial stress state, regarding fracture behavior, according to the assumptions of LEFM.

In the presence of a finite width FPZ, as is the case for a quasi-brittle media, the assumption of a line crack breaks down. Consider again the stress state shown in Figure 1.4 but with the inclusion of a FPZ that is non-negligible compared to the structure size. This is shown in Figure 1.5. Now, because the FPZ has a non-negligible width in the x direction, the stress σ_{xx} that is parallel to the crack plane will have an influence on the crack opening behavior. Meaning the stress state is not equivalent to that of a uni-axial stress state, as was the case for the LEFM assumption in Figure 1.4. This has 2 novel consequences. First, it implies that a crack may propagate by way of a fracture mode that is not defined by Mode I,

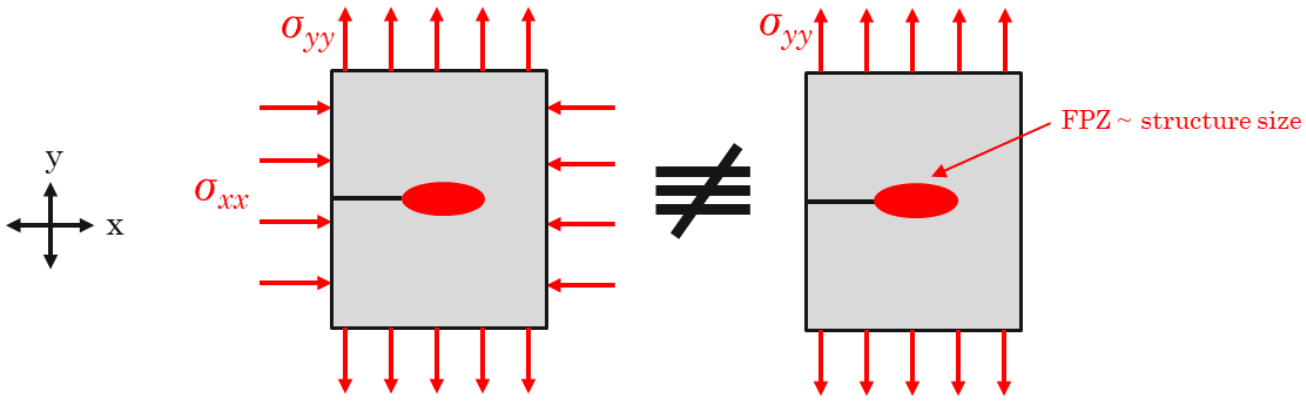

Figure 1.5 Influence of a finite width FPZ on a quasi-brittle material under a biaxial stress state.

II, or III. Second, because the crack parallel stress σ_{xx} will influence the structure's ability to resist fracture, the fracture energy is likely to be non-constant. This conclusion posits an intriguing question that governs the present study: *does the presence of a crack parallel stress influence the constancy of a composites fracture energy?* Existing literature is completely deficient to answer this question for composite materials and hence an opportunity to explore an unexplored behavior exists.

Using this motivation, a thorough experimental and computational effort is undertaken. Specifically, the influence of a crack parallel compression in conjunction with a bending moment is used as the catalyst for investigation. In Chapter 2 the details of this novel experiment and its design for composite materials are discussed. The manufacturing techniques used to build the test coupons are also included here. In Chapter 3 the efficacy of the proposed test method is evaluated. As the experiment is novel for composites, and not defined by an existing standard such as ASTM, three iterations of design updates were required to obtain acceptable data. Lessons learned from this effort are discussed here. Additionally, the experimental data is presented and analyzed via Bažant's SEL. The observations made from the experimental data are then explained via photomicroscopy of the crack tip on the experimental coupons. In Chapter 4 details of the computational work are presented, analyzed, and compared against the experimental data. Chapter 5 then summarizes the key conclusions from this study and its implications for composite structures in industry.

1.5 Literature Review

Due to the novelty of the ideas posed in section 1.4 the existing academic literature is absent in relevant studies on composite materials. But a trailblazing study was performed by a team of researchers at Northwestern University in 2020 where an equivalent experiment was performed on concrete specimens [30, 31]. Concrete is known to behave in a quasi-brittle manner and hence these studies are tantamount to a composite study. Much inspiration in this study is drawn from the efforts and results of the concrete studies at Northwestern.

1.5.1 Effects of Crack Parallel Compression in Concrete

The studies performed at Northwestern University investigated the same stress state as the one proposed in 1.4, a crack parallel compression with a bending moment whose normal stresses open the crack via Mode I fracture. To accomplish this, they employed a simple modification to the standard 3PB test where a polymer pad with a perfectly plastic yield plateau is used to generate a crack parallel compression. The test specimen is placed atop the pads which are designed in such a way that they yield completely prior to engaging rigid rollers that induce a bending moment [30]. A schematic of this test procedure is shown in Figure 1.6. These researchers dubbed this experiment as *The Gap Test*, seemingly due to the simplicity of taking a standard 3PB test, adding a gap between the specimen and the rollers with the perfectly plastic pads, and then using the results from such to draw novel and impactful conclusions. Out of respect to the original researchers the nomenclature of *Gap Test* is also adopted in this study to describe the equivalent experiment shown in Figure 1.6 but for composites.

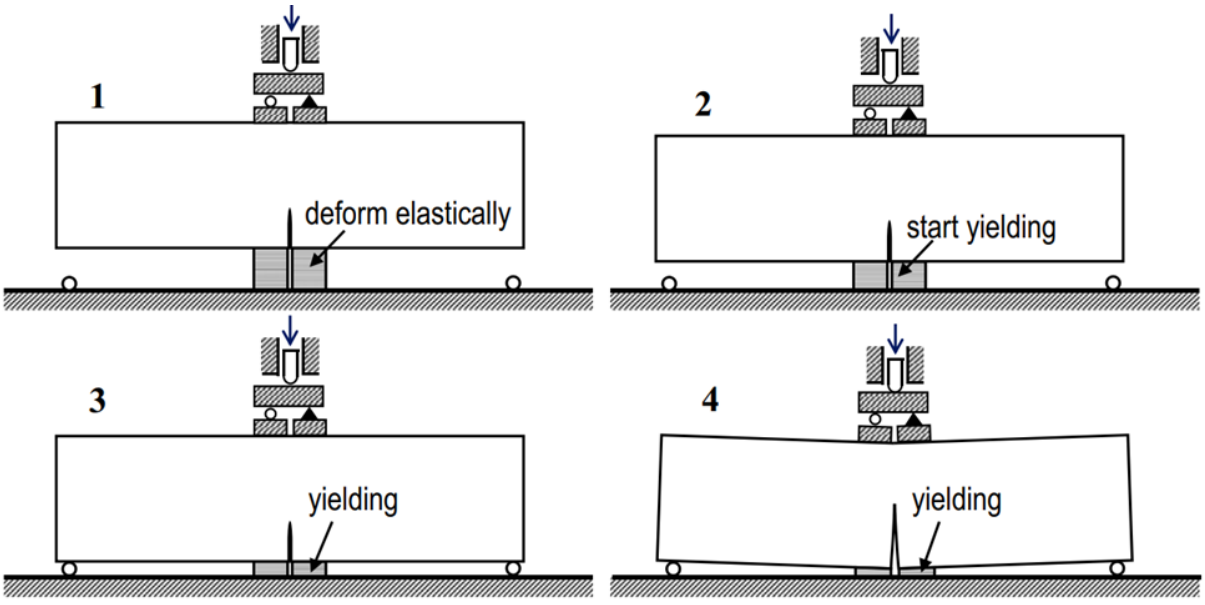

Figure 1.6 Experimental setup used on concrete specimens by [30, 31].

The results from the Northwestern studies suggest that concrete exhibits a non-constant fracture energy when subject to a crack parallel compression. Specifically, they observed that, depending on the level of compression applied, the fracture energy can increase up to 1.8 times the nominal Mode I fracture energy or reduce it to almost zero as the compression level approaches the compressive strength of the structure [30]. A similar trend

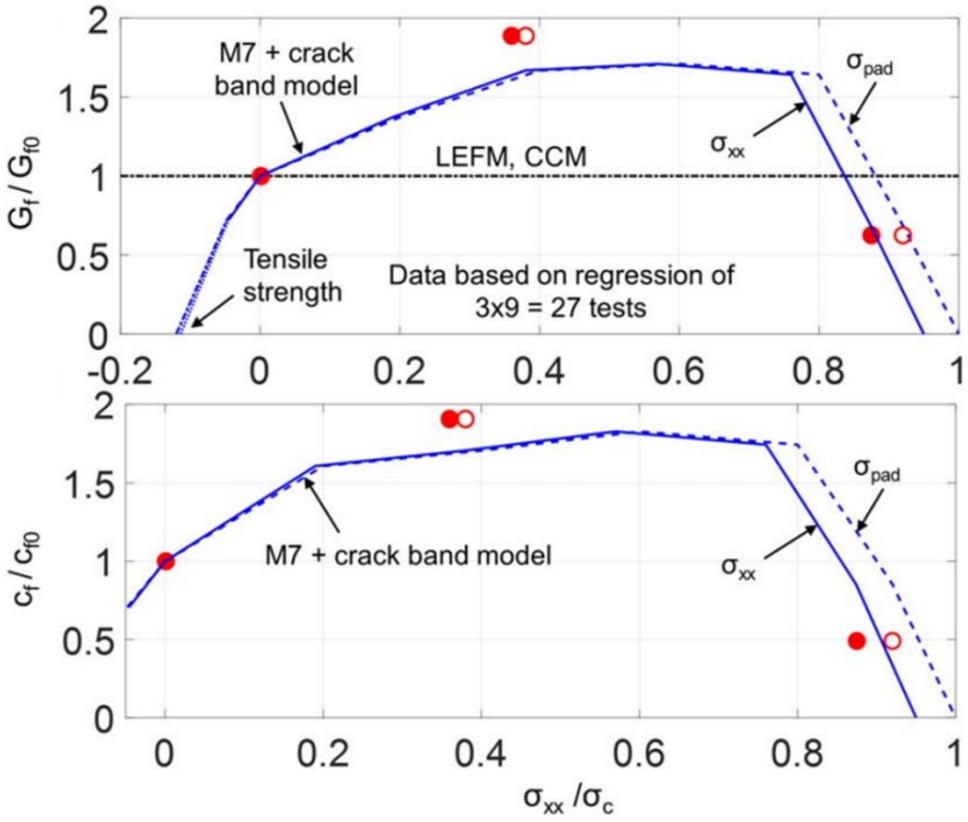

Figure 1.7 Gap Test results from [30] on concrete specimens. The red dots indicate experimental data whereas the blue curves are FEA results. G_f denotes fracture energy, G_{fo} is the fracture energy with no crack parallel compression, c_f a measure of the FPZ size, c_{fo} is the FPZ with no crack parallel compression, σ_{xx} is the crack parallel stress level, and σ_c is the compressive strength of the material.

is observed for the c_f value, which is a measure of the FPZ size. These results are shown graphically in Figure 1.7. The variations in the concrete fracture energy are explained via microstructural damage mechanisms. For the initial rising portion of the curve in Figure 1.7

the crack parallel stress is believed to increase the concrete's resistance to slip on microcracks that are inclined with respect to the direction of the macrocrack propagation and also grain interlock that is enhanced by surface roughness [31]. These features indicate why an initial strengthening effect is observed for moderate crack parallel compression. To explain the second, decreasing, portion of the curve it is proposed that the higher crack parallel stresses overcome the friction and slip resistance that initially strengthens the fracture energy and instead now leads to lateral expansion and eventual axial splitting of microcracks [30, 31].

1.5.2 T-Stress

The main parameters of LEFM are based on an infinite plate assumption, implying no boundary effects on the stress state at the crack tip [15]. But when corrections to these parameters are made for a finite dimension plate, in which boundary effects may be present, a parameter known as the T-stress becomes relevant. The T-stress is typically used as a measure of plastic constraint at the crack tip in a ductile metal and it may be measured experimentally or computationally [32]. Depending on the geometry of the finite plate (or structure) the T-stress term may act like a crack parallel stress which has been alluded to in the conceptualization of the Gap Test. Thus, it may appear that crack parallel stress, disguised as T-stress, is a known concept that has been researched with the origination of LEFM and consequently the Gap Test could yield trivial results or, the conclusions to draw from it have already been made. This concern is not legitimate for two reasons. First, the effects from a T-stress are small in comparison to the crack parallel stresses applied in the Gap Test, never approaching the failure limit of the material. Second, and more forcefully, the concept of T-stress was derived for an isotropic, linear-elastic, and metallic material meaning it is not transplantable to quasi-brittle materials in which the physics and governing material behavior are different [31].

Chapter 2 Experiment Design and Manufacturing

2.1 Objective and Considerations

This project seeks to explore the fracture behavior of composites that are subject to a biaxial stress state in which one stress component is parallel to a crack. By the logic put forth in section 1.4 it is believed that the fracture energy will fluctuate based on the level of biaxiality. Additionally, it appears that the crack parallel stress that is applied may be tension, compression, shear, or a mixed load, and an effect on the fracture behavior will be observed. Due to the novelty of the Gap Test a simple crack parallel compressive stress is chosen for experimentation on composites, like that of [30, 31]. Further, the experimental setup used in the concrete studies at Northwestern, shown in Figure 1.6, will serve as the backbone of the setup used to test on composites.

In adapting the Gap Test for composites, a key difference between concrete and composites must be considered – the characteristic thickness. Concrete is typically a thick, brick like structure whereas composites are thin, shell-like structures. The behavior of a thin structure under compression is subject to buckling failure, an abrupt out of plane displacement due to an in-plane load, while a thick structure is likely to fail due to compressive damage prior to buckling. Buckling failure will impugn the results of the composite Gap Test and hence the test specimens must be designed to mitigate such. The composite Gap Test will also leverage size effect testing, meaning equation (1.2) is the primary means of analysis. This allows for evaluation of fracture properties as a function of size [33], a governing characteristic of QBFM. Test specimens that are scaled in-plane by values of 1:2:4 will be used while the thickness is held constant. The Gap Test effects on specimen thickness certainly may also be investigated using equation (1.2), though such an endeavor is not performed currently due to the substantial amount of added manufacturing and experimental time it would incur. Also, using pads in the Gap Test that have a near perfectly plastic yield plateau is imperative to the test's success. In [30, 31] polypropylene pads are used. Polypropylene is a cheap and readily available material in the location in which the composite Gap Tests were performed, Seattle, WA, and hence polypropylene is also used. Lastly, the Gap Test requires a single edge notched bend (SENB) specimen that is cracked to a pre-determined length. In metallic materials this is traditionally accomplished

via fatigue pre-cracking [34], although fatigue pre-cracking is much more difficult in composites and can prove to be prohibitive timewise. Cracks are thus installed manually with a thin kerf blade. The execution and details of these experiment design considerations are explained and illustrated in the ensuing sections of this chapter.

2.2 Buckling Analysis

The first design detail to resolve is the geometric dimensions of the test specimens, of which there will be 3 different sizes which are scaled in-plane by 1:2:4. A schematic showing the dimensions to be determined is shown in Figure 2.1. During the Gap Tests fracture is considered a successful test whereas buckling is considered a failure. This imposes a simple design criterion

$$P_{fracture} < P_{buckle} \tag{2.1}$$

that is used to determine the dimensions in Figure 2.1. The dimensions a, L, and D are analyzed parametrically while the thickness t is left as an independent variable to find a

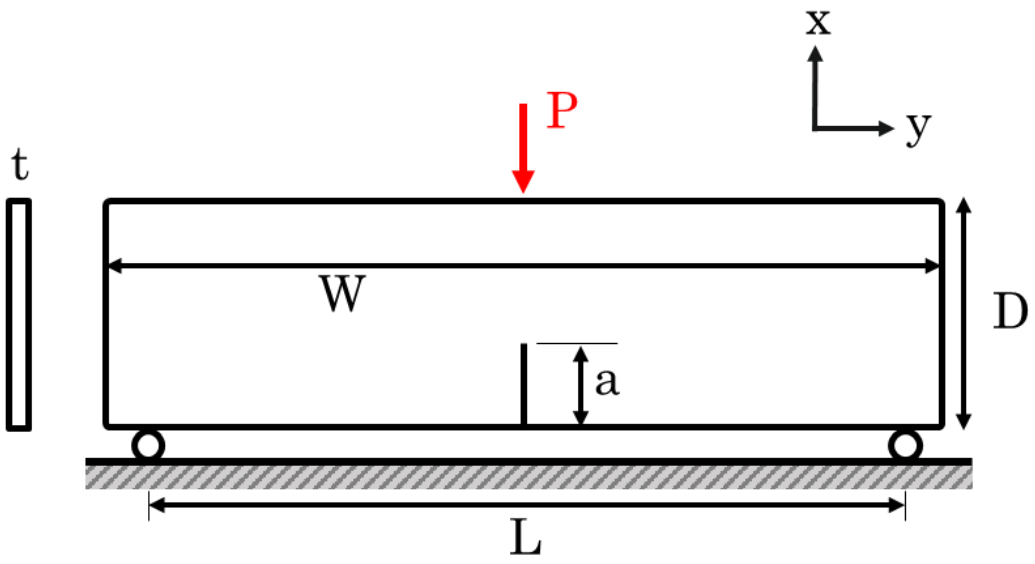

Figure 2.1 Gap Test schematic showing the test specimen geometry.

geometry that satisfies equation (2.1) for the largest test specimen size. Buckling is a phenomenon that increases in likelihood for structures with greater aspect ratios so, it is

sufficient to investigate equation (2.1) for the large size specimen only and the resulting smaller 2 specimen sizes will not be at risk of buckling.

To predict the fracture load in equation (2.1) an expression from LEFM is used.

$$\sigma_N = \sqrt{\frac{EG_f}{Dg(\alpha_o)}} \tag{2.2}$$

LEFM is only loosely applicable to composites and hence equation (2.2) is taken as a first order approximation of the fracture load. For the loading case applied in Figure 2.1 the relation between the critical fracture stress and the fracture load is found via beam theory,

$$\sigma_N = \frac{3PL}{2D^2t} \tag{2.3}$$

Combining equation (2.2) and equation (2.3) then gives the expression for the desired fracture load.

$$P_{fracture} = \frac{2D^2t}{3L}\sqrt{\frac{EG_f}{Dg(\alpha_o)}} \tag{2.4}$$

The critical fracture energy G_f that causes failure according to LEFM is assumed to be G_f = 88.4 N/mm per experiments performed on a 2x2 twill composite [35]. The dimensionless energy release rate $g(\alpha_o)$ is determined per equation (2.5) in conjunction with a finite element analysis (FEA). The value $g(\alpha)$ relates the geometric and elastic parameters of a structure to the fracture energy G_f [17].

$$g(\alpha) = \frac{G(\alpha)E}{D\sigma_N^2} = \frac{JE}{D\sigma_N^2} \tag{2.5}$$

To provide accurate FEA results the J-integral method [36] and quarter element technique [37] is employed in Abaqus Standard-Implicit 2020.

The buckling load in equation (2.1) is predicted using an eigenvalue buckling analysis in FEA. This method functions via a linear perturbation technique that determines the loads for which the model stiffness matrix becomes singular [38], solving the classical eigenvalue problem shown below.

$$(K_o + \lambda_i K_\Delta)v_i = 0 \tag{2.6}$$

K_o is the stiffness matrix of the unperturbed model, K_Δ is the is the stiffness matrix of the model due to an incremental load (i.e. perturbation), λ_i is the eigenvalue which corresponds to a buckling load, and v_i is the eigenvector which corresponds to the buckling mode [39]. This solution method can also determine higher buckling modes and loads though, for the present purposes only the first buckling mode/load is of concern and hence the higher modes/loads can be neglected. Eigenvalue buckling analysis is a built-in feature in Abaqus 2020 making it an accurate analysis tool that requires minimal development effort.

Both the fracture and buckling analyses are dependent upon the composite material system's mechanical properties and the laminate stacking sequence. The present study uses a symmetric cross-ply laminate (0° and 90° layers only) and a Toray T800H/3900-2 material system whose material properties are shown in Table 2.1. The fracture load predicted via

Elastic Properties (GPa)		Strength Properties (MPa)	
E_{11}	152.4	X_T	2089.0
E_{22}	9.205	X_c	1482.0
G_{12}	4.275	Y_T	79.29
v_{12}	0.35	Y_C	231.0
ply thickness = 0.2 mm		S	132.8

Table 2.1 Mechanical properties of a Toray T800H/3900-2 uni-directional lamina per [40].

equation (2.4) requires the effective modulus of elasticity at the laminate level, not lamina as given in Table 2.1. To determine the effective modulus of the laminate classical lamination theory is used [2] and, referring to Figure 2.1, the laminate modulus in the y direction is used, which is in the direction of the normal stresses induced from the bending moment.

Executing this analysis results in the comparative plots shown in Figure 2.2 and Figure 2.3. Note that for geometries (a)-(c) there are no permissible thicknesses that satisfy equation (2.1). The geometry in (f) is chosen for the largest test panel as it is the most robust against buckling at the smallest thickness. Also, due to the fracture load being based on LEFM analysis, making it only an approximate prediction, the thickness is chosen such that the fracture load is one half of the buckling load. From (f) this yields a thickness of t = 7.6

mm which, based on a cured ply thickness of 0.2 mm [41], indicates a 38-ply laminate. The resulting geometries of all 3 test panel sizes are shown in Table 2.2.

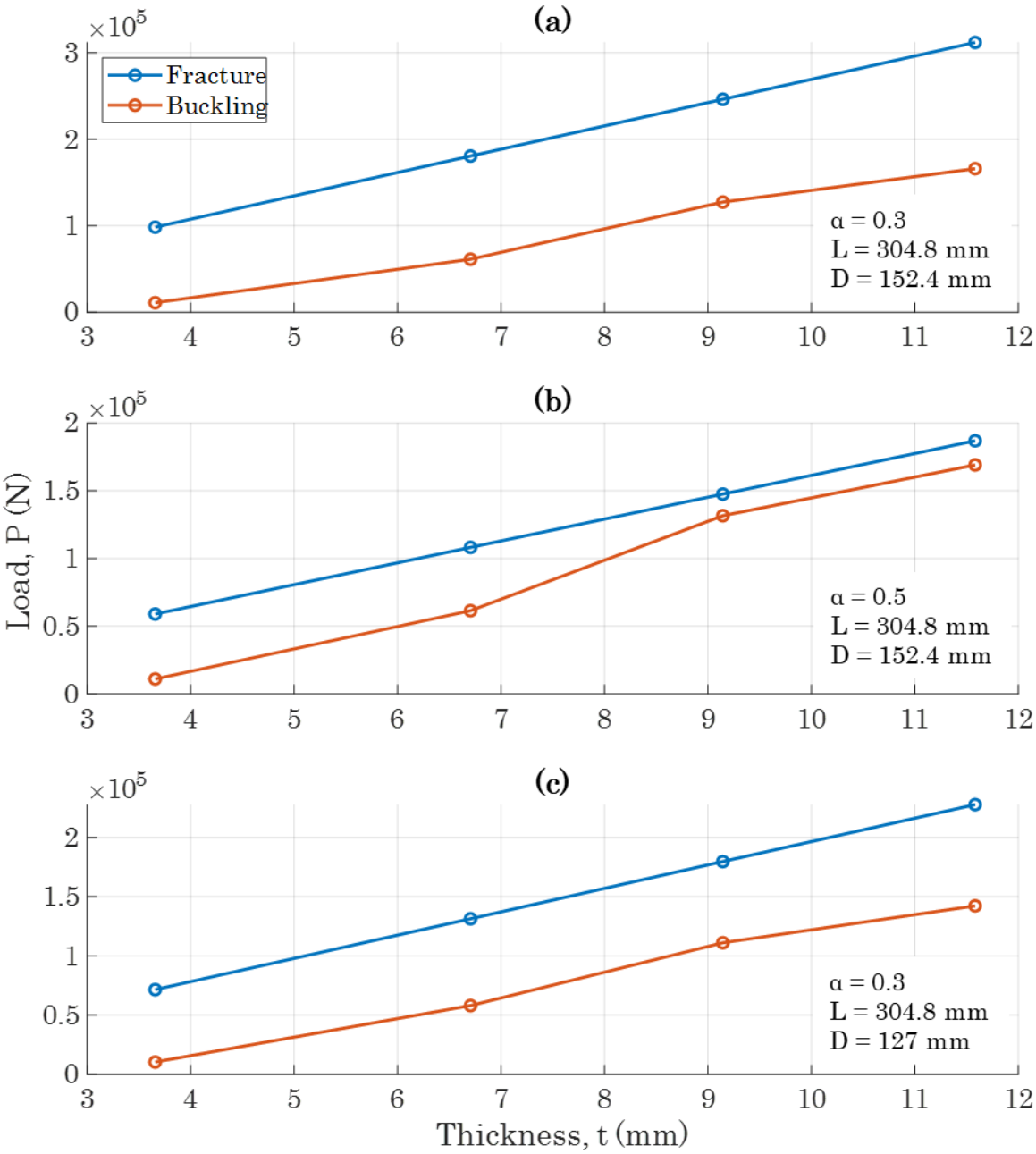

Figure 2.2 (a)-(c) Predicted buckling versus fracture loads using equations (2.4) and (2.6) for various panel designs. Normalized crack length α = a/D.

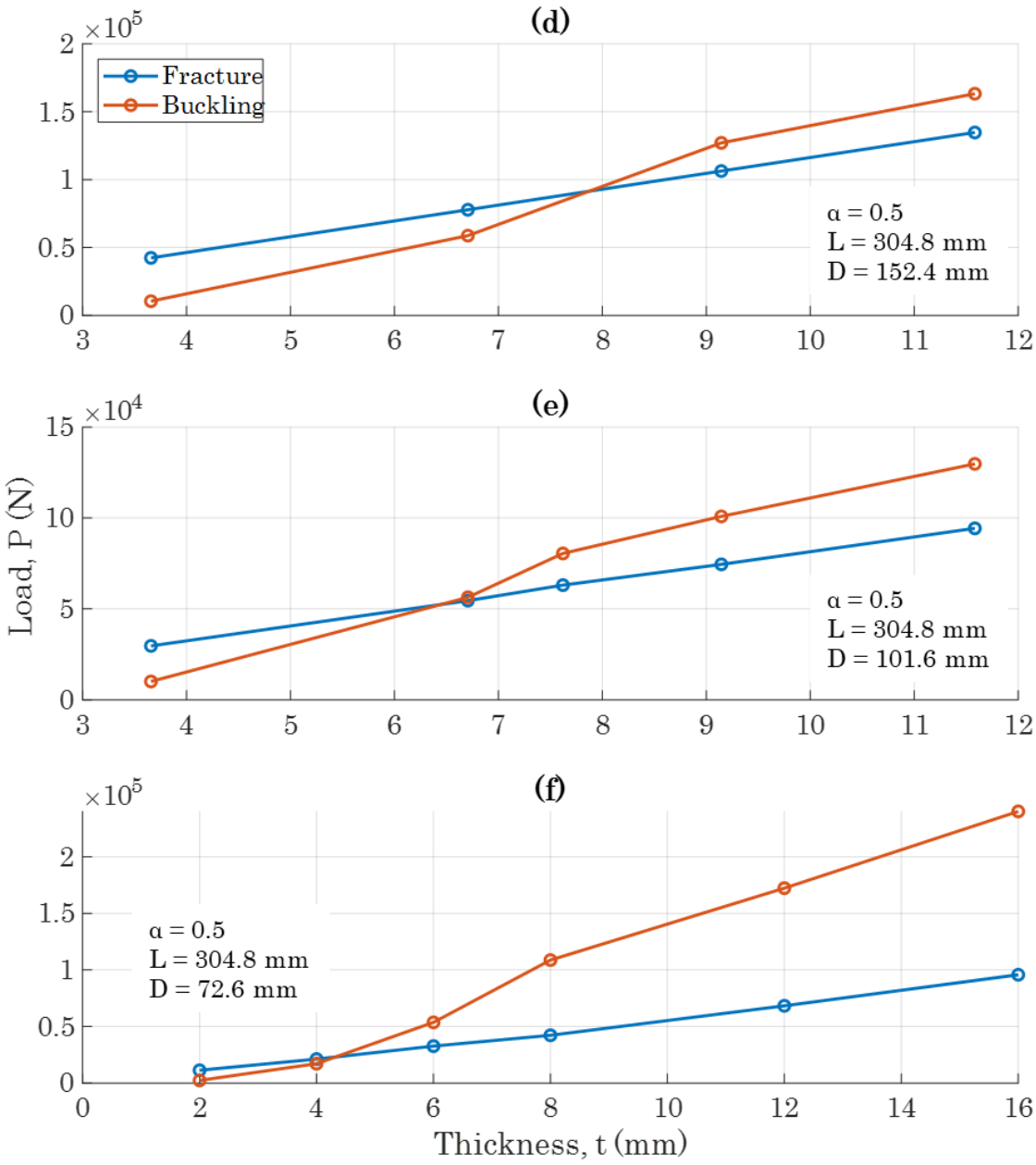

Figure 2.3 (d)-(f) Predicted buckling versus fracture loads using equations (2.4) and (2.6) for various panel designs. Normalized crack length α = a/D

Panel Type	Panel Width, D (mm)	Roller Span, L (mm)	Panel Length, W (mm)	Crack Length, a (mm)
Small	19.05	76.2	83.82	9.525
Medium	38.1	152.4	165	19.05
Large	76.2	304.8	335.28	38.1

*thickness, t = 7.6 mm for all panels

Table 2.2 Test panel dimensions based on Figure 2.1 geometry.

(Referring to Figure 3.16, the polypropylene geometry that will be used in this study is s = 12.7 mm for small specimens, which is scaled by 2 and 4 for the medium and large specimens, respectively, while w is fixed at 25.4 or 38.1 mm depending on the compression level)

2.3 Mechanical Test Fixture

As this study focuses on an avant-garde experimental technique all of the necessary test fixturing is not readily available to execute the Gap Tests. Though, composites are often tested via flexure methods [42] and hence an existing text fixture can be modified to accommodate the specific needs of the Gap Test. The fixture used to perform 3PB tests within the UW Mechanical Test Laboratory is shown in Figure 2.4, this is the fixture that will be modified for Gap Testing.

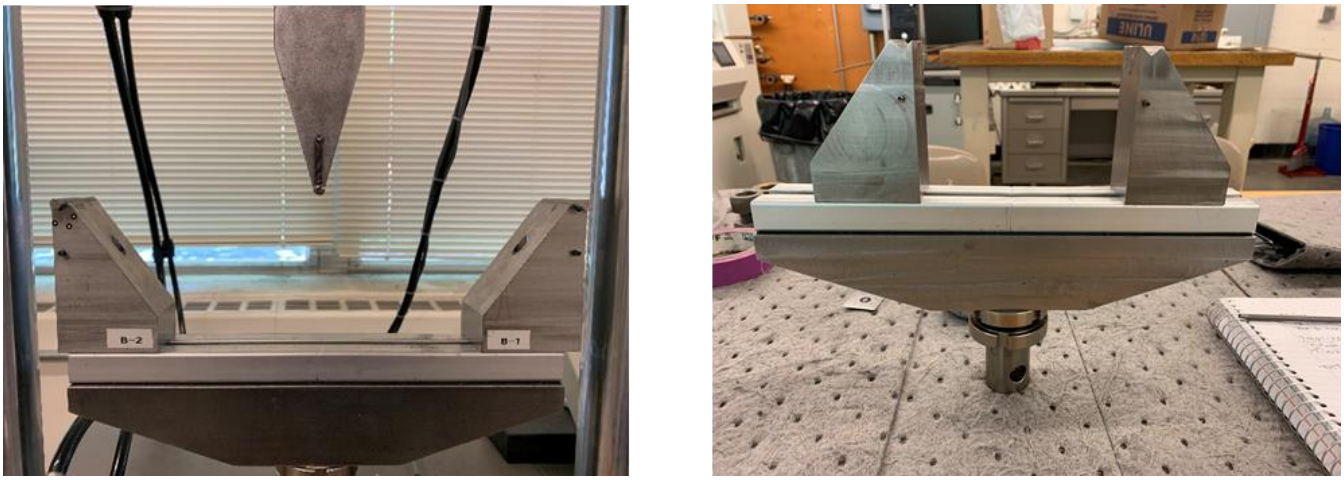

Figure 2.4 Existing 3PB test fixture in the UW Mechanical Test Laboratory that is to be modified for Gap Test use.

The primary nuance of the Gap Tests is the plastic pads that are used to apply the crack parallel compression. A polypropylene material is selected for the pads which, at the time of writing this thesis, may be purchased from McMaster-Carr in a 152.4 mm by 304.8 mm sheet that is 12.7 mm thick for $19.81 (McM #8742K129) – a very economical material for testing (even despite the polypropylene pads plastically deforming during testing and hence being single use only). Based on the efforts by [30, 31] it is known that polypropylene exhibits a near perfectly plastic yield plateau but, the plateau stress and strain must be known to use the polypropylene in a design sense. To obtain these values the ordered polypropylene is tested in accordance with ASTM D695 Standard Test Method for Compressive Properties of Rigid Plastics. ASTM D695 recommends a square test specimen that is 12.7 by 12.7 by 25.4 mm loaded between 2 flat and parallel anvils at a constant displacement of 1.27 mm/min [43]. This experimental setup is shown in Figure 2.5 and the corresponding data in Figure 2.6.

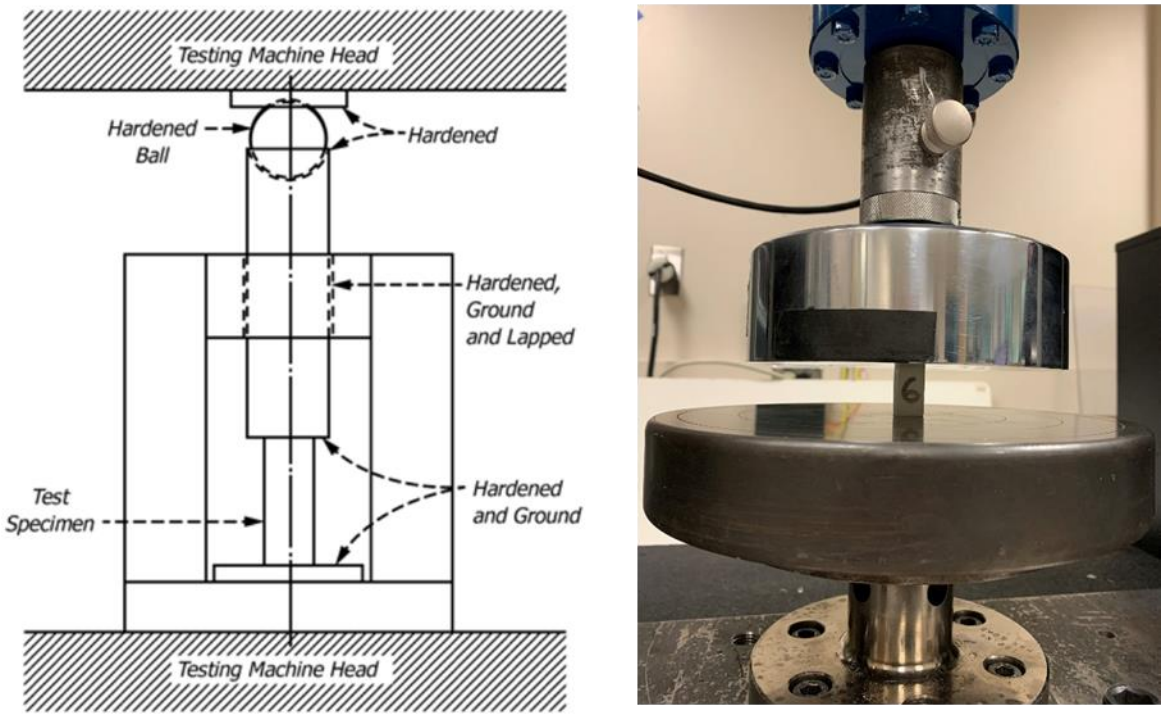

Figure 2.5 (left) ASTM D695 recommended test setup to acquire compressive properties of plastics [43] (right) Actual test setup used in the UW Mechanical Test Lab.

The plateau stress and strain, the strain value at which the polypropylene has yielded entirely and the corresponding stress, are determined qualitatively from the experimental data. The plateau strain is important as it informs of the height of the pad to use and the corresponding gap to leave between the pad and the roller. From Figure 2.6 it is observed that a strain of $\varepsilon > 0.15$ corresponds to the yield plateau and any strain value within this range would be permissible. Similarly, the plateau stress is important as it informs of the cross-sectional area size of the pads and then, to achieve the desired crack parallel stress, the area of the pads may be altered. Though note, the actual crack parallel stresses experienced will be determined from the raw experimental data to ensure the greatest accuracy. Clearly the plateau stress and strain are required values when designing the Gap Test experiment

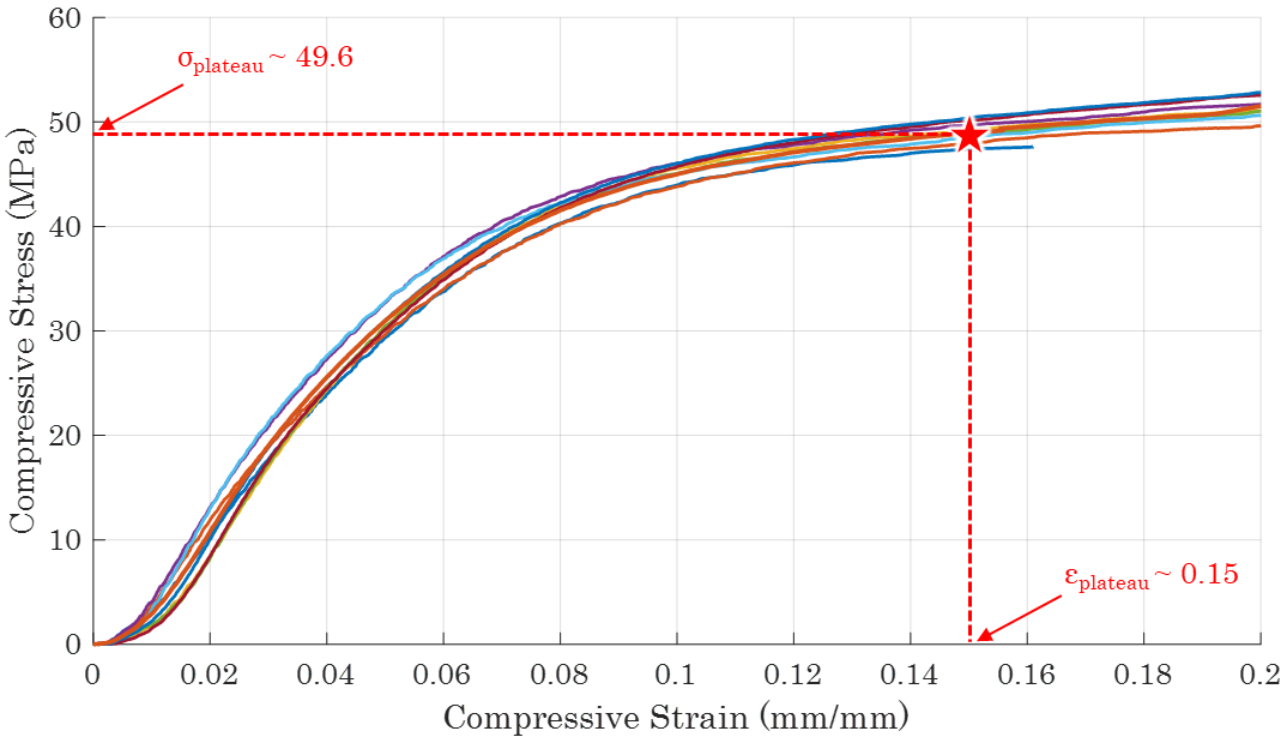

Figure 2.6 Compressive stress-strain curve of polypropylene showing the determined plateau stress and strain. Data obtained from ASTM D695 test procedure.

albeit, they need not be known at a precise point value and instead a compressive stress-strain curve of the pad material is much more practical from a design point of view.

With the details of the pads determined, the test fixture shown in Figure 2.4 must be modified to support the pads and permit the compressive portion of the Gap Test. Using SolidWorks 2021 a center column is designed that bolts into the existing fixture, as shown in Figure 2.7. The additional fixture component is machined in the UW Mechanical Engineering machine shop on a 2 axis CNC mill out of a 1018 Low-Carbon Steel blank, images from the machining operation and final fixture are shown in Figure 2.8.

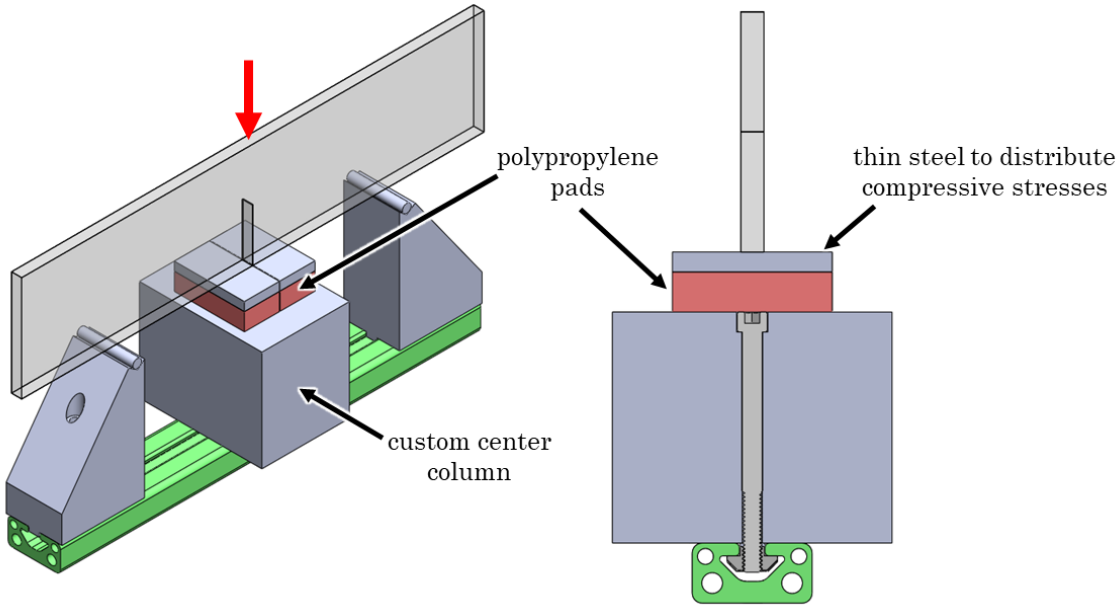

Figure 2.7 First design iteration of the custom fixture to be used for composite Gap Testing.

Figure 2.8 In process machining and final images of the first test fixture design for composite Gap Testing.

2.4 Composite Manufacturing

The composite manufacturing process executed herein follows the process used to manufacture aerospace grade quality parts in industry. This ensures that the experimental results are extendable to real world applications. The material system used during Gap Testing is uni-directional Toray T800H/3900-2, the first carbon fiber material commercialized for primary structures on Boeing commercial aircrafts and used for Boeing 777 components [44]. A summary of the manufacturing process is given below but note, the nuances of composite manufacturing are abounding and not discussed at length in the present text. The interested reader is directed towards the Composite Materials Handbook Volume 3 [45] or [46] for detailed discussions of composite manufacturing.

The composite material used is a pre-impregnated material, meaning the strong and stiff reinforcing carbon fibers are pre-impregnated with the matrix material that binds the fibers together. The matrix material is partially cured upon arrival (often referred to as B-staged) and hence to preclude the matrix from curing entirely the pre-preg composite material is stored in a freezer, typically at 0° F. The composite is wound around a cardboard cylinder and is stored in the freezer in such a way that the carbon fibers do not warp or break. It is also imperative that the composite material is stored in an air-tight bag in the freezer, any moisture intrusion into the matrix may result in porosity or incomplete curing in the final cured composite part. Prior to using the composite material, it must be removed from the freezer and allowed to thaw such that it will be pliable enough to work with. The thawing duration is dependent upon the size and type of composite material roll, often in the window of 4-8 hours. A common method to determine if the material roll is thawed sufficiently is to check for condensation on the bag surface – if condensation exists the material roll is not thawed and if condensation free the material is adequately thawed.

After the material is thawed it is rolled out on a ply cutter table in the UW Mechanical Engineering Composite Shop. A ply cutter is a 2 axis CNC gantry that drags a sharp knife across the pre-preg composite to cut it to the exact dimensions of each ply. The ply cutter table pulls vacuum on the pre-preg during the cutting operation to ensure a clean and precise cut is achieved. After all the desired plies are cut they are stored together in a kit while the

excess pre-preg material roll is re-bagged and returned to the freezer. Images from the ply cutting and kitting operation are shown in Figure 2.9.

Figure 2.9 (left) CNC ply cutter cutting pre-preg composite into the desired size, shape, and quantity of plies (right) ply kit containing the necessary plies for the composite part.

Next the composite plies are stacked by hand atop a flat aluminum plate to form the desired shape, size, and stacking sequence of the cured composite part – this process is referred to as layup. During layup the first ply down, every fourth ply after, and the last ply down are debulked for 10 minutes at a minimum vacuum pressure of 26 inHg. Debulking refers to placing a vacuum bag over the in-process layup and applying vacuum pressure to remove any entrained air within the plies and heighten the compaction between adjacent layers. The debulk vacuum bag used is composed of a specific anatomy of materials such that maximum air flow occurs, and the highest quality composite part is made. Images of in-process layup and the debulk bag schematic are shown in Figure 2.10. The layup schedule is a $[(0/90)_{9.5}]_s$ laminate, 38 total plies, that takes approximately 6 hours to layup entirely.

After layup is complete the part is prepared for cure. This first involves installing the cure bag which is similar in nature to the debulk bag but faces much high scrutiny. The cure

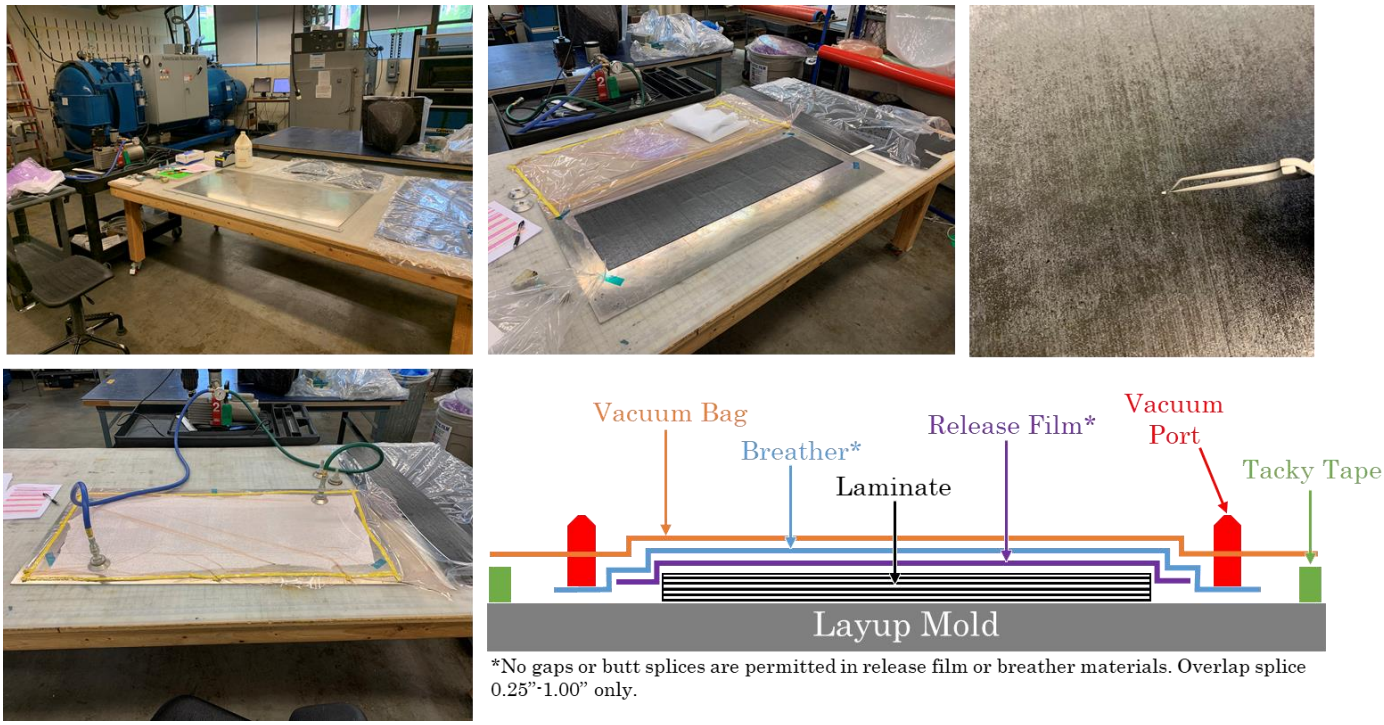

Figure 2.10 (top left) work bench used for composite layup with aluminum plate, supporting tooling, and ply kits shown (top middle) in-process layup (top right) FOD being removed during layup process (bottom left) debulk process during layup (bottom right) debulk bag schematic

bag is of the utmost importance as it facilitates the curing process of the pre-preg composite, notably it provides a pathway to remove air during the cure as well as compaction of the plies to mitigate voids or defects. A common quality check of the cure bag is a drop test, in which the cure bag is installed, brought up to full vacuum pressure, the vacuum pump is turned off, and the cure bag is required to maintain a certain vacuum pressure for a duration of time. This indicates the vacuum integrity that is achieved via the cure bag alone and serves to identify any punctures or damage that may have been induced into the cure bag. For the present manufacturing process a drop test requirement of at least 26 inHg, with a drop no larger than 1 inHg, for 10 minutes is imposed. A series of images giving the details of the cure bag are shown in Figure 2.11. After the cure bag has passed the drop test it is cured via a single dwell, high temperature and pressure autoclave cure. The cure schedule used is shown in Figure 2.12, the total cure time is ~10 hours.

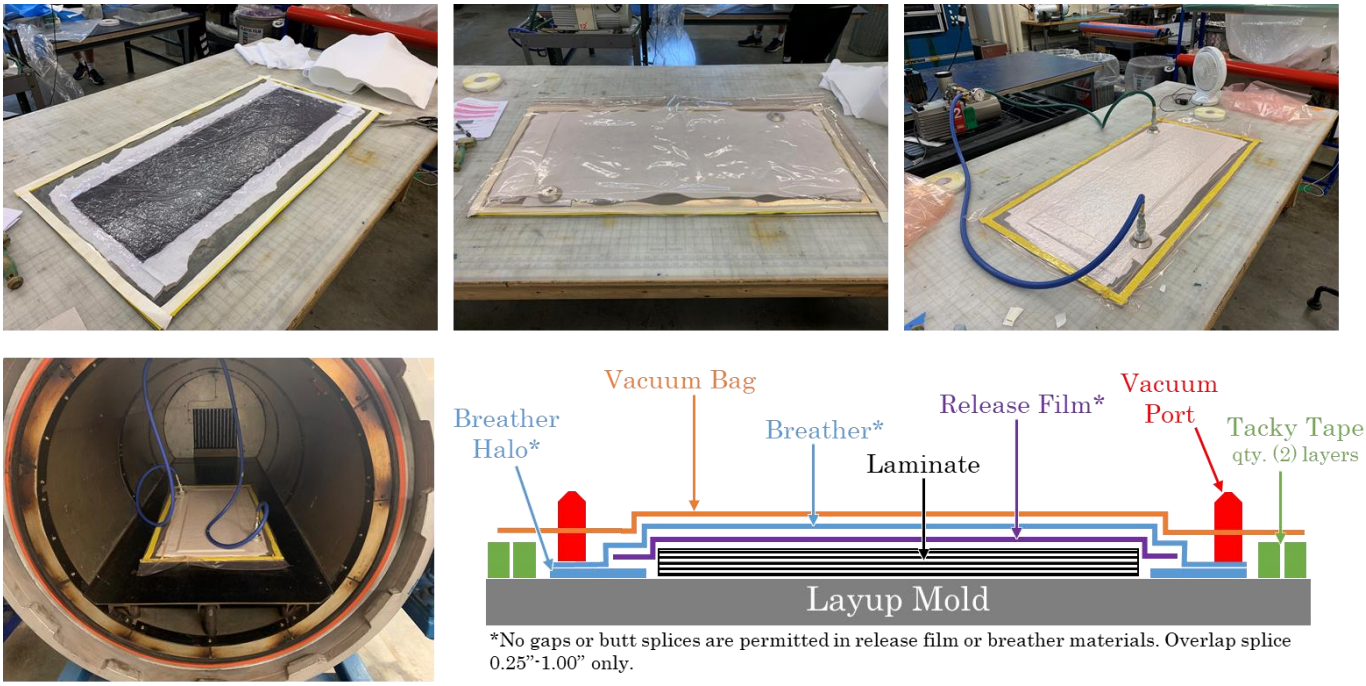

Figure 2.11 Cure bag installation procedure and schematic showing layer details.

Upon cure completion the tool and part are removed from the autoclave using industrial hot gloves and the part is allowed to come down to room temperature. The cure bag is then removed, and a visual quality inspection of the cured composite is performed. From this inspection potential defects that may be observed are FOD (foreign object debris), porosity, or discoloration that is indicative of incorrect cure procedures – no visual defects are observed in the composite panels that were manufactured for Gap Testing. As a point of caution cured composite parts usually exhibit a knife edge condition due to plies terminating at slightly different locations along the part boundaries. Therefore, it is very easy to lacerate one's hand when handling cured composite parts, to prevent this cut gloves should always be worn when handling untrimmed, cured composites.

2.5 Test Specimen Preparation

The manufacturing process outlined in section 2.4 is used to fabricate a single master panel that multiple test specimens are cut out of to the dimensions defined in Table 2.2. A wet tile saw that is equipped with a diamond blade is used to partition the master panel into the

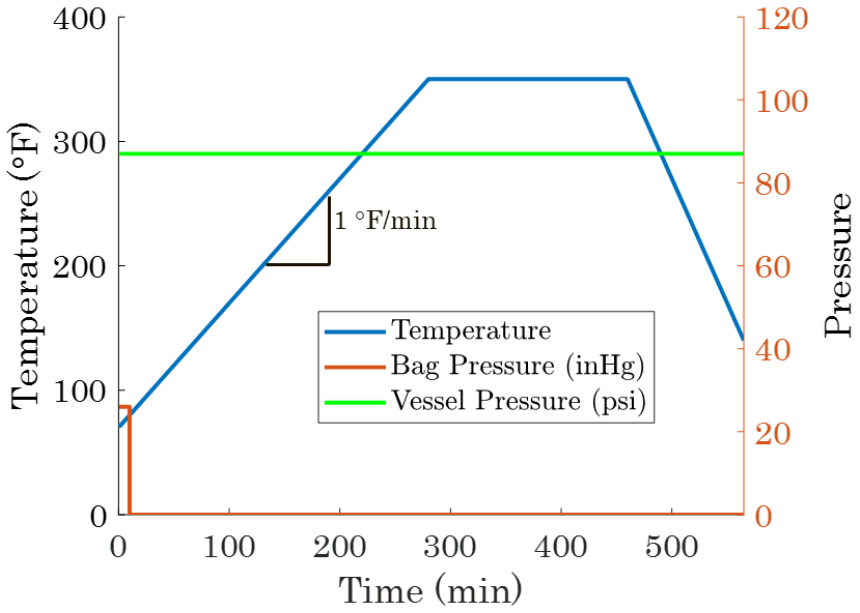

Figure 2.12 Cure schedule used to fabricate composite panels for Gap Testing.

three test specimen sizes. Following conventional composite manufacturing processes, the tests specimens are cut a minimum of 25.4 mm (1") from the edge of the master panel to

Figure 2.13 Master panel being cut with a wet tile saw to the desired test specimen dimensions.

ensure that no uneven ply terminations are included in the test specimens. Images from this cutting operation are shown in Figure 2.13.

The cutting of the master panel presents the opportunity to inspect the cross section for porosity via photo-microscopy (PMG). This is accomplished by taking a cut edge of the master panel and polishing it until a smooth and flat surface is achieved that may be inspected with a high-resolution microscope. To polish the cut edge deionized water and increasing grit sandpaper (220 → 600 → 2000 → 3000 grit) is used on a flat surface while the cut edge is sanded down by hand using a figure-eight pattern. Then a 0.5 μm OpTech diamond slurry is used with a polishing pad to provide an ultra-fine finish. The PMG images of the cross section are shown in Figure 2.14 for different magnifications. No visible porosity is identified which indicates a high-quality composite panel and from which, there are no concerns that quality defects will undermine the experimental results.

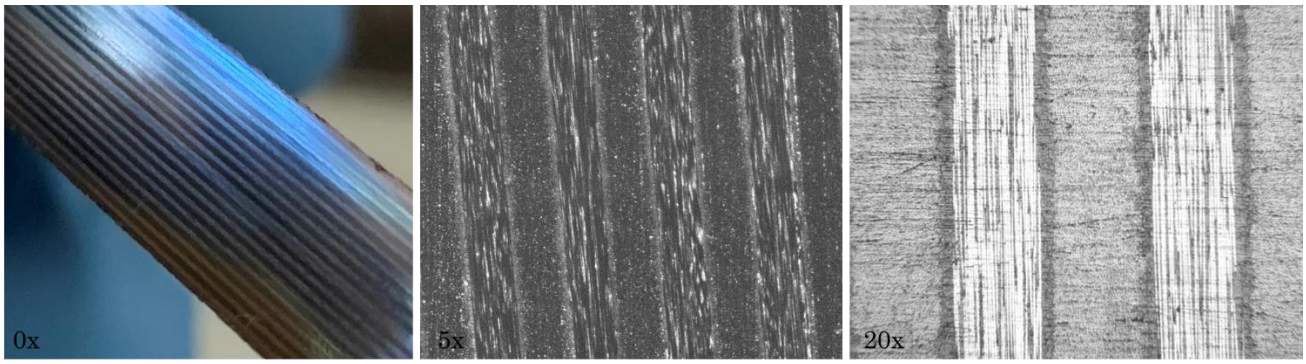

Figure 2.14 PMG images of the manufactured composite panel's cross section at 0x, 10x, and 20x magnification.

The ensuing step in test specimen preparation is installation of the cracks. A standard procedure for pre-cracking composite specimens to a pre-determined length does not exist like it does for metallics. Metallics are typically pre-cracked through fatigue loading at a stress amplitude that is much lower that the material's failure limit [34]. While this is an effective technique it is expensive timewise and requires dedicated fixturing to execute. Furthermore, the anisotropic behavior and heterogenous composition of composites make it unlikely that a straight, self-similar crack will be achieved through fatigue pre-cracking.

When installing cracks for fracture mechanics experiments though there is one commonality across all material types – the crack, and specifically the crack tip, should be as sharp as possible. Idealistically having a crack tip radius equal to zero like that of the assumptions that govern LEFM [15]. This is done to mimic the behavior of structures in the real world where cracks initiate at a microscopic scale and hence have a nearly zero radius crack tip which results in the highest stress intensity [47].

Cracks for the present study are installed by hand using the thinnest kerf blade that could be found for purchase, a 0.508 mm kerf blade from Zona Tool. It is also desirable to install the cracks manually as a power tool such as a bandsaw or pencil grinder may induce damage at the crack tip which could impact the composite's fracture behavior. To guarantee a straight crack is installed a mitre box is used to guide the blade to the desired crack length. Installation of an angled crack is particularly undesirable as it will result in mixed mode loading and previous experimental data has shown that a composite's structural strength will fluctuate based on the degree on load multiaxiality [18]. Also, the present study is aimed at Mode I fracture only so a mixed Mode I-II loading will conflate the experimental results. Images of the crack installation process are shown in Figure 2.15.

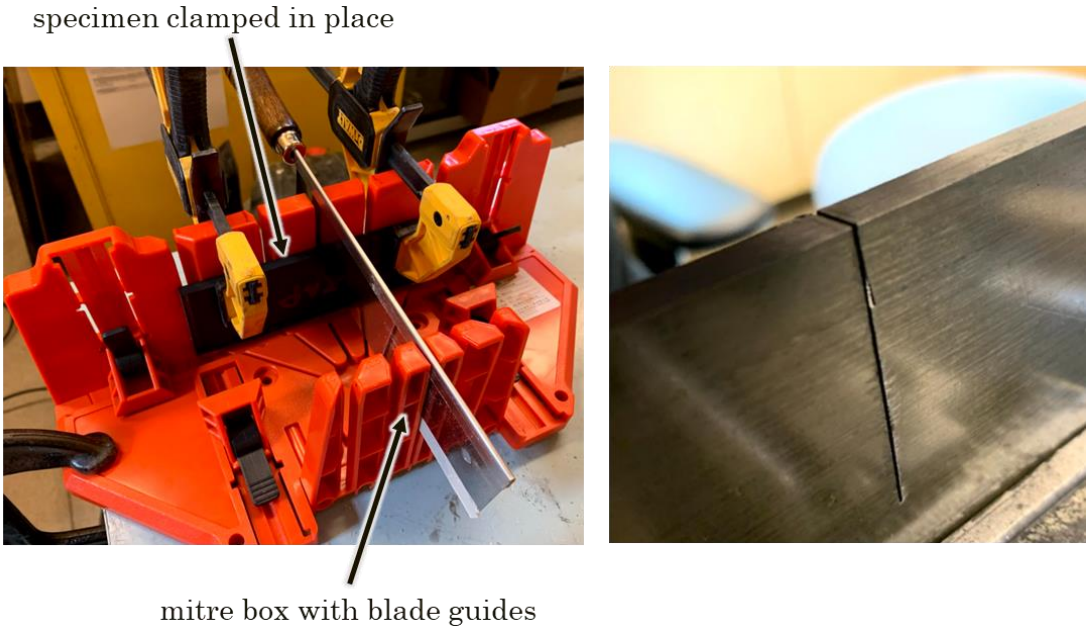

Figure 2.15 (left) Test specimen clamped into a mitre box that is used to install straight cracks (right) resulting straight crack

To complete the Gap Testing preparation specimens are speckled with spray paint that is used for DIC data acquisition. First, the tool-side (smoother side) of the test specimens are cleaned with acetone or isopropyl alcohol and then sprayed with a uniform coat of white Rust-Oleum spray paint. Additional coats of white paint are applied as needed. Once the white paint has dried a black Rust-Oleum spray paint is used to apply a speckle pattern atop the white layer. The speckling is achieved by holding the spray canister approximately 0.5 meters away from the specimen and moving it in a sweeping pattern. Any unsatisfactory application of the white layer or black speckling is simply removed with acetone or isopropyl alcohol and reapplied. Figure 2.16 shows an example of the stochastic pattern that results when following the above procedure.

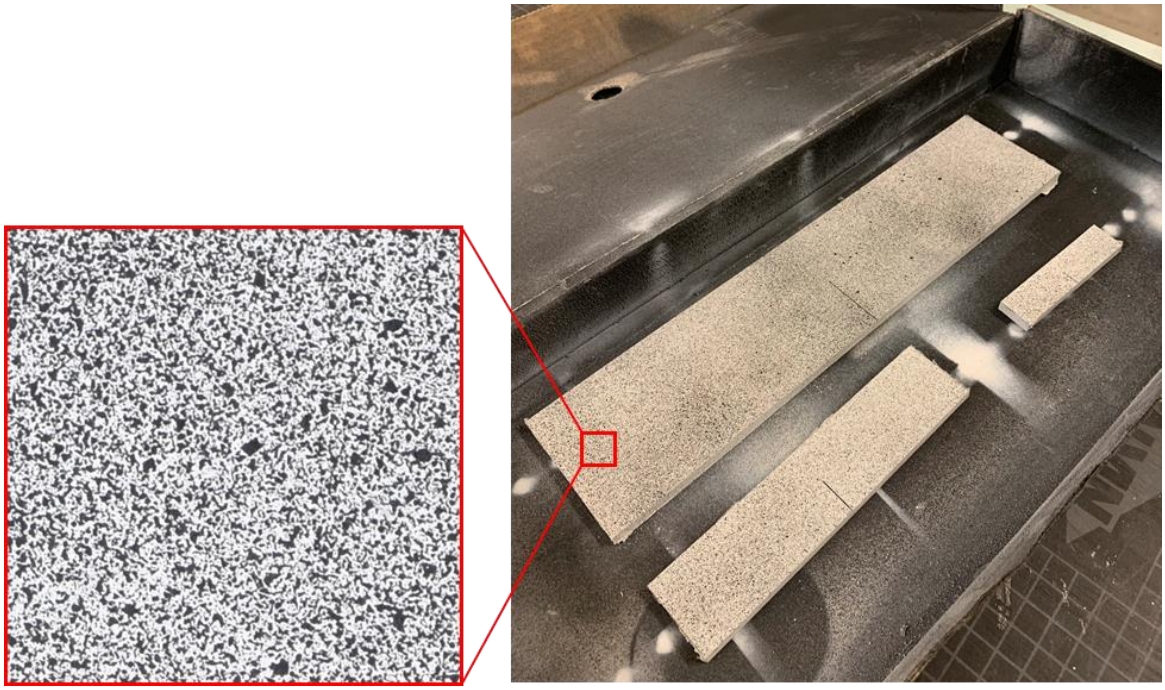

Figure 2.16 Stochastic pattern used for DIC data acquisition.

Chapter 3 Gap Testing, Results and Analysis

3.1 Initial Attempts

The design depicted in Chapter 2 represents a first and entirely novel attempt to execute the Gap Test for a composite material and rather unsurprisingly, the first attempts are unsuccessful. Three design updates to the initial design put forth in Figure 2.7 and Figure 2.8 are required to achieve a successful Gap Test and useable experimental data. These design updates and the failures that motivated them are discussed in the below text.

The initial Gap Test design attempts to execute in the simplest manner: a 3PB loading condition where a single roller transmits the force from the load frame to the test specimen. This results in a stress concentration at the load application point and ultimately causes delamination failure in the composite prior to crack propagation at the crack tip, as shown in Figure 3.1. To remediate this a 4PB loading condition with a small but finite top roller span

Figure 3.1 Delamination failures that occur due to stress concentrations in the initial Gap Test design.

is adopted. Additionally, thin steel caul sheets are used to reduce the stress concentration at the load application point by distributing the load. Inclusion of the steel cauls in the test procedure does add additional preparation time as the cauls must be cut to size and bonded in place. In the present study a sheet of hardened steel is ordered from McMaster Carr, from

which the cauls are cut on a vertical bandsaw, and then bonded onto the test specimen with a high strength JB Weld adhesive as shown in Figure 3.2. The cauls are also placed with a deliberate gap between them to avoid adding any flexural rigidity to the test specimen that could impact the experimental data. A schematic of this second test design is shown in Figure 3.3.

Figure 3.2 Additional test specimen preparation required to include steel caul sheets with a 4PB loading condition.

Figure 3.3 Second design iteration used to execute the Gap Test on composites.

The second design in Figure 3.3 is successful for the remainder of the control group testing, the panels for which no crack parallel compression is applied. But when this design is used to apply crack parallel compression the test proves again to be unsuccessful. What transpires is an instability in the polypropylene pads that leads to the test specimens toppling prior to fracture. Note that this is a different failure mechanism than buckling which is not observed due to the analysis of section 2.2. In process images that highlight the structural instability in the polypropylene pads are shown in Figure 3.4. The root cause of this

Figure 3.4 Second design iteration failures when attempting to apply crack parallel compression (top) test specimen toppling prior to fracture (bottom) structural instability in polypropylene pads that causes toppling.

instability is yielding of the steel that is intended to compress the polypropylene pads uniformly. To correct such two measures are taken. First, the thickness of the steel atop the polypropylene pads is increased while the thickness of the polypropylene is decreased, see Figure 3.5. This is a more robust structure that is less susceptible to the steel yielding or general instability. Second, as a measure of redundancy, additional fixturing is added to that shown in Figure 2.7 and Figure 2.8. Lateral stability columns are included to prevent the test specimens from toppling and ensure they stay within the plane in which the compressive load

is applied. All additional fixturing is machined per the same process defined in section 2.3. These updates represent the third design iteration and are captured in Figure 3.6

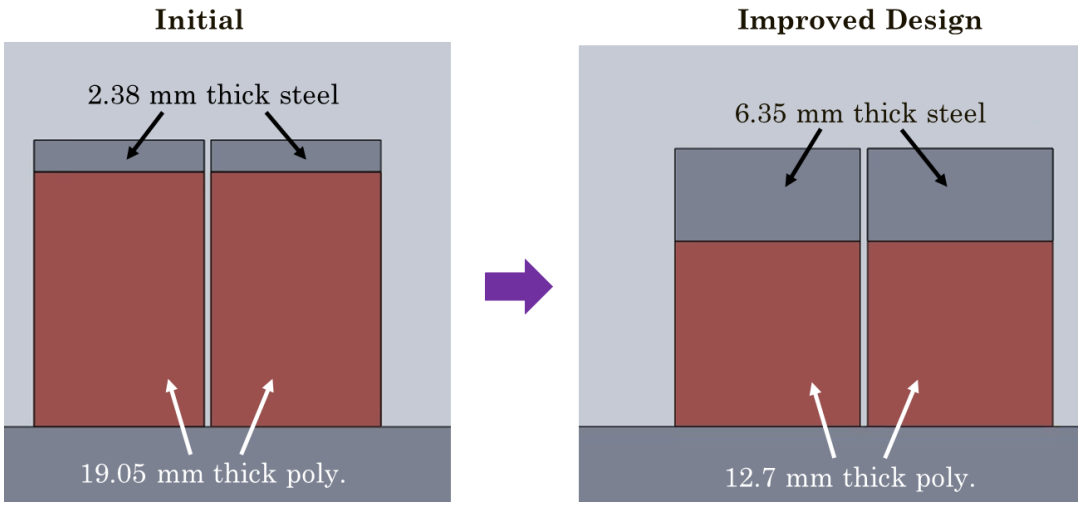

Figure 3.5 Polypropylene pad redesign to mitigate structural instabilities that result during the Gap Test.

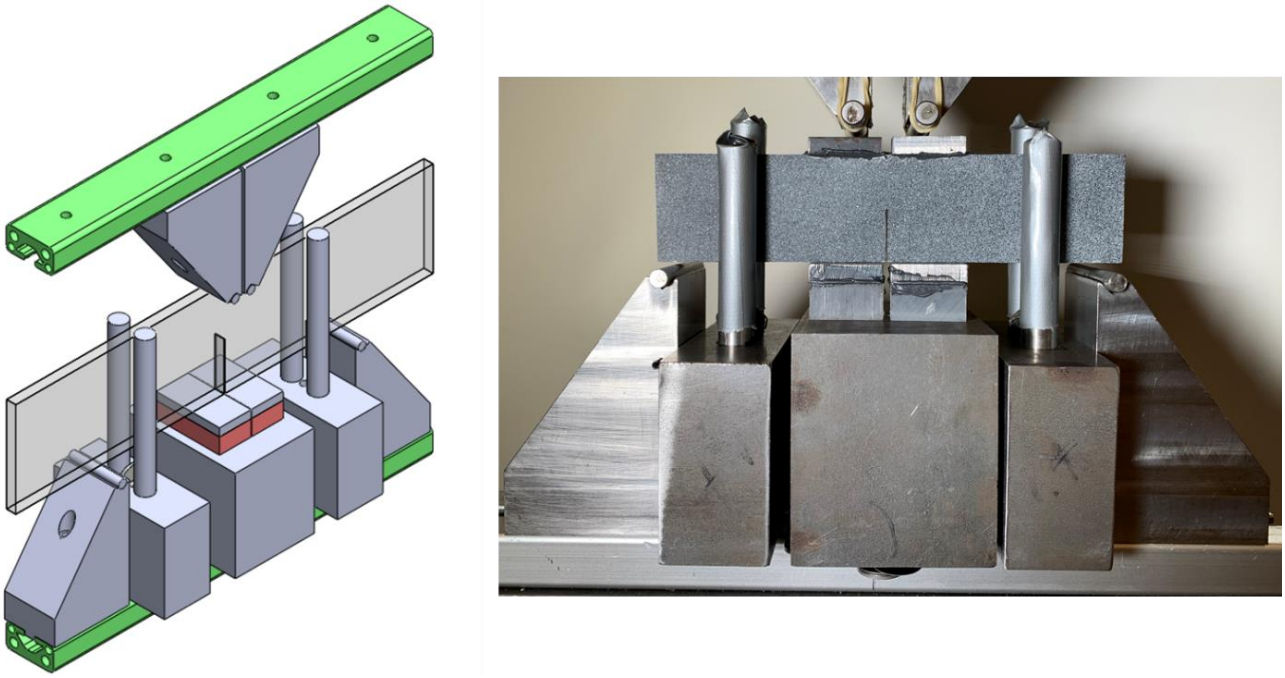

Figure 3.6 Third Gap Test design that includes updated polypropylene pad geometry and additionally machined fixturing to support stability columns.

The third design iteration in Figure 3.6 is an improvement from the second design in Figure 3.4 although it to proves to be inadequate to completely combat the toppling issue. As seen in Figure 3.7, the third design performs almost as desired albeit the test specimen still has a minor ability to tilt out of plane. This does not cause the test specimen to topple off the fixture due to the presence of the stability columns. But the minor tilting induces a bending moment on the top steel cauls which eventually causes a delamination failure between them and the composite test specimen. Minor damage is also observed in the test specimen due to

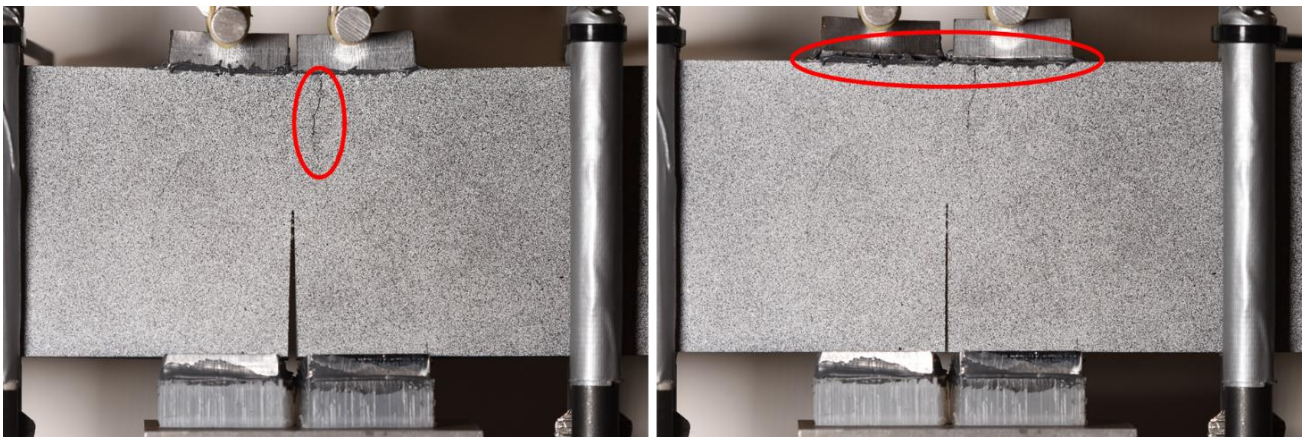

Figure 3.7 Delamination failures and test specimen damage that occur with the third Gap Test design.

the out of plane tilting. To eliminate this a bolted constraint is added to the stability columns used in the third design. The bolt is fastened only finger tight and consequently any contribution of the stability columns to the test specimen's fracture behavior is assumed to be negligible. This fourth Gap Test design is finally what proves to be successful, and it is the design that is used to capture all the experimental data shown in the following sections. Figure 3.8 shows this design and as before, the new fixturing is machined in-house in the UW Mechanical Engineering machine shop by the author.

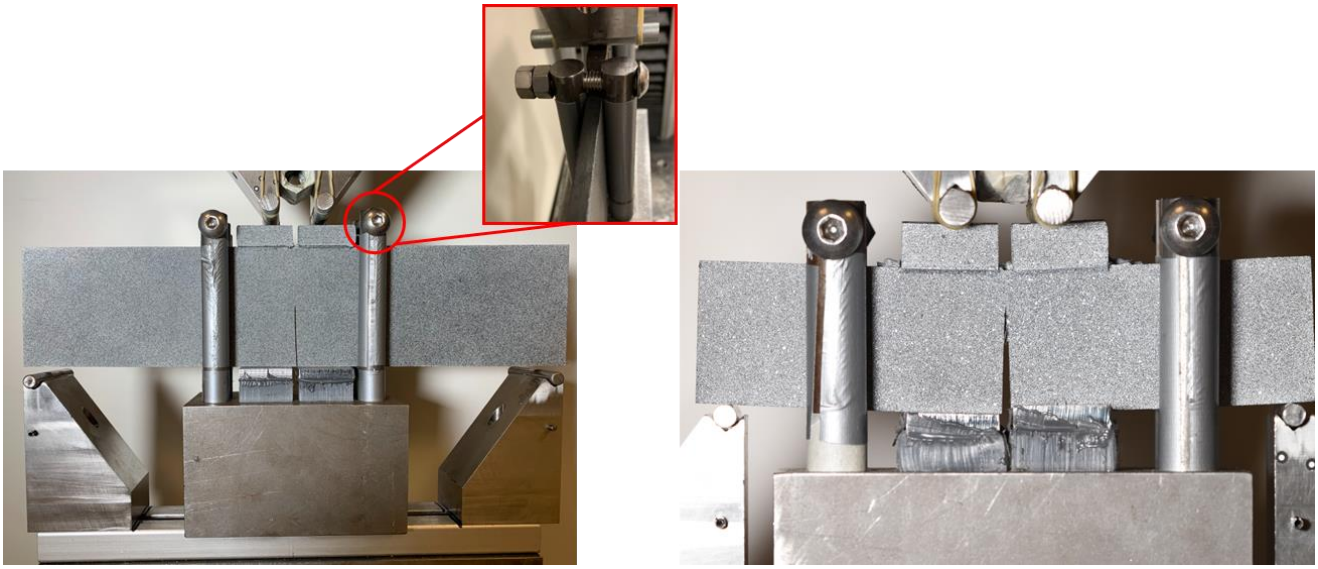

Figure 3.8 (left) Fourth and final Gap Test design used to capture all experimental data (right) example of a successful crack parallel compression test.

3.2 Experimental Procedure

The Gap Test generally follows the guidelines of ASTM 7264 [42] and 5045 [48] to maintain consistency with the standard test procedures that are used in the academic community (it is noted that ASTM 5045 is no longer an active standard so it's guidelines are taken as a general starting point where applicable). Though, as seen in Chapter 2 and section 3.1, the uniqueness of the Gap Test elicits multiple scenarios where standard test specifications do not provide adequate definition – specimen dimensions to avoid buckling and pad material composition for example. Nonetheless, after the development phase defined in section 3.1 the common Gap Test procedure used is as follows:

1. Obtain the desired test specimen from those defined in Table 2.2, record its actual dimensions, and permanently label it with a unique identifier. For example, *smallpanel_nocompression_test1*
2. Load the test specimen into the fixture shown and check all dimensions against nominal with calipers. Adjust the test setup as needed.
3. Using an Instron 5585H load frame manually apply 25 N of preload to 'seat' the test specimen appropriately.

4. Using a bright external light source illuminate the test specimen surface to ensure high fidelity DIC images are obtained.
5. Focus a high-resolution camera on the crack tip and include as much of the adjacent test specimen surface as possible. Set the camera to capture images at a rate of 1 image/second.
6. Start the image capture on the camera and then begin a constant displacement test on the load frame at a rate of 1.27 mm/minute.
7. Allow the test to run to a minimum of the peak load and, if the post peak behavior is stable, allow the test to run until the measured load is ~ 0 N.
8. If complete fracture occurs label all separate test pieces with the appropriate unique identifier.
9. Download the force-displacement data from the load frame workstation and save it with a standard naming convention that includes the test specimen unique identifier.
10. End test.

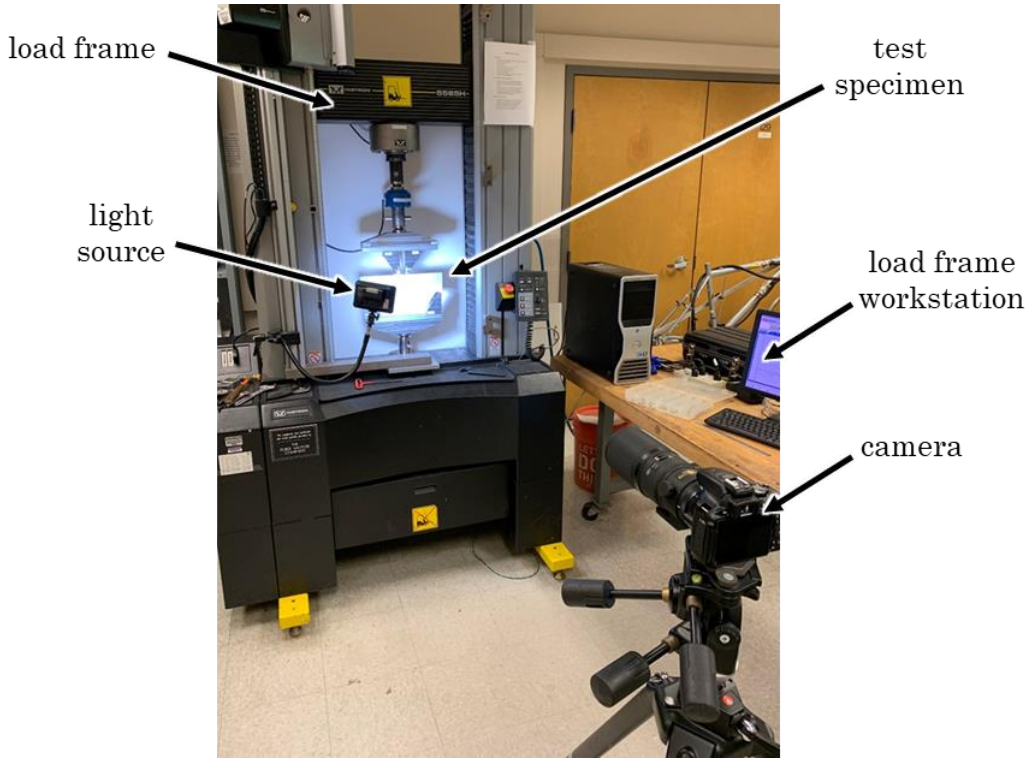

Figure 3.9 Experimental setup used to acquire the Gap Test data.

3.3 Results

The output from each Gap Test is a 3-column matrix including the time, displacement, and force values measured every 0.1 seconds by a transducer on the load frame. Thus, an initial tendency may be to calculate the fracture energy for each test from the area under the stress-displacement curve [49] per equation (3.1). This would be a simple means of analysis but it

$$G_f = \int_{\delta = 0}^{\delta = total\ failure} \sigma(\delta) d\delta \tag{3.1}$$

is not appropriate presently for 3 reasons. First, the post-peak behavior of the composite materials in this study tends to be unstable and hence the full area under the stress-displacement curve may not be calculated for all tests. Also, the displacement values are output from a transducer that includes a small but finite compliance of the test fixture which alters the area under the stress-displacement curve. A DIC analysis must be performed to extract the displacement of the test specimen only. Lastly, due to the presence of a non-negligible FPZ the small size test specimens may exhibit notable non-linear behavior and to accurately calculate the fracture energy the Bažant Type II SEL, equation (1.1), must be used [19]. The Bažant SEL is fortunately derived based on a material's structural strength, which is directly determined from the peak load in each Gap Test, thus it is both simpler and more correct than equation (3.1).

Following the previously defined test procedure the Gap Test is first performed for the case of no crack parallel compression, which is a standard 4PB test per ASTM 7264 that will serve as the control group. A combined force displacement plot for all 3 panel sizes, subsequently referred to as small, medium, and large per Table 2.2, of the control tests is shown in Figure 3.10. Notice that for all test sizes the force displacement response is linear up to the peak load. This is indicative of brittle behavior as there is no warning of failure or crack propagation and implies a limited effect of the nonlinear stresses within the FPZ. The control tests also display progressive damage, deduced by the saw-tooth behavior of the force displacement response immediately prior to or after the peak load. This occurs due to modulus degradation in the damaged plies while the undamaged are still capable of taking

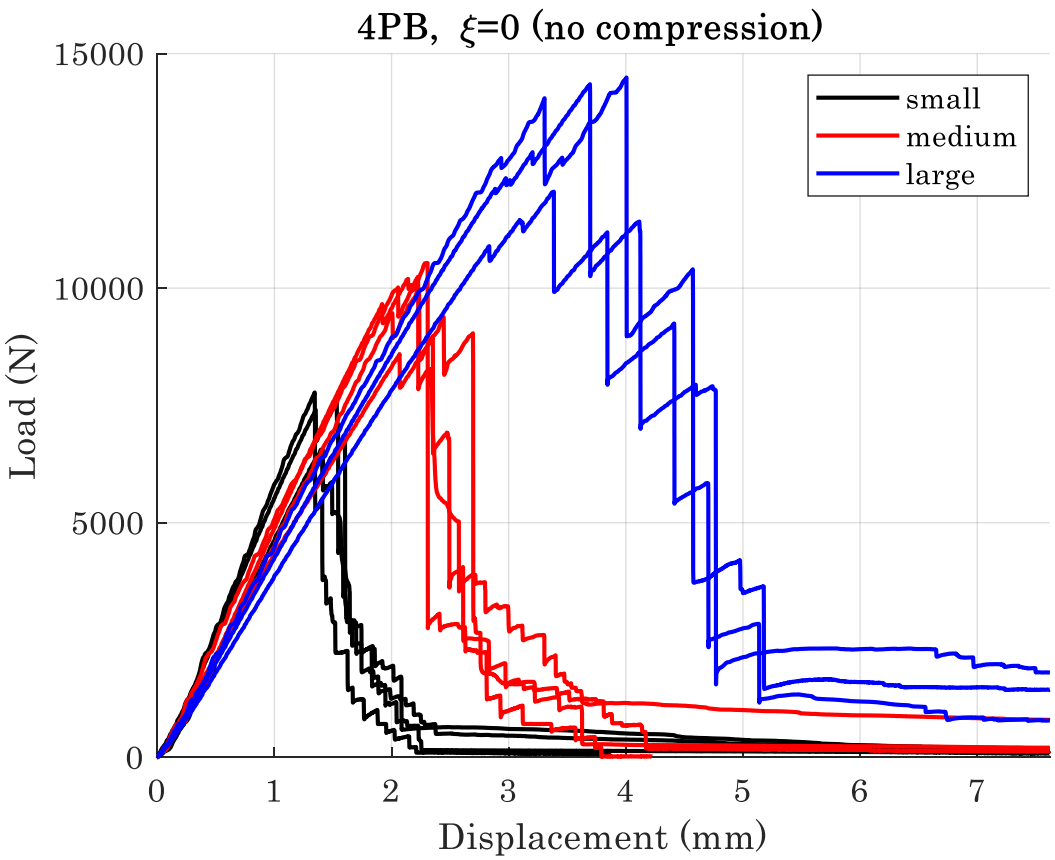

Figure 3.10 Force displacement results for the Gap Test with no crack parallel compression.

load up to their failure point [50]. A stable post-peak regime is also seen in all the control tests which corresponds to stable crack propagation during the fracture test. For analysis via the Bažant SEL the peak load is the most critical experimental value which is tabulated in

ξ = 0			
Size	Quantity	Avg. Peak Load (N)	CoV*
Small	4	7167.2	0.0834
Medium	4	9924.1	0.0702
Large	3	13631.2	0.1001

*CoV is the standard deviation divided by the mean

Table 3.1 Peak load values for the Gap Test with no crack parallel compression (ξ = 0).

Table 3.1 for the control tests. There is some variation in the peak loads which is attributed to (1) minor differences in the actual geometry of each specimen and (2) statistical uncertainty that is inherit to all material failure testing and exacerbated in heterogenous materials such as composites [51].

The same test procedure is performed on all the test specimen sizes but now including the crack parallel compression which is achieved via the design in Figure 3.8. Two levels of compression are tested, $\xi = 0.29$ and $\xi = 0.44$, where ξ is the crack parallel stress normalized by the compressive strength of the laminate. ξ is a non-dimensional parameter that varies between 0 and 1 and quantifies the degree of biaxiality of the Gap Test. In the ensuing discussions ξ is referenced as a general term which corresponds to the specific set of data i.e., $\xi = 0$ denotes the control group of data while $\xi = 0.29$ denotes the data set from this level of compression. The details of calculating ξ are also covered in the following section. The force displacement data of the $\xi = 0.29$ and $\xi = 0.44$ tests are seen in Figure 3.11 and Figure 3.12,

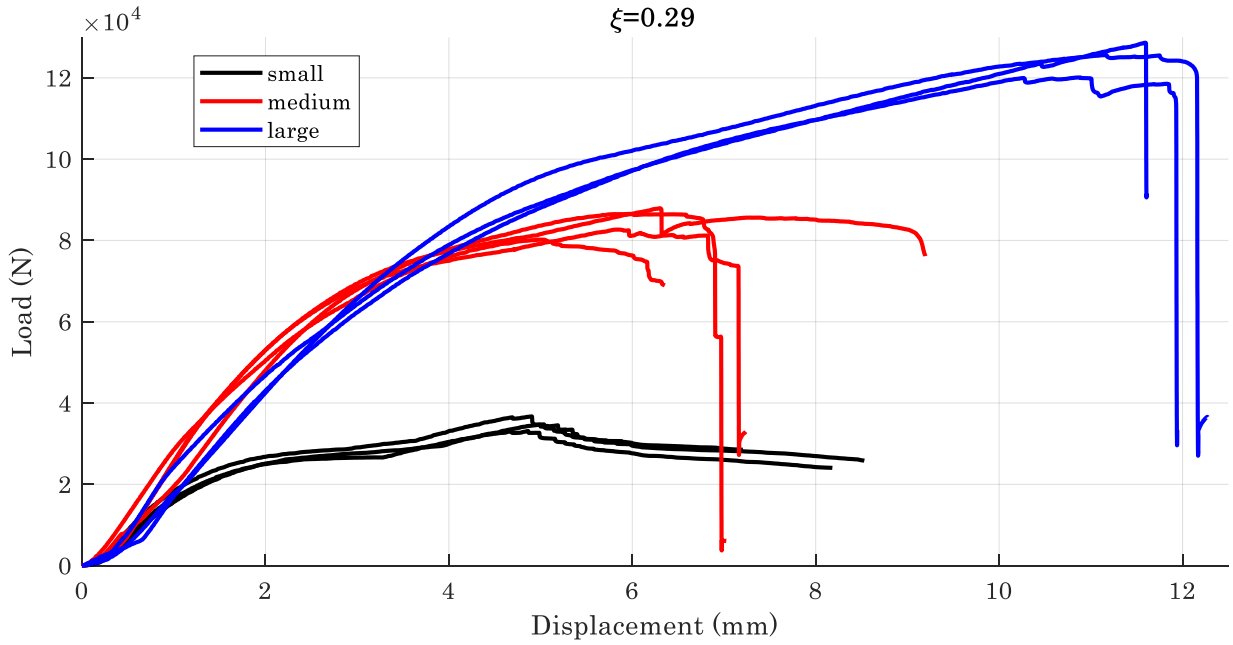

Figure 3.11 Force displacement results for the Gap Test with $\xi = 0.29$.

respectively. The force displacement curves for the ξ = 0.29 and ξ = 0.44 tests are notably different in shape than the curves for ξ = 0 due to the presence of the compressive stress. To interpret these plots each distinct regime needs to be identified and juxtaposed against the statically determinate stress state as shown in Figure 3.13. The four distinct stress states are easily identifiable within all the experimental data sets, as seen in the representative plot in Figure 3.13, an indicator of successful testing and also a selling point for the simplicity of the Gap Test.

In contrast with the ξ = 0 data, the ξ = 0.29 and ξ = 0.44 tests tend to display an unstable post-peak behavior, noted by the sudden drop of the force displacement plot which is characteristic of unstable crack propagation and or a catastrophic failure such as transverse cracking. A comparative image of the post-peak behavior for a ξ = 0 test versus a ξ = 0.44 is shown in Figure 3.14. This is an early indicator that a different, or perhaps more, damage mechanisms are occurring in the FPZ due to the presence of the crack parallel compression. Also, the ξ = 0.29 and ξ = 0.44 tests begin to exhibit a nonlinear force displacement response as the peak load is approached, most notably for the medium and

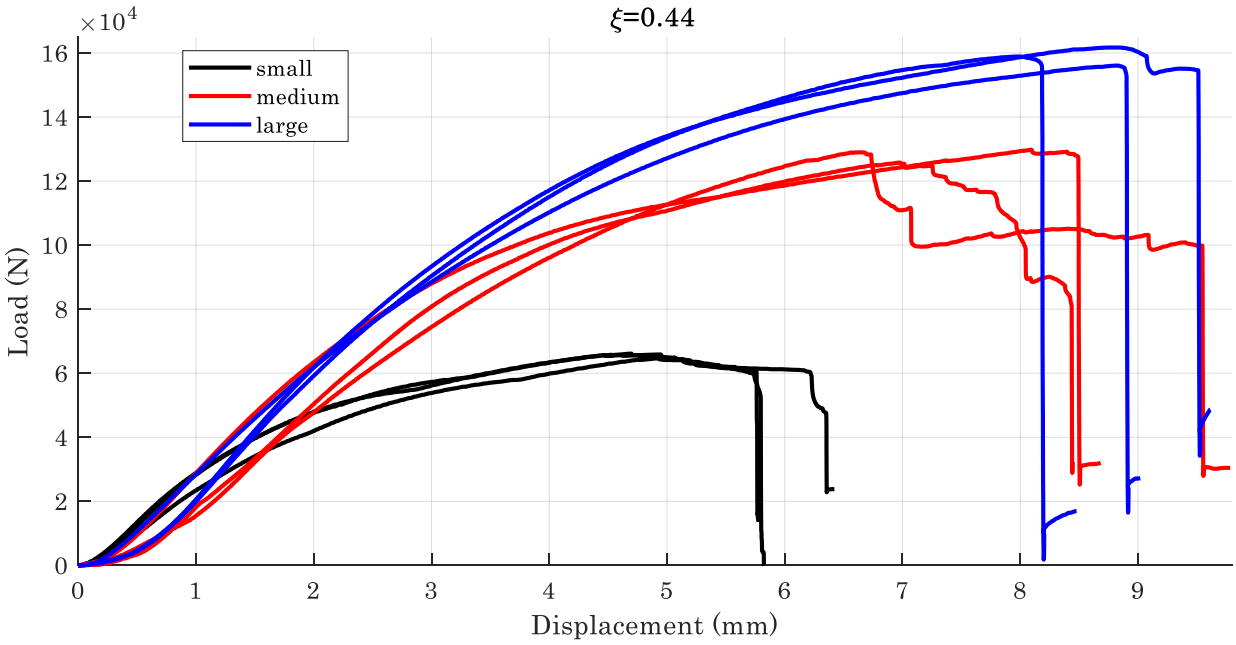

Figure 3.12 Force displacement results for the Gap Test with ξ = 0.44.

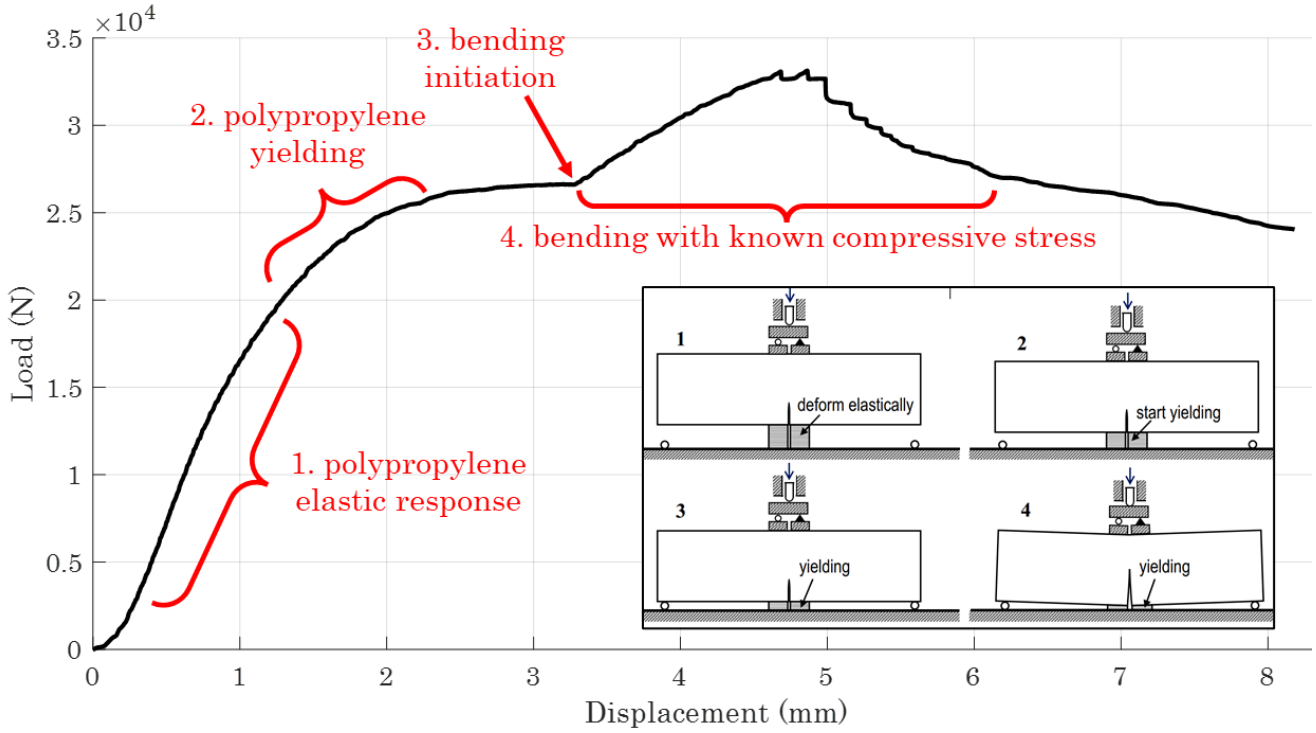

Figure 3.13 Example force displacement plot for the Gap Test with crack parallel compression decomposed into the 4 distinct, statically determinate stress states.

large size panels. One possible explanation for this is the influence of the nonlinear stresses within the FPZ that may dominate the structure's response in the presence of a crack parallel compression, a phenomenon that would support the hypothesis initially postulated in section 1.4.

Analytically the peak load of the Gap Test is the most important value however, for the $\xi = 0.29$ and $\xi = 0.44$ tests the regime corresponding to bending only (no. 4 in Figure 3.13) must be isolated to permit a comparison with the $\xi = 0$ tests. In other words, it is desired to perform an analysis of the structures bending performance in the presence of a known and constant compressive force. This is achieved by determining the compressive force at bending initiation (no. 3 in Figure 3.13) and subtracting it from the bending regime, whose resultant is the bending response only. To calculate the compressive force accurately and efficiently at bending initiation an n-degree polynomial is fit to the discrete force displacement data set. The derivative of this polynomial is then evaluated to identify exactly when an increase

occurs which corresponds to the minor stiffness change when bending is initiated. This additionally gives the displacement value at bending initiation that, as a measure of

Figure 3.14 Representative images of the post peak behavior differences for a Gap Test without and with crack parallel compression. (left) $\xi = 0$ small panel exhibiting stable crack propagation (right) $\xi = 0.44$ medium panel exhibiting transverse fracture after initially unstable crack propagation.

redundancy, is visually compared against the DIC images to confirm its correctness as the instance of bending initiation. To explain, the Gap Tests are run at a constant displacement of 1.27 mm/min. while DIC images are taken every 1 seconds and labeled with an index corresponding to this time stamp i.e., *image_67* is taken at the 67 second mark. Thus, as an example, if the bending initiation displacement is 6mm the corresponding DIC image index is 6mm * 1min./1.27mm * 60s/min. = 283.46 ~283. Image 283 is then checked to confirm that it is the exact moment the test specimen engages the rigid rollers and bending is initiated. This is a highly accurate process, all Gap Test data presented herein is checked via this and all are within 0 or ±1 images of the polynomial calculated image index. As an alternative method the force displacement response of the polypropylene pads shown in Figure 2.5 could be subtracted from the force displacement response of the Gap Test to segregate the force displacement response of the composite only. This methodology was not employed presently as the polypropylene data collected did not include displacements that were large enough to

compare to those used during Gap Testing and hence extrapolation would have been required.

Using the bending initiation loads the peak loads of the bending regimes for the ξ = 0.29 and ξ = 0.44 tests are identified, which are shown in Table 3.2 and Table 3.3, respectively. Comparison of these values to the ξ = 0 data in Table 3.1 indicates a decrease in the peak load as ξ is increased. A reduction of the peak load and consequently structural strength correlates to a reduction of the fracture energy, contradicting the LEFM assumption that the critical fracture energy is a constant material property. This is further supporting evidence that the finite width FPZ in composites is impacted by a crack parallel compression. A peak load comparison plot for ξ = 0, 0.29, and 0.44 is shown in Figure 3.15. In the next section these peak loads will be used to quantify the Mode I fracture energy while the fracture energy decrease is explained through PMG images of the test specimen crack tips.

ξ = 0.29			
Size	Quantity	Avg. Peak Load (N)	CoV
Small	3	5935.5	0.0933
Medium	4	7759.8	0.1569
Large	3	11269.8	0.0699

Table 3.2 Peak load values for the Gap Test with ξ = 0.29.

ξ = 0.44			
Size	Quantity	Avg. Peak Load (N)	CoV
Small	3	5618.0	0.0362
Medium	3	7592.7	0.0922
Large	3	10641.7	0.0497

Table 3.3 Peak load values for the Gap Test with ξ = 0.44.

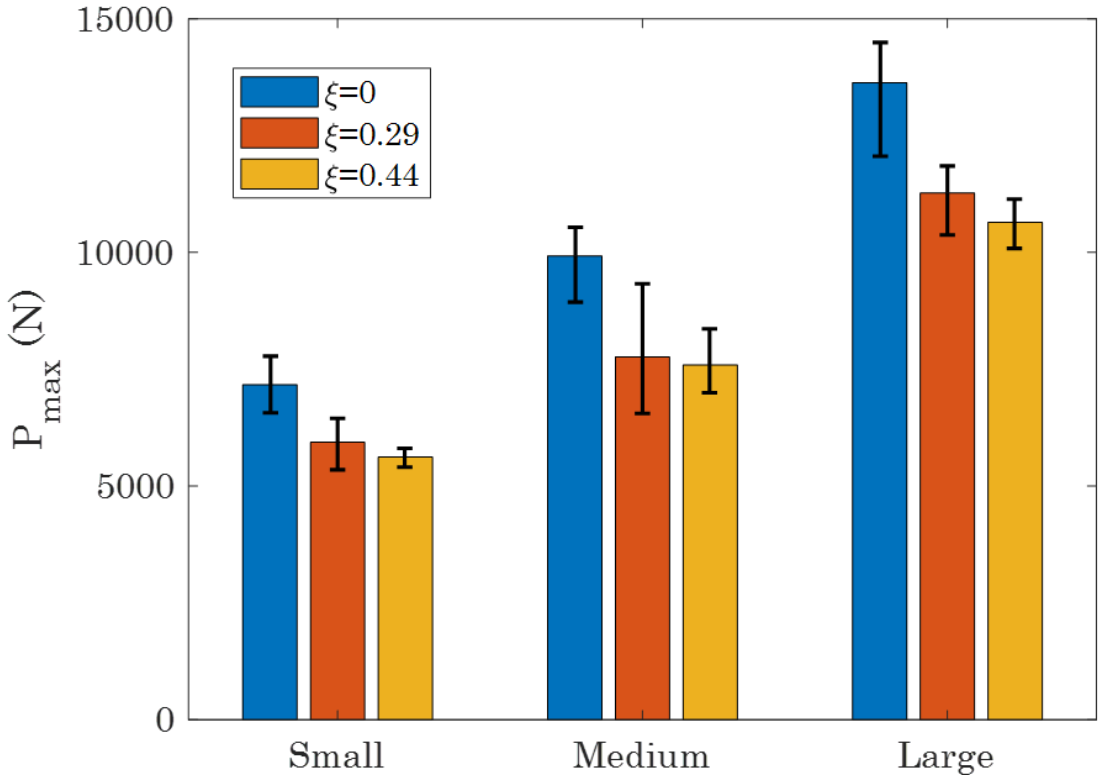

Figure 3.15 Measured peak loads for ξ = 0, 0.29, and 0.44.

3.4 Analysis

3.4.1 ξ Calculation

The parameter ξ is a normalized level of the crack parallel stress that is applied, used frequently in this thesis for convenience and as a general value for comparison with Gap Tests on other materials. It is calculated via simple solid mechanics as follows. From Figure 3.16 the cross-sectional area of the pad is,

$$A_{pad} = s * w \tag{3.2}$$

Thus, when the pad is compressed beyond yield the force generated is proportional to the plateau stress of the pads which is shown in Figure 2.5.

$$F_{pad} = \sigma_{plateau} * A_{pad} \tag{3.3}$$

The resulting crack parallel stress in the laminate σ_{xx} is then the pad force acting over the effected laminate area, subbing equations (3.2) and (3.3) into this expression leads to the simplifications below.

$$crack\ parallel\ stress: \sigma_{xx} = \frac{F_{pad}}{A_{lam.}} = \frac{\sigma_{plateau} * s * w}{t * s} = \frac{w}{t}\sigma_{plateau} \tag{3.4}$$

To determine ξ the σ_{xx} value is divided by the compressive strength of the laminate, denoted σ_c.

$$\xi = \frac{\sigma_{xx}}{\sigma_c} = \frac{w}{t}\frac{\sigma_{plateau}}{\sigma_c} \tag{3.5}$$

By this definition $\xi = 0$ indicates no crack parallel compression and $\xi = 1$ indicates the material is at its compressive failure limit. Additionally, equation (3.5) may be used in the initial Gap Test design phase to determine the expected ξ values and ensure that meaningful crack parallel stresses are applied. As previously stated though, to obtain the most accurate ξ values the bending initiation force determined in section 3.3 is used in place of the pad force (note that the two values are nearly inextricable though).

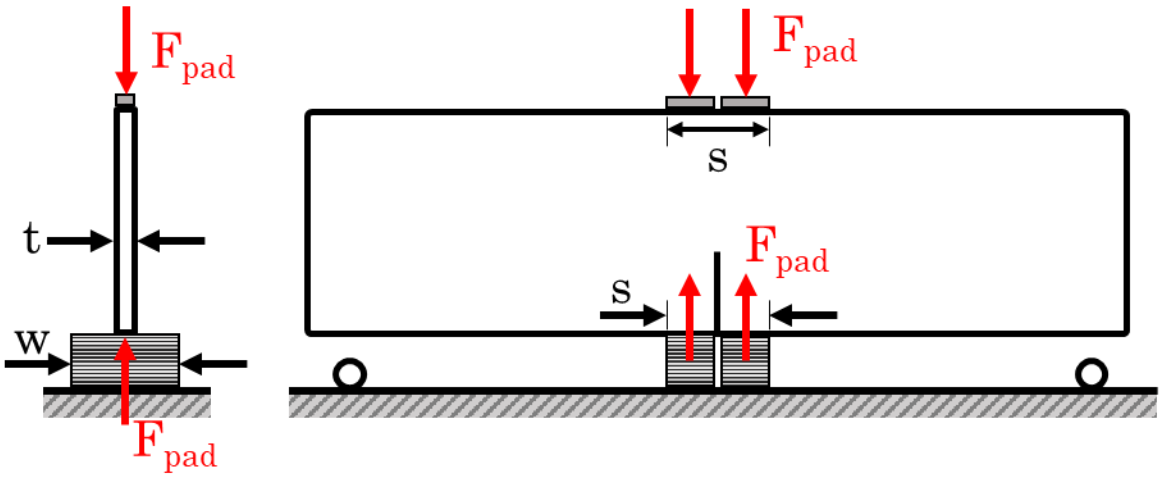

Figure 3.16 Gap Test schematic used to calculate the ξ parameter (left) side view (right) front view.

The compressive strength of the laminate σ_c is calculated analytically via the Tsai-Wu failure criterion, which is an operationally simple criterion that treats the strength of a composite laminate as a tensorial quantity [52]. For a composite material where each lamina is transversely isotropic (i.e., uni-directional) and a state of plane stress is dominate the Tsai-Wu criterion predicts that failure will not occur so long as the following inequality is satisfied [2],

$$X_1\sigma_{11} + X_2\sigma_{22} + X_{11}\sigma_{11}^2 + X_{22}\sigma_{22}^2 + X_{66}\tau_{12}^2 + 2X_{12}\sigma_{11}\sigma_{22} < 1 \tag{3.6}$$

Where the constants X_1, X_2, … are determined from the fundamental strength constants in Table 2.1 as shown,

$$\begin{aligned} X_1 &= \frac{1}{X_{1T}} - \frac{1}{X_{1c}} \\ X_{11} &= \frac{1}{X_{1T}X_{1c}} \\ X_2 &= \frac{1}{Y_{1T}} - \frac{1}{Y_{1c}} \\ X_{22} &= \frac{1}{Y_{1T}Y_{1c}} \\ X_{66} &= \frac{1}{S^2} \\ X_{12} &= -\frac{1}{2}\sqrt{X_{11}X_{22}} \end{aligned} \tag{3.7}$$

The values σ_{11}, σ_{12}, and σ_{22} denote the ply stresses that can be determined from classical lamination theory based on the specific load case. For the compressive strength σ_c a purely compressive loading case is considered, and equation (3.6) is iterated through until the inequality is no longer satisfied. This yields a compressive strength of σ_c = 701.36 MPa and then using equation (3.5) ξ = 0, 0.29, and 0.44, as previously referenced to.

3.4.2 Size Effect Analysis

Existing fracture theory such as LEFM is unable to adequately capture the fracture behavior of composites and quasi-brittle materials in general [16, 19, 30, 31, 53]. This is due to a non-negligible FPZ that develops at the crack tip during fracture and is further complicated in composites who display anisotropic behavior. As a consequence of the non-negligible FPZ quasi-brittle materials display a characteristic size effect where fracture properties are highly sensitive to structure size and a transition from ideally brittle to pseudo-plastic

behavior is observed. To analyze fracture in these materials the Bažant Type II Size Effect Law, equation (1.2), must be used which a foundational tool in Quasi-Brittle Fracture Mechanics.

The Bažant SEL is repeated below for convenience where G_f is the fracture energy, c_f

$$\sigma_N = \sigma_o(1 + D/D_o)^{-1/2} \tag{3.8}$$

$$\sigma_o = \sqrt{EG_f/c_f g'(\alpha_o)} \tag{3.9}$$

$$D_o = c_f g'(\alpha_o)/g(\alpha_o) \tag{3.10}$$

is a measure of the FPZ size, D is a characteristic structure size, and σ_N is the structural strength. Manipulation of equation (3.8) leads to the linear expression shown below,

$$\begin{gathered} \sigma_N = \sigma_o(1 + D/D_o)^{-1/2} \\ \downarrow \\ 1/{\sigma_N}^2 = 1/{\sigma_o}^2 + D/D_o{\sigma_o}^2 \\ \downarrow \\ let\ Y = 1/{\sigma_N}^2, C = 1/{\sigma_o}^2, A = 1/D_o{\sigma_o}^2 \\ \downarrow \\ \therefore\ Y = C + AD \end{gathered} \tag{3.11}$$

which is fit to the experimental data using a linear regression plot of $1/\sigma_N^2$ versus D. From the slope, A, and intercept, C, of this fit the fracture properties G_f and c_f may be determined for each data set $\xi = 0$, 0.29, and 0.44 using equations (3.9) and (3.10). That is,

$$G_f = \frac{g(\alpha_o)}{EA} \tag{3.12}$$

$$c_f = \frac{Cg(\alpha_o)}{Ag'(\alpha_o)} \tag{3.13}$$

To utilize equations (3.11), (3.12), and (3.13) the peak load values reported in section 3.3 are converted to structural strength via the application of beam theory to the 4PB loading shown in Figure 3.8 and Figure 3.16. This gives,

$$\sigma_N = \frac{3P(L - s)}{2D^2 t} \tag{3.14}$$

The aforementioned equations also require the effective modulus of elasticity of the laminate, from classical lamination theory this is calculated to be E = 83.81 GPa based on the lamina elastic constants in Table 2.1. Lastly, to determine g(α) the same process defined in section 2.2 in conjunction with equation (2.5) is used although multiple simulations are run at differing α values to obtain g as a function of α as opposed to a point value. A polynomial is then fit to these FEA results and its derivative evaluated to find g′(α). The resulting g(α) and g′(α) plots from this analysis are shown in Figure 3.17, $\alpha_o = 0.5$ in all the currently presented Gap Test data which corresponds to g(α) = 6.7176 and g′(α) = 41.352. The polynomial

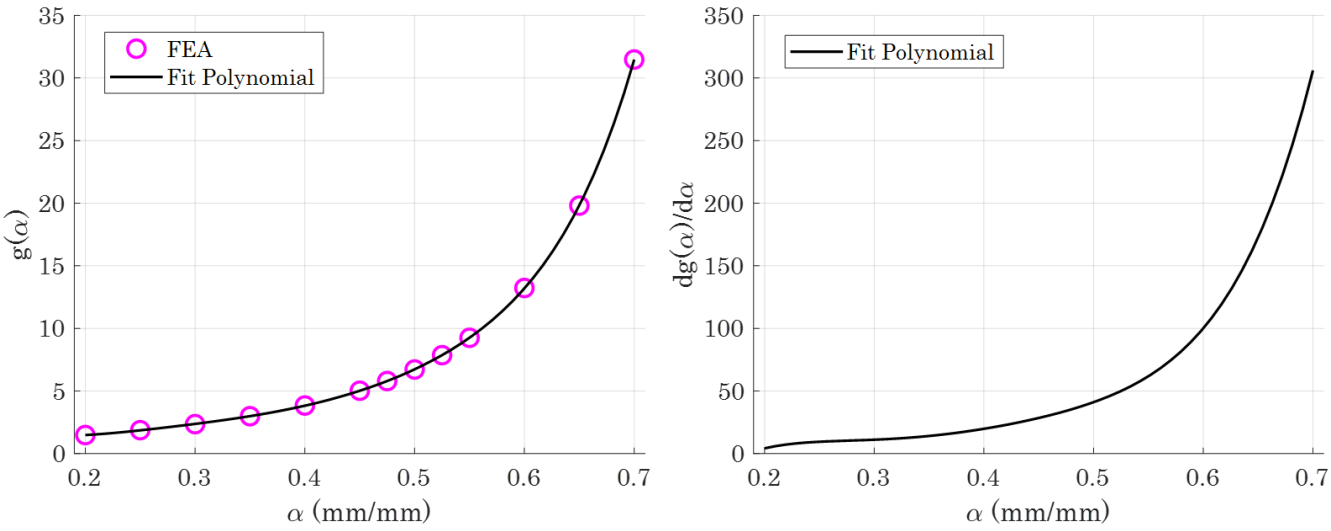

Figure 3.17 FEA simulation results for (left) the dimensionless energy release rate g(α) and (right) its derivative g'(α) as a function of the normalized crack length α = a/D.

expression found for g(α) is given in equation (3.15) which is unique to the specific geometry used in this Gap Test configuration and applicable elsewhere only so long as the geometric dimensions are scaled exactly. Also, the composite laminates are homogenized through the thickness to allow g(α) to be applied to all 3 test specimen sizes. When highly inhomogeneous materials are evaluated i.e., discontinuous fiber composites, g(α) is not consistent for geometrically scaled specimens, and it is instead uniquely dependent on structure size D [54].

$$g(\alpha) = 9702.8\alpha^6 - 22089\alpha^5 + 20911\alpha^4 - 10345\alpha^3 + 2822.6\alpha^2 - 394.46\alpha + 23.223 \quad (3.15)$$

Using equation (3.11) leads to the linear regression and size effect plots shown below. Figure 3.18 is a combined linear regression plot for each ξ data set from which notable discrepancies are observed. According to LEFM the fracture energy of a material is to remain constant regardless of the ξ value, in the regression plots of Figure 3.18 this would correspond to all regression lines overlapping one another or being nearly identical within reasonable experimental noise. This trend is not observed and instead the slope increases as ξ increases which corresponds to a decrease in the fracture energy per equation (3.12). Similarly, the

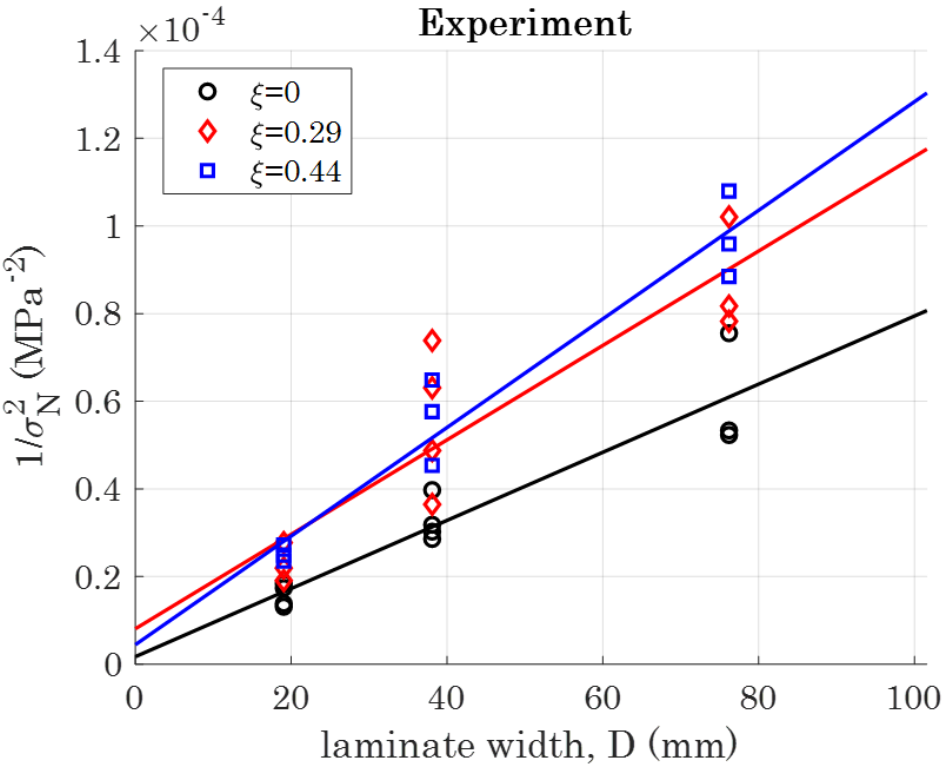

Figure 3.18 SEL linear regression plots for differing experimental ξ values.

intercepts for ξ = 0.29 and 0.44 are larger than the intercept for ξ = 0 which indicates an increase in the FPZ size (c_f value) due to the presence of a crack parallel stress. The decrease in fracture energy and increase in FPZ size are likely indicative of changing or increasing damage mechanisms at the crack tip that ultimately initiates fracture, this will be explored further in the following section. Regardless the analysis captured herein supports the hypothesis that the non-negligible FPZ in composites impacts the fracture behavior and a

crack parallel stress leads to a weakening effect via reduction of the fracture energy. Numerical values for G_f and c_f from equations (3.12)and (3.13) are in Table 3.4. The G_f values are additionally plotted in normalized forms in Figure 3.19 to highlight the degree of fluctuation that is observed, $G_{f,o}$ is the fracture energy measured for $\xi = 0$. At the highest crack parallel compression tested $\xi = 0.44$ the fracture energy is measured to be 37.2% less

ξ	G_f (N/mm)	c_f (mm)
0	102.85	0.361
0.29	74.20	1.229
0.44	64.52	0.587

Table 3.4 Calculated fracture energy G_f and FPZ size c_f for the experimental Gap Test data using Bažant's Type II Size Effect Law.

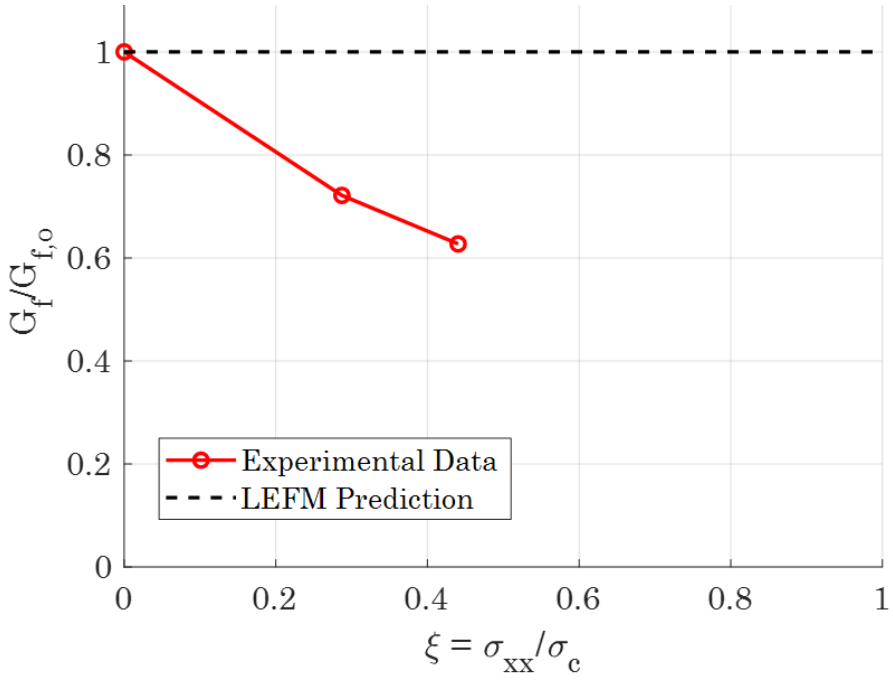

Figure 3.19 Normalized fracture energy plotted as a function of ξ. $G_{f,o}$ is the fracture energy measured for no crack parallel stress which is assumed to be constant per LEFM. Shown fracture energy values are calculated per Bažant's SEL.

less than the nominal value with no crack parallel compression – a sizeable departure that would prove dangerous in a real-world application if unaccounted for.

With the values in Table 3.4 equations (3.8), (3.9), and (3.10) may be used to assess the experimental data's fit to the classical Bažant size effect curve originally shown in Figure 1.2. These plots are included below and are broken out individually by ξ = 0, 0.29, and 0.44 for convenience. All data sets generally fit the Bažant SEL well, indicating its legitimacy as the primary means of fracture analysis in this work. As can be seen also, the data falls very

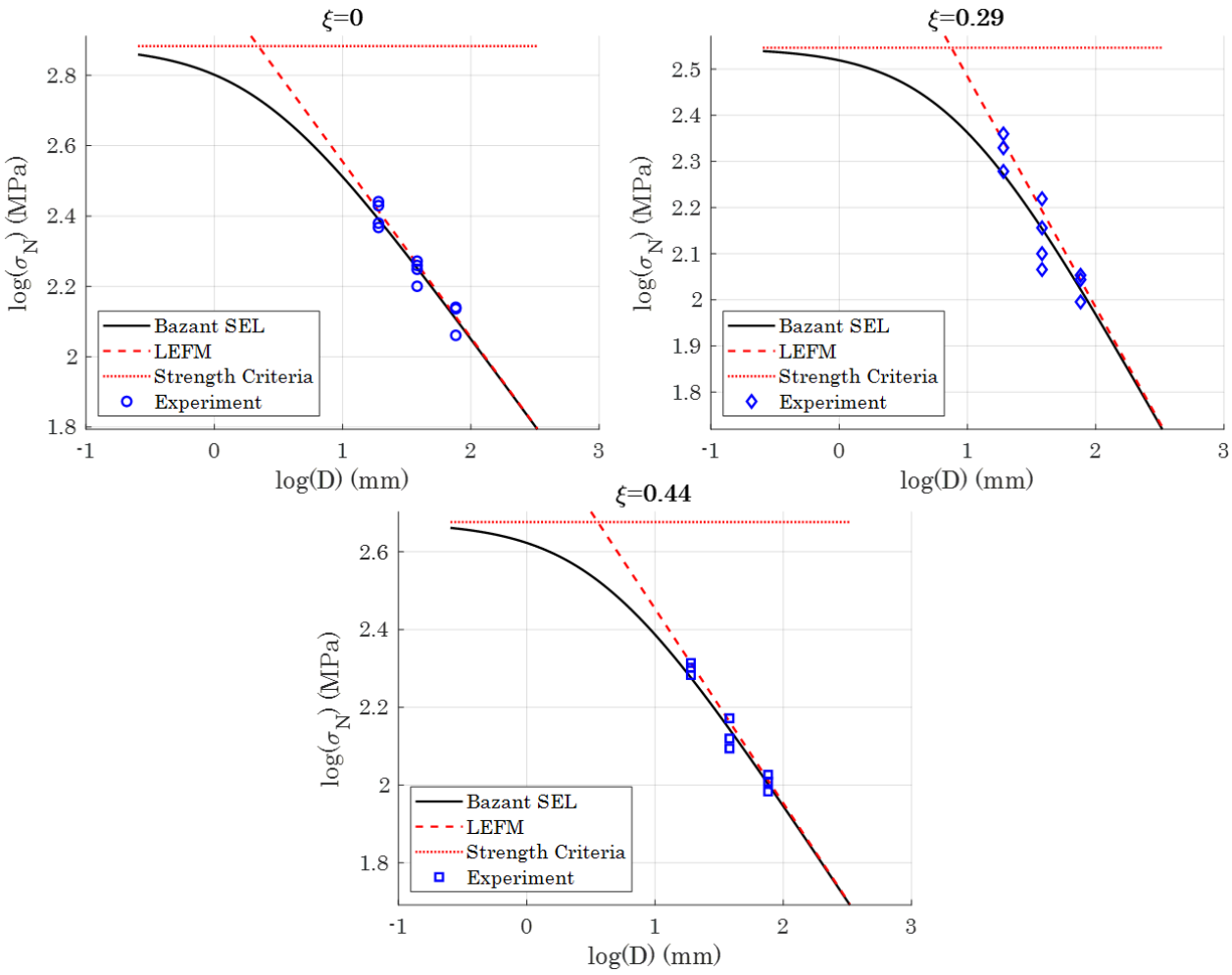

Figure 3.20 Gap Test experimental data fit to the Bažant SEL and compared against the scaling relationship predicted by LEFM and the strength criteria.

close to the LEFM asymptote showing that, for the geometry (primarily thickness and in-plane dimensions) studied in this work, LEFM does provide a reasonable estimation of the fracture scaling. Though the smaller size specimens exist approximately at the break point of the curve where the Bažant SEL and LEFM deviate and LEFM begins to overpredict the structural strength. Therefore, if smaller test specimens are evaluated, where the FPZ is more significant in size compared to the structure size and the nonlinear effects from damage within the FPZ greatly affect the structural behavior, LEFM will be insufficient and the SEL must be used.

3.4.3 Crack Tip Fractography

Strength is an elusive and at times vague term. It is applied to aspects of fatigue, creep, static and dynamic loading, uni- and multi-axial loading, and fracture, all of which are extended to consider corrosive, environmental, and geometric effects. Moreover, strength in composites is complicated by a plethora of independent and interacting failure mechanisms such as delamination, fiber breakage, matrix cracking, kink band formulation, fiber-matrix debonding, and fiber pull out [52, 55]. To the best of the author's knowledge a reliable numerical or theoretical framework for the prediction of progressive failure (and strength) in composites that is driven by the unique failure mechanisms at multiple length scales does not exist. To then diagnose the governing failure mechanism in a composite structure, or any engineering material in general, optical methods are often relied upon, grouped under a blanket term known as *Fractography*.

Due to the foregoing results the failure mechanism(s) for each of the $\xi = 0$, 0.29, and 0.44 tests are of keen interest. While the Bažant SEL provides insight to the structure's response under a crack parallel compression at the macro-scale (i.e., laminate level) the peculiarities of the composite's behavior at the meso-scale (i.e., lamina level) and micro-scale (i.e., matrix and fiber level) are unknown. In the present study an optical microscope at high magnifications is used to obtain detailed images of the composite morphology at the crack tip where the fracture initiates, specifically a Nikon Optiphot microscope at 10x, 20x, and 40x magnification via the commercial software ToupView as shown in Figure 3.21. This process is colloquially referred to as photomicroscopy (PMG). Micrographs for a $\xi = 0$ test are shown

in Figure 3.22 while those for ξ = 0.29 and 0.44 tests are in Figure 3.23 and Figure 3.24, respectively. A nuance to photomicroscopy, at least for the present application to composite

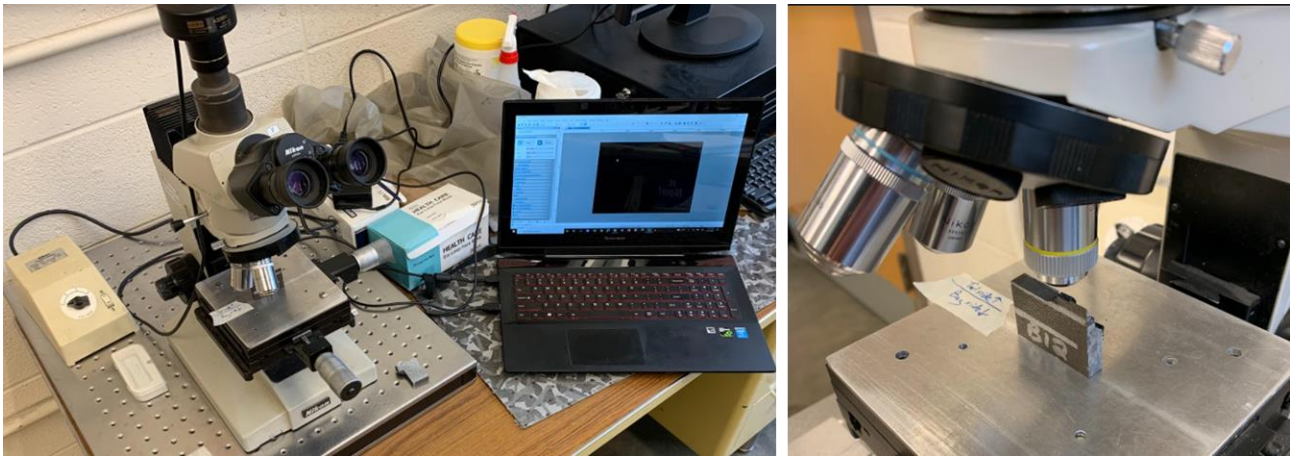

Figure 3.21 (left) photomicroscopy setup (right) test specimen in which only the crack tip has been isolated to allow imaging of the fracture morphology.

fracture surfaces, is obtaining high resolution images by focusing the focal plane on the area of interest. This can be an arduous endeavor as composite's exhibit a rough, jagged fracture surface on the meso-scale and the critical geometry often does not conveniently exist on a flat plane. As a biproduct PMG images may display areas of low resolution that are not on the focal plane and, fracture surfaces are never to be polished as such an operation will remove the fracture morphology which is the detail of most interest. In viewing the below images, the reader is to be privy to this challenge that is inherit to PMG.

The ξ = 0 test in Figure 3.22 is compared against a polished, pristine cross section. The pristine cross section shows the mesoscale structure that is, the 0° and 90° layers and their respective interfaces are easily identifiable. When viewing the fractured surface, the 90° plies (plies in the x direction) remain attached to the crack tip while the 0° plies (plies in the y direction) appear to be removed entirely, less a few remaining fibers seen at the ply interfaces. This is indicative of a tensile dominant fracture which is expected due to the normal stresses from the globally applied bending moment. For the 0° plies, who are not in fact absent but have fractured completely, fiber breakage is the observed failure mechanism. For the 90° plies, the fibers appear on a flat and smooth surface that is the fracture plane,

implying minimal fiber breakage and instead a failure in the matrix. A limitation to this analysis though, is the absence of a timescale. Whether the fracture initiated via fiber breakage in the 0° plies or matrix cracking in the 90° plies first is unknown, and additionally the interaction of these two phenomena is undefined. Conventional wisdom suggests that matrix cracking in the 0° plies due to the tensile stresses would occur first, supported by the strength parameters of Table 2.1 where X_T / Y_T = 2089.0 / 79.29 = ~26.3. Though this is not a conclusion that may be made solely based on Figure 3.22. Nonetheless, fiber breakage in the 0° plies and matrix failure in the 90° plies are observed in all the $\xi = 0$ tests which is generally the expected failure response based on the loading condition.

The fracture surfaces for a $\xi = 0.29$ test, Figure 3.23, and a $\xi = 0.44$ test, Figure 3.24, tell partially the same story as the fracture surface for a $\xi = 0$ test. Similar fiber breakage in the 0° plies and matrix failure in the 90° plies are present for the crack parallel compression tests, indicating that tensile failure is one of the mechanisms that drives crack propagation. But a considerably sized splitting crack is also observed for the $\xi = 0.29$ and $\xi = 0.44$ tests. Observationally the anatomy of these splitting cracks is always the same: one single splitting crack is present for each $\xi = 0.29$ or 0.44 test, the splitting cracks only exist in the 0° plies, and the splitting crack is close to the laminate midplane though never exactly at the midplane. Additionally, the width of the resulting splitting cracks is higher in the $\xi = 0.44$ specimens than it is in the $\xi = 0.29$ specimens. Inspection of the micrographs for each ξ level confirms that the presence of a crack parallel compression leads to a change in the fracture morphology which offers a possible explanation for the reduction in fracture energy that is shown in the previous sections. Via the initiation of a new and or additional failure mechanism it is likely that the crack propagates sooner and hence the load bearing capacity of the structure, and concomitantly the fracture energy, is reduced.

However, this finding also complicates the present effort of diagnosing the crack initiation mechanism for $\xi = 0.29$ and $\xi = 0.44$. Previous researchers [56] performed 3PB tests on notched and un-notched composite specimens and showed that splitting cracks initiate mainly at the fiber/matrix interface, but also in the matrix, due to the high dilatational energy density at the interface. This damage then triggers localized crack propagation and ultimately catastrophic failure of the structure [57]. Unfortunately, though, due to the

complex morphology at the crack tip of the Gap Test specimens these results from the literature are insufficient to uniquely define the crack initiation mechanism. In Figure 3.23 and Figure 3.24 three different failure mechanisms are present – fiber breakage, matrix failure, and splitting cracks. And as before, the absence of a timescale in this analysis precludes one from isolating the governing failure mechanism from this list. To answer this question the Gap Test may be ran up to a percentage of the known peak load (i.e., $0.9P_{max}$), unloaded, and then the fracture surface analyzed as was done above. This will allow the identification of the first failure mechanism that manifests at the crack tip and consequently what micro- and meso-scale behavior dominates the structural strength in the presence of a crack parallel compression. The execution of this effort is left for future works due to current time constraints for the author.

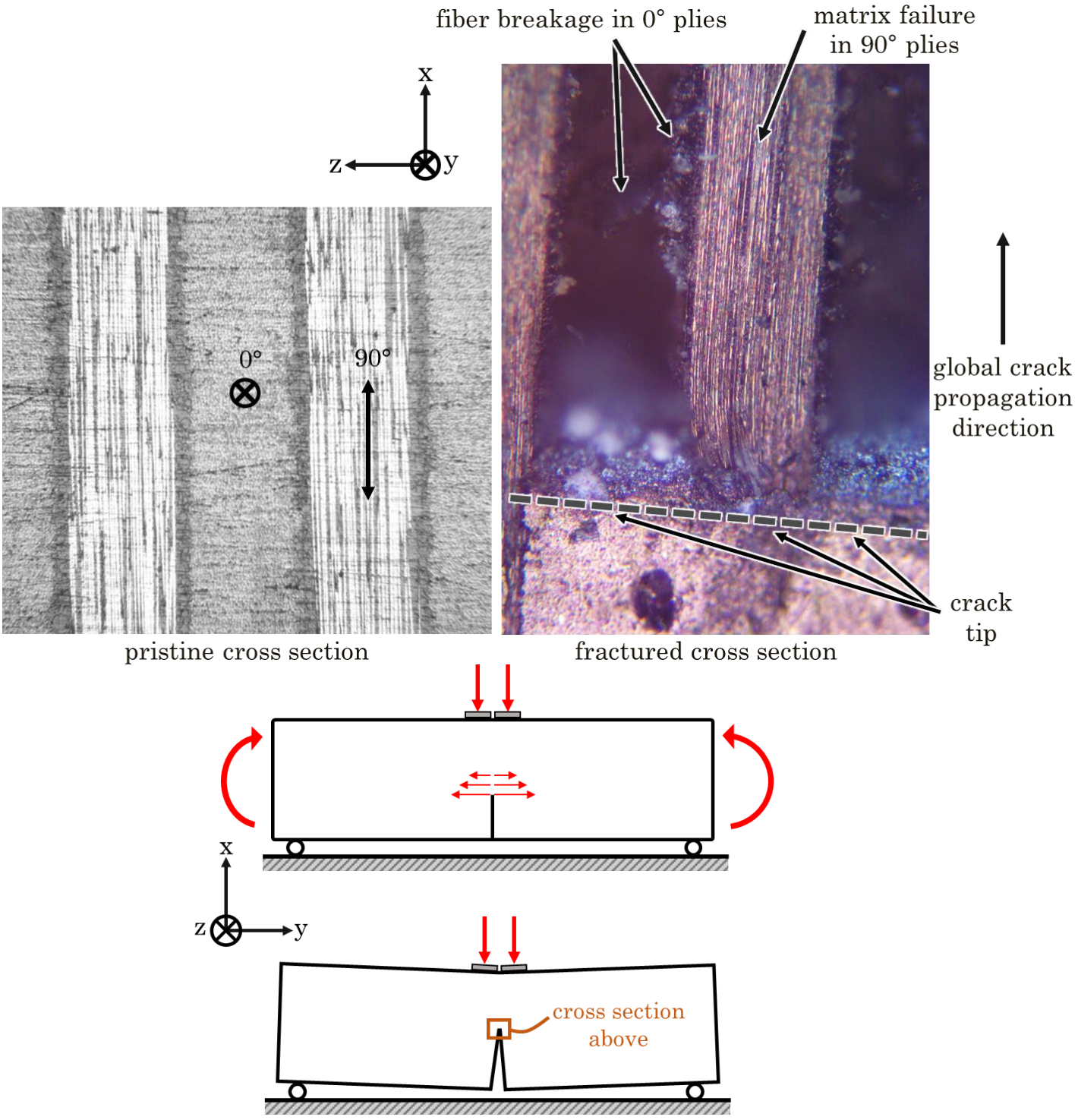

Figure 3.22 Representative micrograph of the crack tip morphology in a $\xi = 0$ test where fiber breakage in the 0° plies and matrix failure in 90° plies is observed. The fracture surface is compared against a pristine cross section which shows the mesoscale morphology prior to fracture.

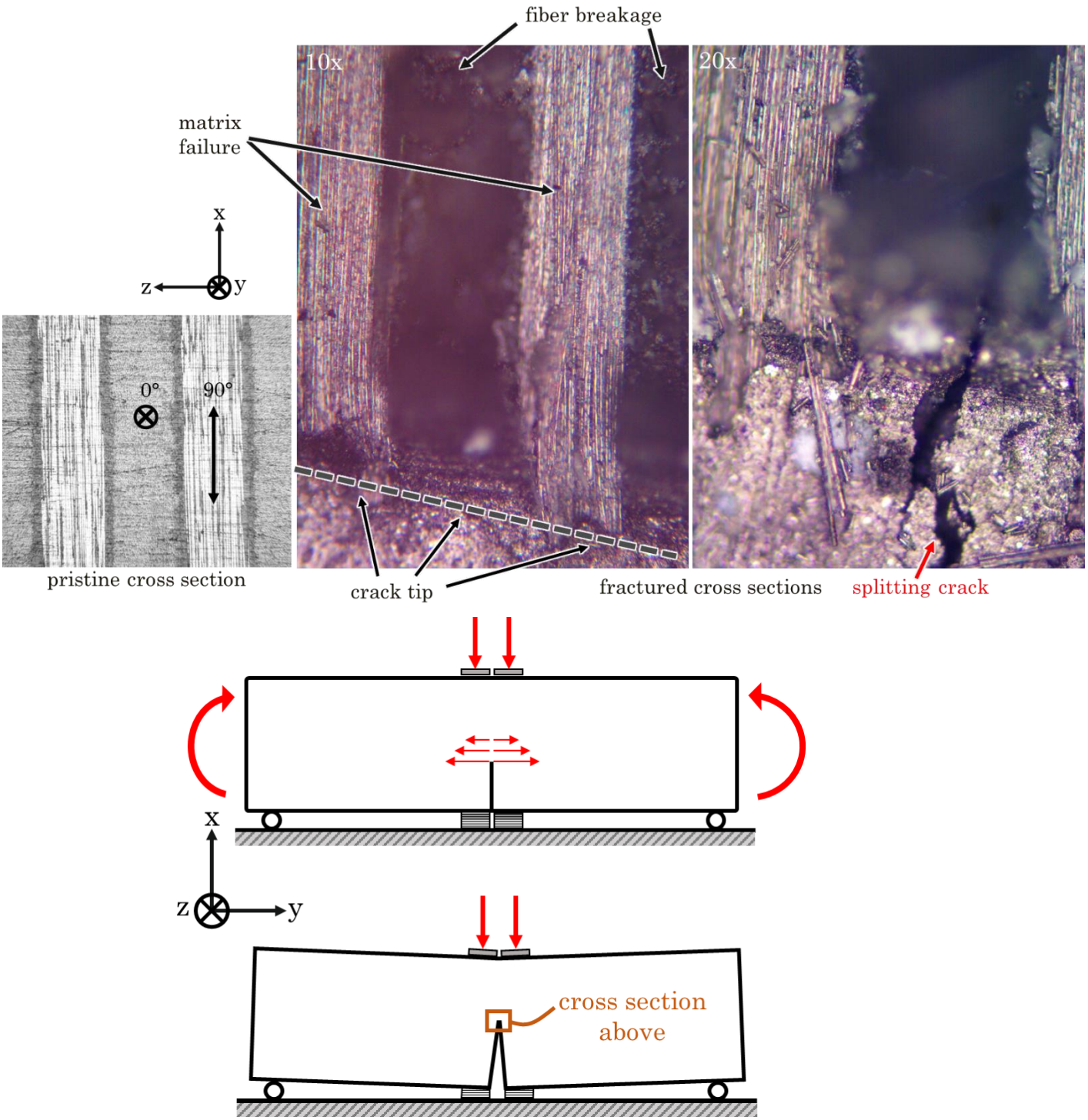

Figure 3.23 Representative micrograph of the crack tip morphology in a $\xi = 0.29$ test. The observed fracture surface displays similar fiber breakage and matrix failure to the $\xi = 0$ tests although, a significant splitting crack is now present due to the crack parallel compression.

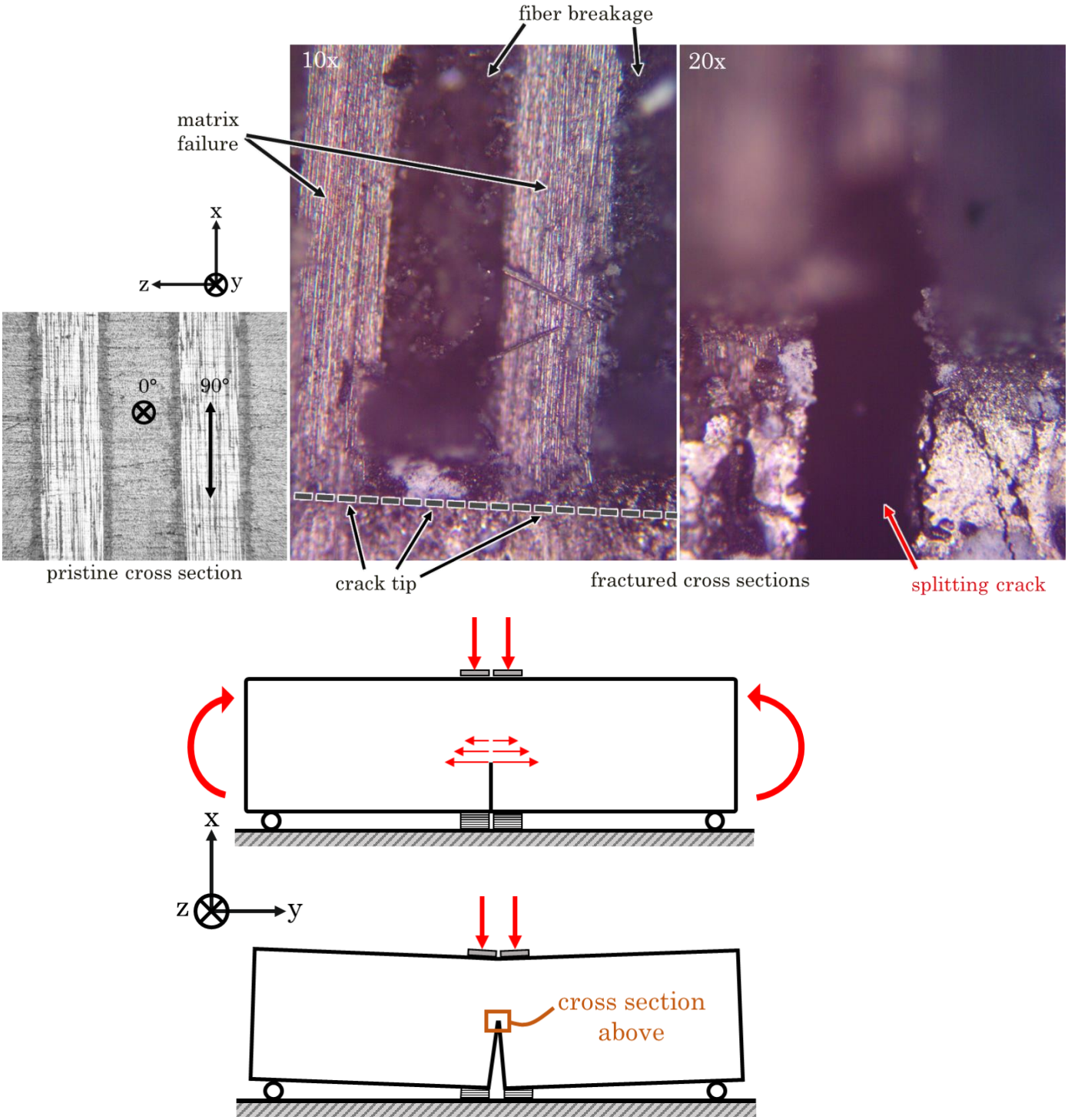

Figure 3.24 Representative micrograph of the crack tip morphology in a $\xi = 0.44$ test. The observed fracture surface displays similar fiber breakage and matrix failure to the $\xi = 0$ tests although, a significant splitting crack is now present due to the crack parallel compression. The size of the splitting crack also increases as ξ increases.

3.4.4 Digital Image Correlation

Displacement in the Gap Tests is measured two ways – one via a transducer on the load frame and one via digital image correlation (DIC), which is done due to the load frame displacement being intrinsically less accurate. This is because the load frame and test fixture have a small but finite compliance that allows it to displace during testing. A phenomenon that is exacerbated when the load frame transducer is located far from the test specimen as is the case for the current test setup. To rectify this undesirable behavior DIC measures the displacement directly on the test specimen, removing any effects of the machine compliance. This is a correction that proves paramount in the ensuing chapter where FEA models are calibrated against the experimental data. And as a note, in the foregoing fracture energy analysis only the peak load is used which is unaffected by the differences in displacement from DIC or the load frame transducer.

The compliance of the load frame and test fixture may be quantified by modeling the entire test setup as two springs in series as shown in Figure 3.25. Here one spring denotes the test specimen, and the other is an effective machine spring that groups together the load

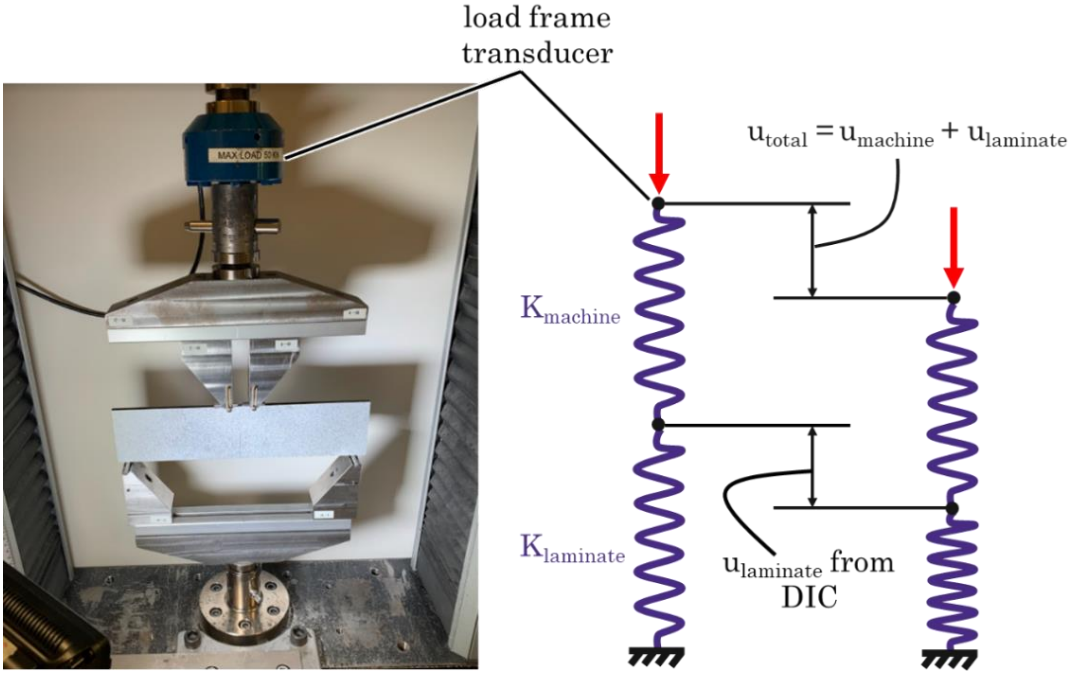

Figure 3.25 Gap Test setup idealized as 2 springs in series, u refers to displacement and K refers to stiffness.

frame, grips, fixture, lubrication, etc. In this idealization the force is constant in both springs and thus the relative stiffnesses of the machine versus the test specimens may be calculated from equation (3.16); the load frame transducer measures total displacement and DIC measures the laminate displacement. This data is compiled in Table 3.5 for each specimen size for the $\xi = 0$ tests where it is seen that the machine stiffness is approximately an order of magnitude larger than the test specimen stiffnesses.

$$\begin{gathered} u_{total} = u_{machine} + u_{laminate} \\ \downarrow \\ \frac{F_{total}}{K_{total}} = \frac{F_{machine}}{K_{machine}} + \frac{F_{laminate}}{K_{laminate}} \\ \downarrow \\ assume\ constant\ force \\ \downarrow \\ \frac{1}{K_{total}} = \frac{1}{K_{machine}} + \frac{1}{K_{laminate}} \\ \downarrow \\ \therefore \frac{K_{laminate}}{K_{machine}} = \frac{K_{laminate}}{K_{total}} - 1 \end{gathered} \tag{3.16}$$

Size	Avg. $K_{laminate}$ (N/mm)	Avg. $K_{machine}$ (N/mm)	Avg. $K_{laminate}/ K_{machine}$
Small	6173.78	58749.97	0.1050
Medium	5668.01	36736.62	0.1542
Large	4774.08	46449.50	0.1027

Table 3.5 Measured machine versus test specimen stiffnesses for $\xi = 0$ Gap Tests.

DIC also augments the load-line displacement that is output from the load frame transducer, which is a one-dimensional point value. DIC illustrates the displacement and strain fields on the surface of the test specimen and most critically, the development of the strain field adjacent to the crack tip. This is immensely beneficial as it elucidates the crack tip stresses while also being a surface representation of the FPZ and its evolution. DIC images showing the progression of the maximum principal strain for a $\xi = 0$ test are captured

in Figure 3.26 while similar images for a $\xi > 0$ test are in Figure 3.27. Both for tests with and without crack parallel compression the highest intensity strain field originates at the crack tip and proceeds to increase in size as the applied load increases, an expected phenomenon due to the stress concentrations that develop at the crack tip [58]. For $\xi > 0$ tests the size of the intensified strain field at fracture is generally less than that in a $\xi = 0$ test, an observation that supports the preceding results of a reduction in fracture energy as ξ increases. This is due to the additional damage that is induced within the FPZ from the crack parallel compression, as shown in Figure 3.23 and Figure 3.24, which in turn reduces the structure's capacity to resist fracture and therefore the magnitude of the strain field (and consequently stress field) is lesser at failure. 0

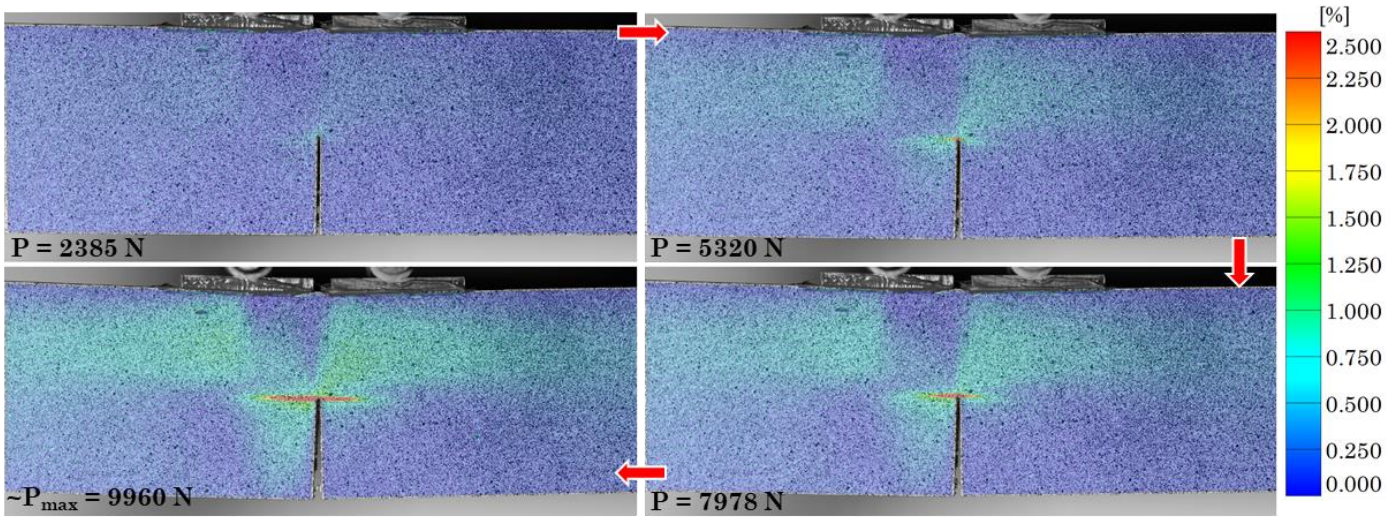

Figure 3.26 Maximum principal strain field evolution in a $\xi = 0$ test on a medium size specimen. Shown strain field is representative of all $\xi = 0$ tests.

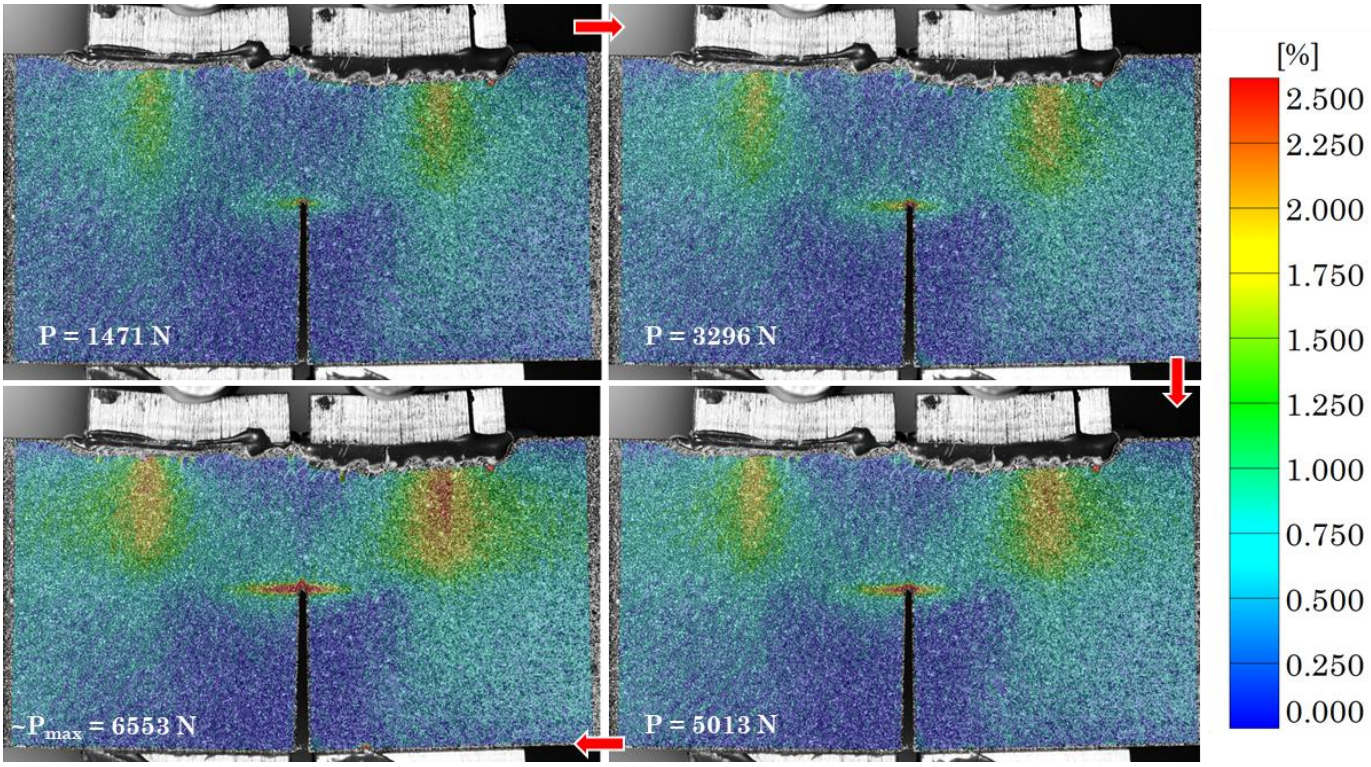

Figure 3.27 Maximum principal strain field evolution in a $\xi = 0.29$ test on a medium size specimen. Shown strain field is representative of all $\xi > 0$ tests

Chapter 4 Computational Gap Test, Results and Analysis

4.1 Motivation

The foregoing experimental campaign is buttressed with a thorough computational campaign whose details are found within this chapter. This is done to provide a computational framework that can capture the crack parallel compression effects observed in the Gap Test. Such an effort is tremendously important due to the current prevalence of composite materials in industry whose strength may be dangerously weaker than expected in the presence of a crack parallel compression. To this end, a computational framework allows the practicing engineer to appropriately model and predict a composite structure's behavior when crack parallel compression is experienced. Furthermore, correct modelling definition obviates the need to undertake a large experimental effort as done in this study. Designing, developing, and manufacturing the Gap Test to be executed in many different laboratory settings on different materials is an expensive endeavor which simply may not be feasible for some academic or industry researchers. But many FEA resources are available in the modern day, particularly due to the momentous development in computational power, which enables the interested researcher to model and simulate crack parallel compression on their specific structure and or material.

4.2 Model Definition

To corroborate the experimental Gap Test results a crack band modeling approach [59] is employed via Abaqus-Explicit 2020 simulations. The crack band model allows the inclusion of all the stress components in a material which, due to the presence of a finite width FPZ, plays a major role in fracture initiation of quasi-brittle media [30, 31]. For the present application, the crack band model is an absolutely imperative detail to capture the effects of a crack parallel compression. As has been previously stated traditional fracture theory and modeling approaches consider cracks as a line that is perfectly sharp. If such an approach is used currently it will be impossible to capture the influence of a crack parallel compression on fracture. To support this claim two different failure modeling techniques are leveraged – a Hashin damage law which is fully tensorial and a cohesive element model with a reduced

tensorial damage law. These two approaches and their results are expounded upon in the subsections below.

To computationally repeat the Gap Tests each specimen size listed in Table 2.2 is modeled with geometry, boundary conditions, and loading that replicates the experimental conditions. Images of $\xi = 0$ and $\xi > 0$ models are shown in Figure 4.1 and Figure 4.2, respectively. Here the roller pins are modeled as discrete rigids that are incapable of deforming while also being frictionless to allow tangential sliding of the test specimens without penalty. The frictionless assumption is justified due to the pins in the experiment being precision ground and lubricated. To mimic the load frame displacement of the experiments a reference point at the midpoint of the laminate is tied to nodes that are deliberately placed where the top cauls in the experiments distribute load from the load frame to the test specimens. A displacement boundary condition is applied to this reference point and the resulting nodal forces and displacement at the reference point are tabulated to give an identical comparison of the experimental force-displacement data to the computational force-displacement data. The composite laminates are modeled with the

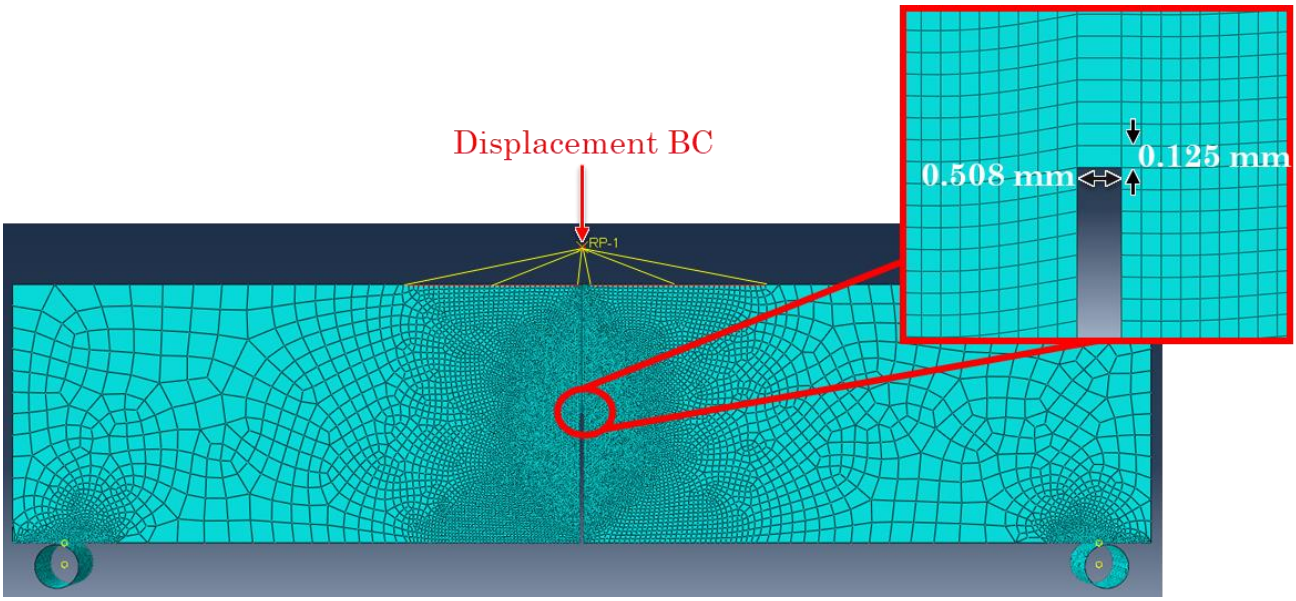

Figure 4.1 FEA model detail for a $\xi = 0$ simulation. Crack band geometry is shown in the red bounded box.

material properties in Table 2.1 and meshed with linear reduced integration continuum shell elements S4R to allow use of the Hashin damage law that is built into Abaqus. For $\xi > 0$ models the polypropylene pads are modeled with elastic and plastic behavior from the data acquired in Figure 2.6 and meshed with linear reduced integration brick elements C3D8R. The elements used within the crack band are dependent upon the specific damage law adopted, these details are shared in the subsections below.

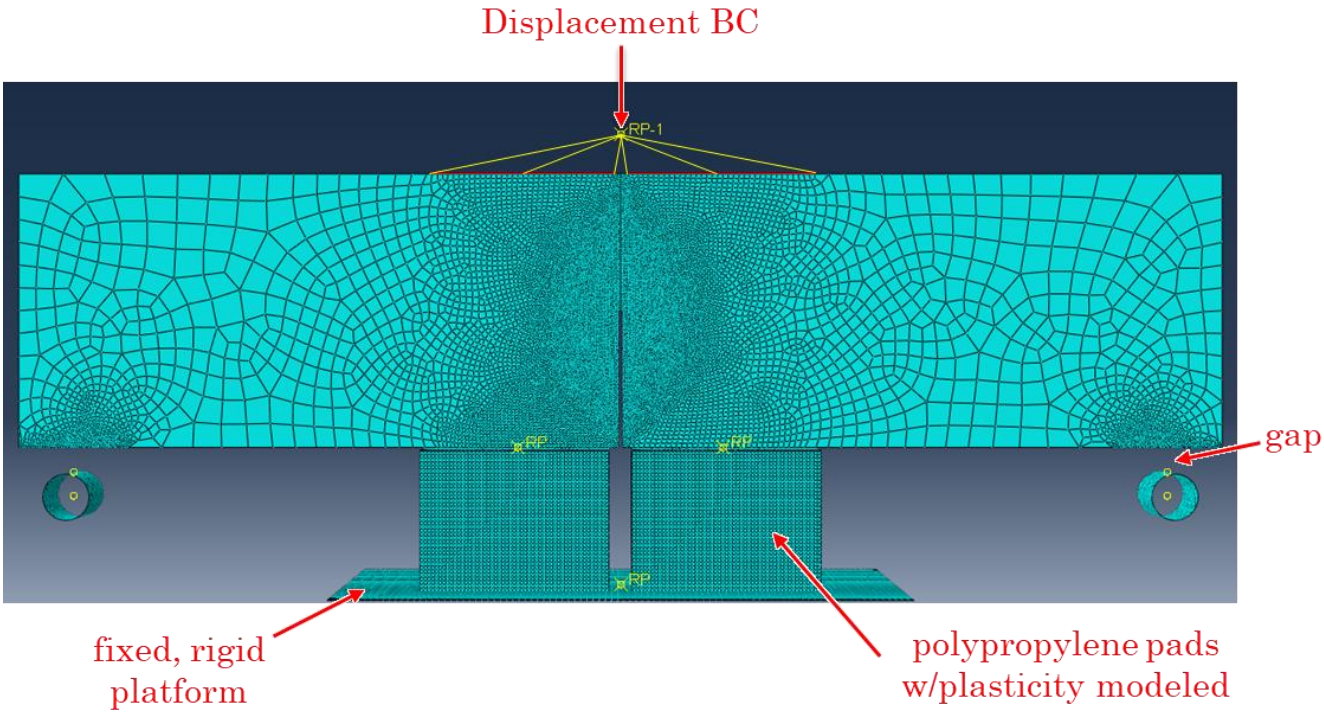

Figure 4.2 FEA model detail for a $\xi > 0$ simulation.

4.2.1 Crack Band with Hashin Damage

The Hashin damage law [60] predicts failure in a transversely isotropic material (all uni-directional composites are transversely isotropic [2]) when equation (4.1) is true.

$$A_1 I_1 + B_1 I_1^2 + A_2 I_2 + B_2 I_2^2 + C_{12} I_1 I_2 + A_3 I_3 + A_4 I_4 = 1 \tag{4.1}$$

Where I_i denotes the invariants of the stress tensor given by equation (4.2) below

$$
\begin{aligned}
I_1 &= \sigma_{11} \\
I_2 &= \sigma_{22} + \sigma_{33} \\
I_3 &= \sigma_{23}^2 - \sigma_{22}\sigma_{33} \\
I_4 &= \sigma_{12}^2 + \sigma_{13}^2
\end{aligned}
\tag{4.2}
$$

and A_i, B_i, and C_i are constants determined from the lamina strength properties given in Table 2.1. The terms σ_{ij} are the stress tensor components referenced to the principal material coordinate system which is illustrated in Figure 4.3 for a unidirectional lamina. Based on

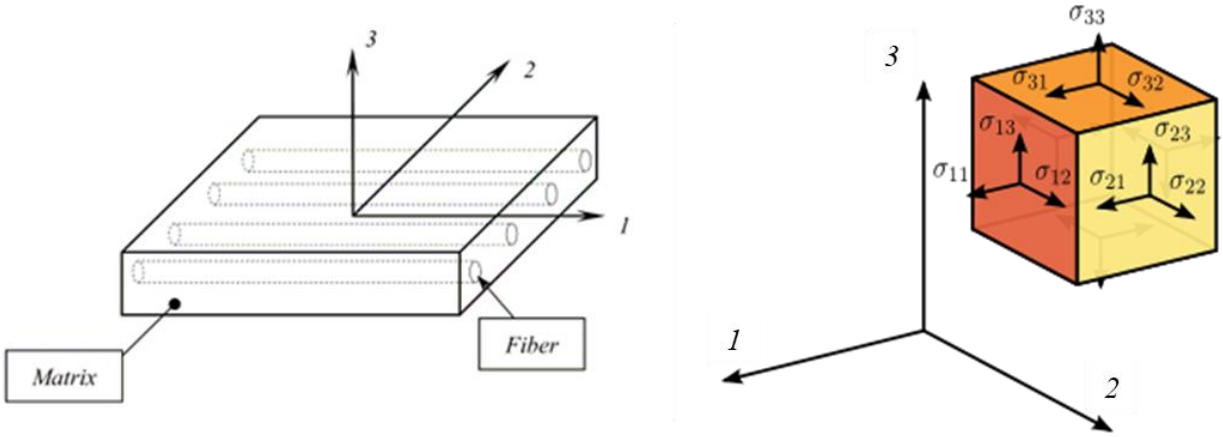

Figure 4.3 (left) uni-directional lamina principal material coordinate system [61] (right) infinitesimal stress cube showing the 3D stress tensor components, of which $\sigma_{ij} = \sigma_{ji}$ as the stress tensor is symmetric [62]

further work by Zvi Hashin equations (4.1) and (4.2) are applied to distinguish between and predict specific damage initiation mechanisms in a composite, as shown below. Note that these equations are predicated upon a plane stress condition which is generally a safe assumption for thin composite laminates. The assumptions leading to equations (4.3)-(4.6) are not discussed presently though a cogent review is provided in the original journal publication that is available in the public domain [60].

Fiber Tension:

$$
\left(\frac{\sigma_{11}}{X_T}\right)^2 + \left(\frac{\sigma_{12}}{S}\right)^2 = 1 \tag{4.3}
$$

Fiber Compression:

$$\left(\frac{\sigma_{11}}{X_C}\right)^2 = 1 \tag{4.4}$$

Matrix Tension:

$$\left(\frac{\sigma_{22}}{Y_T}\right)^2 + \left(\frac{\sigma_{12}}{S}\right)^2 = 1 \tag{4.5}$$

Matrix Compression:

$$\left(\frac{\sigma_{22}}{2S}\right)^2 + \left[\left(\frac{Y_C}{2S}\right)^2 - 1\right]\frac{\sigma_{22}}{Y_C} + \left(\frac{\sigma_{12}}{S}\right)^2 = 1 \tag{4.6}$$

For the plane stress assumption that drives equations (4.3)-(4.6) the 3D stress tensor shown in Figure 4.3 is reduced to a plane 2 by 2 tensor as shown in Figure 4.4. Because the Hashin criteria introduced above considers all these stress components within its failure criteria it is deemed a fully tensorial damage law, as referenced to multiple times in the preceding text.

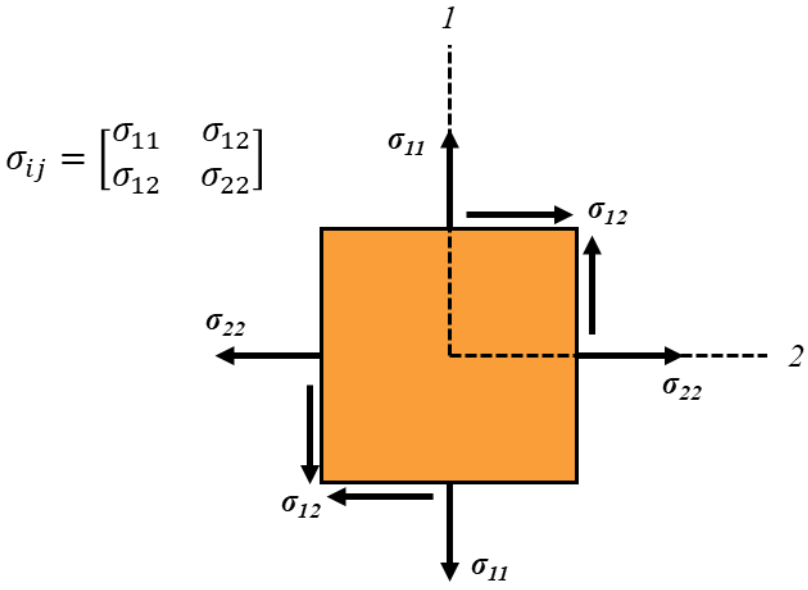

Figure 4.4 Reduced stress tensor for the case of plane stress used in the Hashin failure criteria in composites.

Now consider the stress state in front of the crack tip in the Gap Test which is biaxial due to the compressive and bending stresses, as shown in Figure 4.5. It is known that quasi-brittle materials exhibit a finite width FPZ and hence none of the in-plane dimensions of the crack, or effective crack that is the FPZ, are negligible. This implies that both the bending

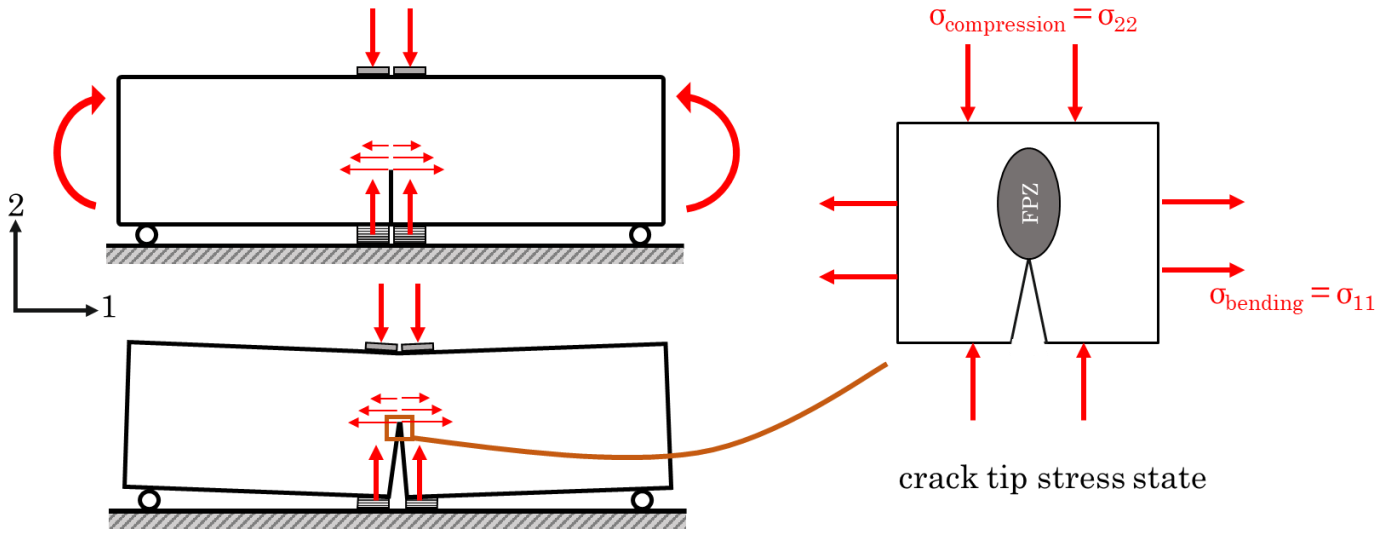

Figure 4.5 Crack tip stresses experienced during the Gap Test.

and compressive stresses will influence the crack propagation behavior. And further, if any fiber waviness or misalignment is present shear stresses will also develop in the FPZ due to the compression and bending stresses. Therefore all 3 stress components σ_{11}, σ_{12}, and σ_{22} must be included in the failure criteria used when computationally modeling the Gap Test. Because equations (4.3)-(4.6) satisfy this requirement the Hashin damage criteria is used to predict failure in the crack band. This is achieved by simply meshing the crack band with identical elements that model the adjacent composite laminate, continuum shell S4R elements.

4.2.2 Crack Band with Cohesive Elements

To further support the above reasoning the crack band is also modeled with a simpler, reduced tensorial damage law that is incapable of considering all the experienced crack tip stresses σ_{11}, σ_{12}, and σ_{22}. This serves to solidify two arguments, (1) a fully tensorial damage law is necessary to capture crack parallel compression effects and (2) the use of a reduced

tensorial damage law, that only considers the 3 traditional modes of fracture shown in Figure 1.3, can dangerously overpredict structural strength even when the crack band model is employed. This is accomplished by meshing the crack band with cohesive elements COH3D8 [63] and a maximum stress failure criterion (referred to as Maxs Damage in Abaqus) whilst leaving the remainder of the model identical to the previous simulations in section 4.2.1.

The constitutive relationship for a cohesive element is given via a linear elastic traction separation law that consists of one normal stress and two shear stresses, one in-plane and one out-of-plane [64]. These stress components are also uncoupled. Figure 4.6 below shows these stress components while equation (4.7) gives their standard mathematical representation, ε denotes the corresponding strain component and E, G are elastic constants.

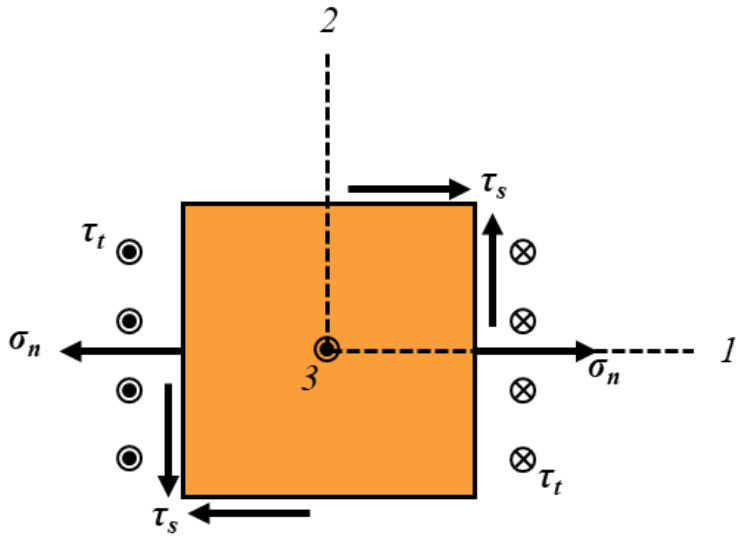

Figure 4.6 Stress state defined when using cohesive elements. σ_n is an in-plane normal stress, τ_s is an in-plane shear stress, and τ_t is an out-of-plane shear stress.

$$\begin{Bmatrix} \sigma_n \\ \tau_s \\ \tau_t \end{Bmatrix} = \begin{bmatrix} E_n & 0 & 0 \\ 0 & G_s & 0 \\ 0 & 0 & G_t \end{bmatrix} \begin{Bmatrix} \epsilon_n \\ \epsilon_s \\ \epsilon_t \end{Bmatrix} \tag{4.7}$$

Note that when this constitutive relationship is used to model the crack band it may only experience stresses that coincide with the 3 traditional fracture modes defined in LEFM – σ_n is an opening stress (Mode I), τ_s is in-plane shear (Mode II), and τ_t is out-of-plane shear (Mode

III). This effectively reduces the crack band model to a line crack model. More importantly though, fracture initiation occurs when any of the stress components σ_n, τ_s, or τ_t reach a critical value. This is represented by equation (4.8) where $\sigma_{n,crit}$, $\tau_{s,crit}$, and $\tau_{t,crit}$ refer to nominal material strengths for each mode of loading.

$$max\left\{\frac{|\sigma_n|}{\sigma_{n,crit}}, \quad \frac{\tau_s}{\tau_{s,crit}}, \quad \frac{\tau_t}{\tau_{t,crit}}\right\} = 1 \tag{4.8}$$

Combining equation (4.7) and (4.8) results in equation (4.9), which is the tensorial damage law used presently to define the cohesive elements in the crack band.

$$\begin{Bmatrix}\sigma_n\\ \tau_s\\ \tau_t\end{Bmatrix} = (1-D)\begin{bmatrix}E_n & 0 & 0\\ 0 & G_s & 0\\ 0 & 0 & G_t\end{bmatrix}\begin{Bmatrix}\epsilon_n\\ \epsilon_s\\ \epsilon_t\end{Bmatrix} \tag{4.9}$$

In this equation D is a damage variable that monotonically increases from 0 to 1 upon further loading after damage has initiated per equation (4.8). As is quickly noticed, equation (4.9) is incapable of capturing a crack parallel compression due to the simplicity of the tensorial damage law. Thus, when cohesive elements are used with a reduced tensorial damage law in the crack band the experimental results observed in Chapter 3 are impossible to capture. This point is further illustrated in Figure 4.7.

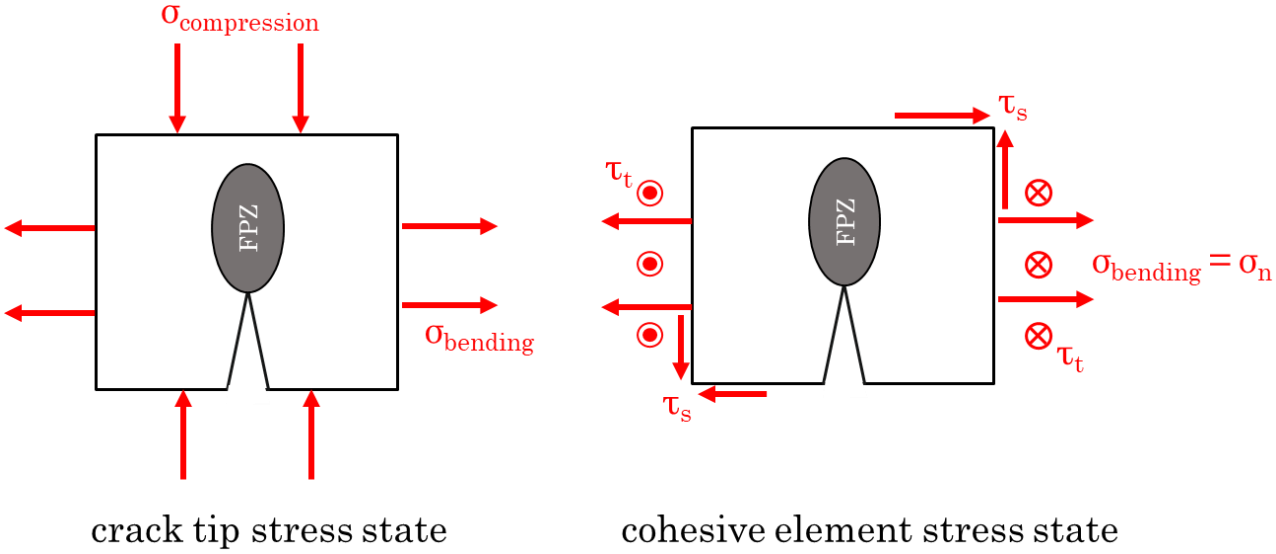

Figure 4.7 Comparative schematic of (left) the actual crack tip stresses during the Gap Test and (right) the stress state captured in a cohesive element. Notice that the cohesive element does not capture the effects of a crack parallel compression.

4.3 Results

Based on the previous model definition Gap Test simulations are ran for the small, medium, and large size test specimens at compression levels of $\xi = 0$, 0.29, and 0.44. This is repeated for 2 tensorial damage laws – a fully tensorial Hashin damage law and a reduced tensorial maximum stress damage law implemented with cohesive elements – for a total of 18 simulations. The results of which are shared in the current section.

For the Hashin damage law all the needed material properties for the computational model are standard properties given in Table 2.1 and the experimentally determined fracture energy in Table 3.4. But for the cohesive element model there are 3 non-standard properties needed that are not readily available: $\sigma_{n,crit}$, $\tau_{s,crit}$, and $\tau_{t,crit}$ which denote the material strengths as defined in Figure 4.6. Note that when cohesive elements model the crack band, the crack band is homogenized through the thickness and $\sigma_{n,crit}$, $\tau_{s,crit}$, and $\tau_{t,crit}$ represent smeared strengths of the composite laminate. Because of such the Tsai-Wu failure criterion [52] introduced in section 3.4 is used to predict the laminate strength and provide an initial guess for $\sigma_{n,crit}$, $\tau_{s,crit}$, and $\tau_{t,crit}$. To gauge the accuracy of these parameters $\xi = 0$ simulations are ran and checked against the $\xi = 0$ experimental data. The $\sigma_{n,crit}$, $\tau_{s,crit}$, and $\tau_{t,crit}$ values are then iteratively updated until the $\xi = 0$ simulations match the $\xi = 0$ experiments, a process often referred to as 'calibrating' an FEA model. The calibrated $\sigma_{n,crit}$, $\tau_{s,crit}$, and $\tau_{t,crit}$ values are listed in Table 4.1 while a comparative force-displacement plot of the $\xi = 0$ simulations and experiments is shown in Figure 4.9. An identical force-displacement plot is given in Figure 4.8 for shell elements and the Hashin damage law in the crack band, which requires no calibration as the model is deterministic based on the known elastic constants and material strengths. Note that the DIC measured displacement is now used in Figure 4.8 and Figure 4.9 as the FEA model is unable to capture the load frame compliance that is intertwined in the load frame displacement measurement. This does not affect the experimental peak load values, only a slight increase in stiffness results.

$\sigma_{n,crit}$	$\tau_{s,crit}$	$\tau_{t,crit}$
600	104.4	104.4

*all units MPa

Table 4.1 Calibrated strength parameters used when modeling the crack band with cohesive elements.

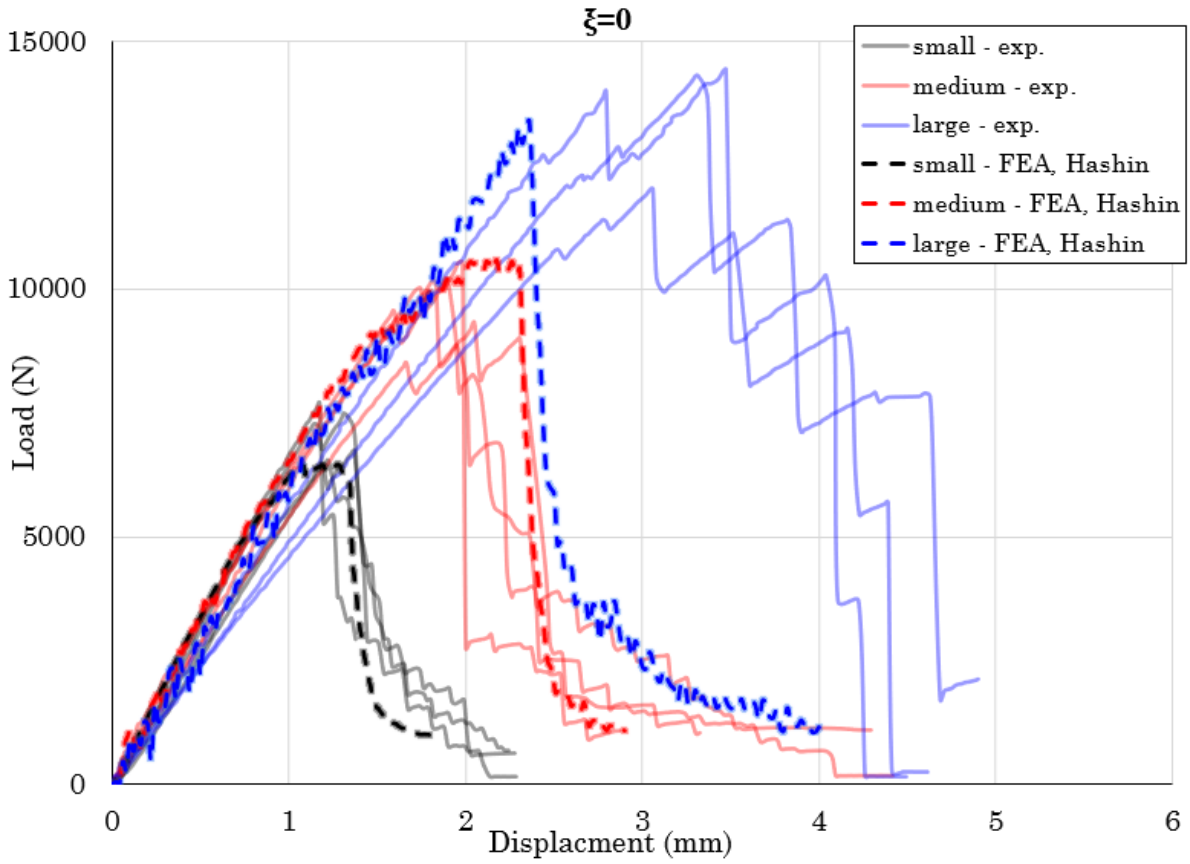

Figure 4.8 Experimental force-displacement data for ξ = 0 (solid lines) superimposed with simulated data (dashed lines) when Hashin damage models the crack band. Note that this experimental data now uses DIC displacement measurements as opposed to the load frame displacement.

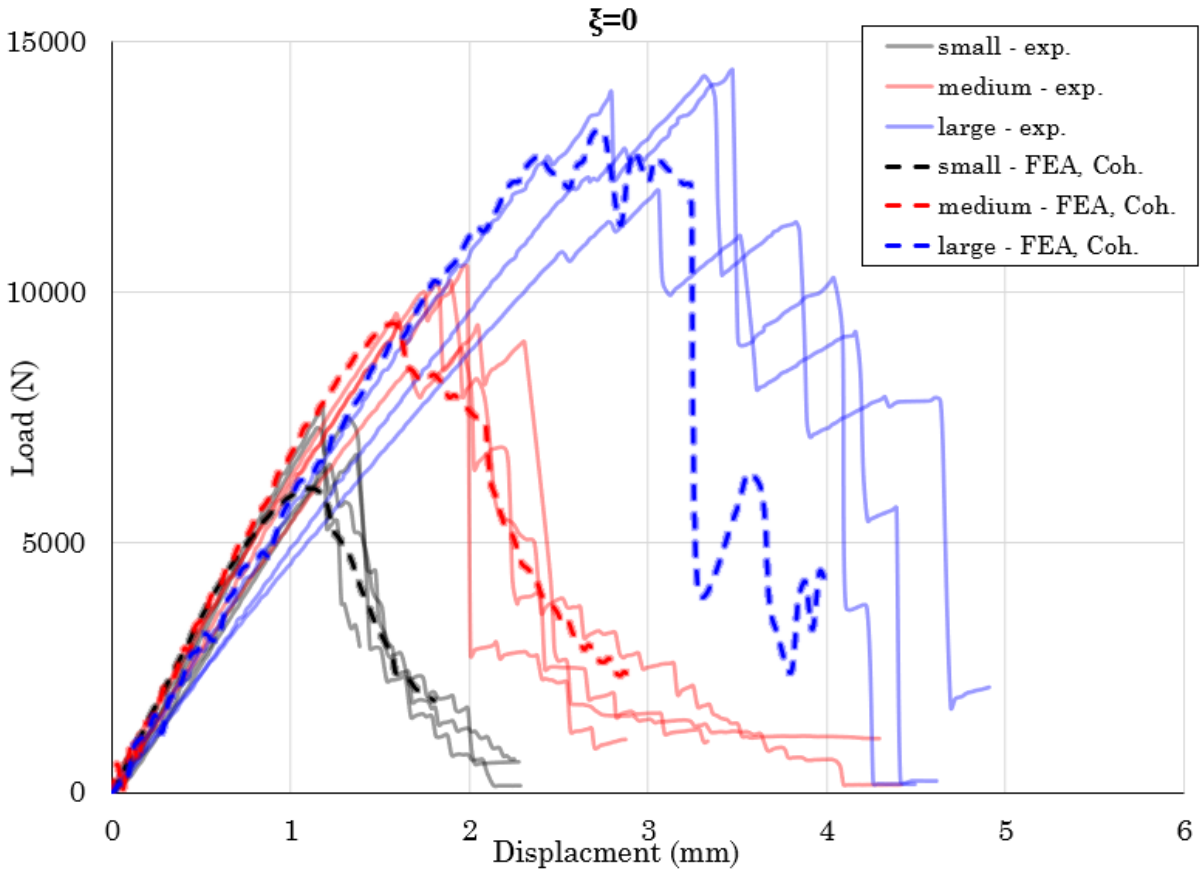

Figure 4.9 Experimental force-displacement data for $\xi = 0$ (solid lines) superimposed with simulated data (dashed lines) when Cohesive elements model the crack band. Note that this experimental data now uses DIC displacement measurements as opposed to the load frame displacement.

Both computational models do a sufficient job of matching the experimental $\xi = 0$ data – the stiffness, strength, and post peak response is generally captured in all simulations. This behavior is expected as for the case of no crack parallel compression both tensorial damage laws capture all the experienced crack tip stresses. As before the peak load values are the most critical from an analytical perspective when using the Bažant SEL. The simulated peak load values are given in Table 4.2 and are compared against the experimental averages, satisfactory agreement is seen between the simulated and experimental strength across the 3 sizes used.

Based on the accuracy of the $\xi = 0$ simulations corresponding simulations are ran for $\xi = 0.29$ and 0.44. The peak load values from these simulations are given in Table 4.3 and

Simulated Peak Loads (N)				
Size	Hashin Damage	% diff.	Cohesive Elements	% diff.
Small	6477.3	-0.096	6095.5	-0.149
Medium	10632.1	0.071	9394.4	-0.053
Large	13399.4	-0.017	13261.1	-0.027

*Percent difference is calculated against experimental average

Table 4.2 Simulated peak load values for $\xi = 0$ compared against the experimental average.

comparatively plotted in Figure 4.10 and Figure 4.11. As was foreseen in section 4.2, the fully tensorial Hashin damage law predicts a similar trend as the experimental data – as ξ is increased the peak load (i.e., structural strength) decreases. This is possible due to the crack parallel compression being included in the damage initiation criterion of equations (4.3)-(4.6). Also as predicted, the reduced tensorial damage law implemented with cohesive elements is unable to capture the crack parallel compression effects and the reduction in structural strength is not captured.

	Simulated Peak Loads (N)				
	Size	Hashin Damage	% diff.	Cohesive Elements	% diff.
$\xi = 0.29$	Small	6024.6	0.015	6614.4	0.114
	Medium	8007.8	0.032	7925.8	0.021
	Large	12467.5	0.106	13832.2	0.227
$\xi = 0.44$	Small	6559.94	0.167	7450.8	0.326
	Medium	7082.17	-0.067	9389.1	0.236
	Large	11631.4	0.093	14609.8	0.372

*Percent difference is calculated against experimental average

Table 4.3 Simulated peak load values for $\xi = 0.29$ and 0.44 compared against the experimental average.

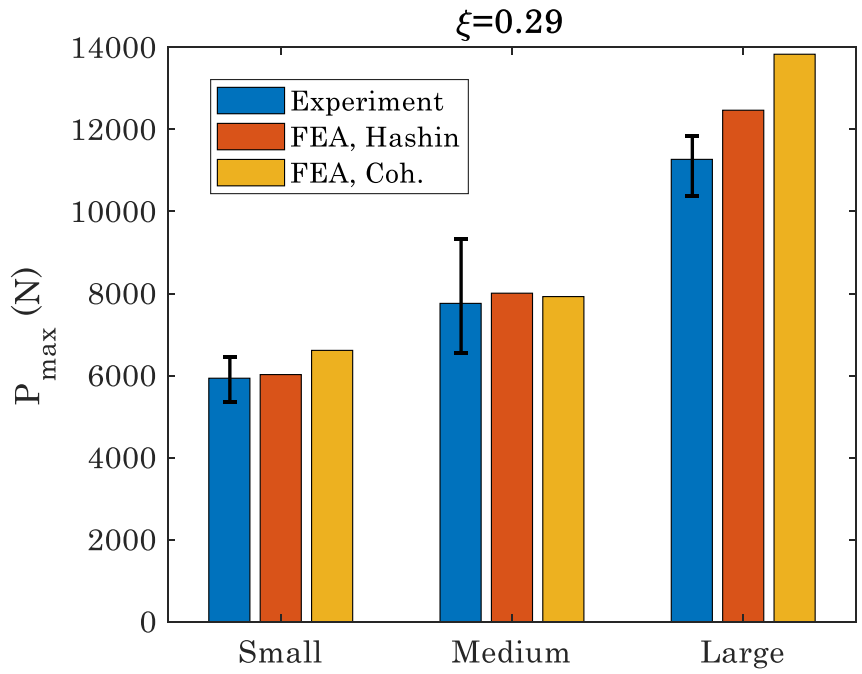

Figure 4.10 Measured peak loads for ξ = 0.29 compared against simulated peak loads.

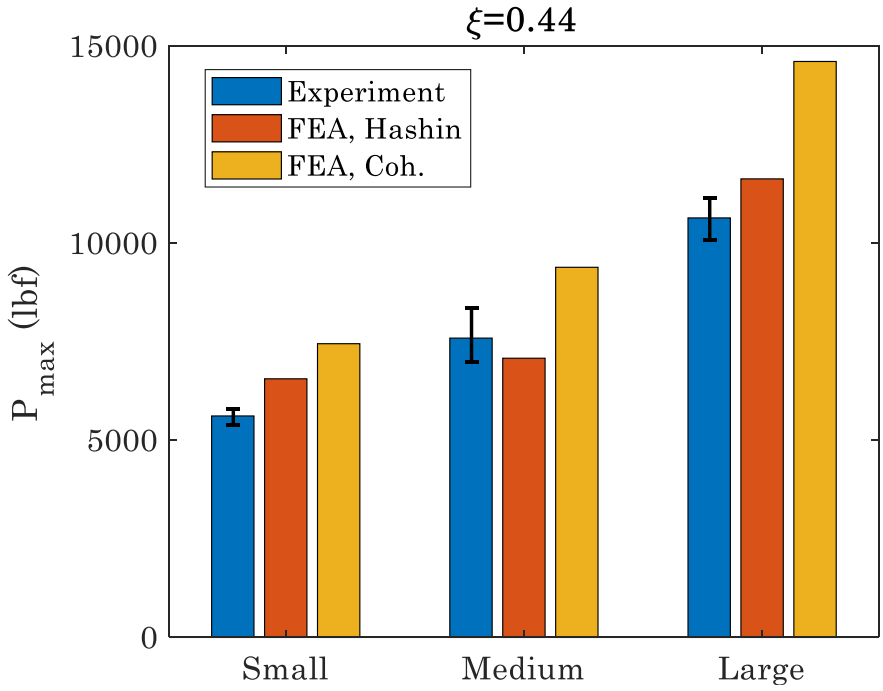

Figure 4.11 Measured peak loads for ξ = 0.44 compared against simulated peak loads.

4.4 Analysis

To analyze the computational results the Bažant SEL is used as the primary analytical tool, as was done with the experimental results in section 3.4. First, the simulated peak load values in Table 4.2 and Table 4.3 are converted to structural strength with equation (3.14). Then using the canonical Bažant SEL in equation (1.2) a linear regression is performed according to equation (3.11) for each simulated ξ level. These regression plots are captured in Figure 4.12 for the Hashin damage simulations and Figure 4.13 for the cohesive element simulations. From the linear regression, equation (3.12) is used to determine the fracture

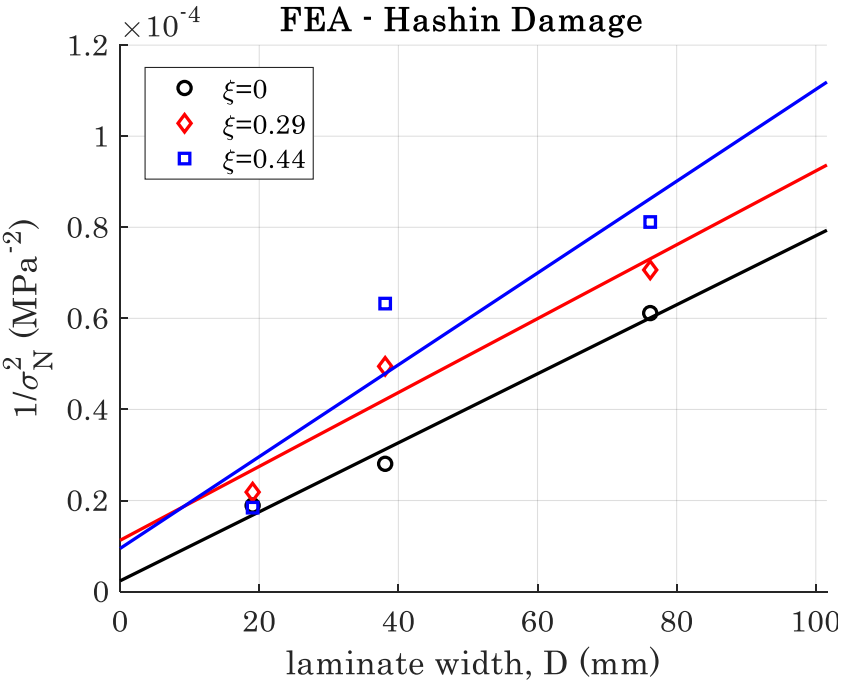

Figure 4.12 SEL linear regression plots for differing simulated ξ values using the fully tensorial Hashin damage law.

energy – which is the ultimately desired parameter for the present study. The calculated fracture energy is tabulated in Table 4.4 and also plotted in a normalized form in Figure 4.14, which includes the previously presented experimental fracture energy. All values are normalized against the experimental ξ = 0 fracture energy.

As seen in Figure 4.14 the fully tensorial damage law predicts the same trend as the experimental data where the fracture energy G_f decreases as ξ increases. This a critical result as it enables this unique behavior of quasi-brittle materials to be captured with existing and simple to implement FEA tools. Although the trend is captured with the fully tensorial damage law, the simulated results do exhibit discrepancies between the calculated experimental fracture energy. This is attributed to error and approximations that are implied by numerical analyses like FEA. For example, discretizing the part geometry into finite elements and the overestimation of stiffness that is inherent to this method [65]. Also, the simulation of the crack with a constant width notch, whereas the crack tip in actuality may be much sharper. And lastly, the FEA model assumes ideal conditions of the composite – perfectly straight fibers, absence of any voids/defects, etc. – which is not true in reality and hence the slight overprediction in fracture energy may be explained by such.

For the reduced tensorial damage law that is invoked with cohesive elements, the weakening effect of the crack parallel compression is not captured. This is a dangerous result as the fracture energy and structural strength is grossly overpredicted. At the worst, for ξ = 0.44 the cohesive element model predicts a fracture energy that is 101% higher than the true value determined experimentally. Also, the cohesive element model generally predicts a constant fracture energy. This spurious result matches the assumption of constant fracture energy per LEFM, and hence incorrect modeling definition is a contributing cause for the structurally weakening behavior of the Gap Test being undiscovered in composites.

	G_f (N/mm)		
ξ	Experiment	Hashin Damage	Cohesive Elements
0	102.85	105.51	111.72
0.29	74.20	98.57	130.07
0.44	64.52	79.32	129.95

Table 4.4 Calculated fracture energy G_f for the simulated Gap Test data using Bažant's Type II Size Effect Law.

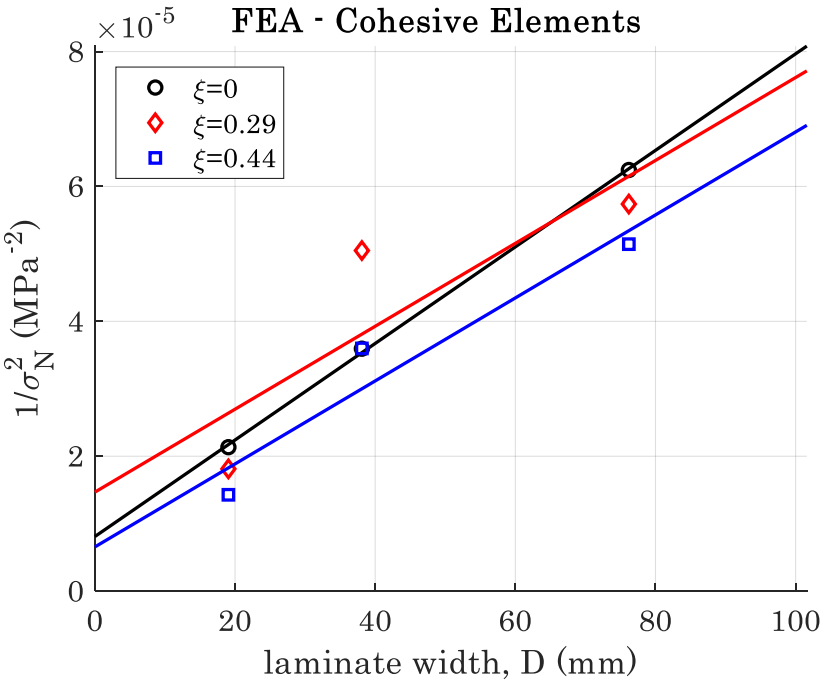

Figure 4.13 SEL linear regression plots for differing simulated ξ values using the reduced tensorial damage law implemented with cohesive elements.

As a salient result these simulations indicate the importance of modeling composites, and all quasi-brittle materials, with a finite width FPZ – done using the crack band approach – and a fully tensorial damage law. In the absence of these two requirements the unique behavior of quasi-brittle materials cannot be captured and furthermore, inaccurate results may lead to concerning overestimations of a structures ability to withstand load in the presence of a crack or defect.

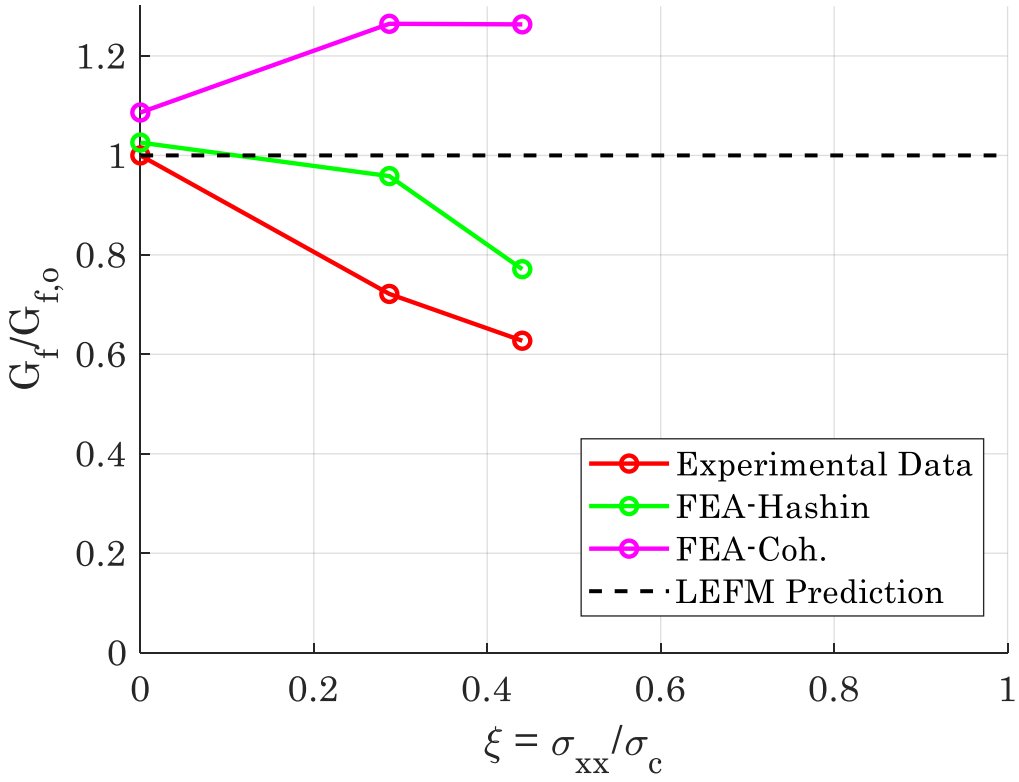

Figure 4.14 Normalized fracture energy plotted as a function of ξ including experimental and simulation results. $G_{f,o}$ is the fracture energy measured for no crack parallel stress which is assumed to be constant per LEFM. Shown fracture energy values are calculated per Bažant's SEL.

4.4.1 Cohesive Size Effect Curve (CSEC) Fitting

The experimental and computational results may also be fit to a cohesive size effect curve to determine the fracture energy G_f, which previous researchers have shown is the asymptotic behavior of the Bažant SEL [53]. Assuming a linear softening law for an isotropic material the following analytical CSEC expression was determined through interpolation of numerical results by [53],

$$\frac{f_t'^2}{g'(\alpha)\sigma_N^2} = \frac{g(\alpha)D}{g'(\alpha)l_1} + \left(1 + 11\sqrt{\frac{g(\alpha)D}{g'(\alpha)l_1}}\right)\left(\beta_o + 25\sqrt{\frac{g(\alpha)D}{g'(\alpha)l_1}}\right)^{-1} \tag{4.10}$$

where g, g', D, and σ_N are as previously defined, f_t' is a measure of material strength, l_1 is a measure of the fracture process zone size (equivalently referred to as Hillerborg's characteristic length [66] and also similar but different in magnitude than the c_f value determined via Bažant's SEL) and $\beta_o = 9(1-\alpha)^4 g'$. Equation (4.10) is amendable to a regression analysis of structural strength σ_N versus structure size D, akin to the regression performed with the Bažant SEL in equation (3.11), albeit the regression is now non-linear. From this non-linear regression the parameters f_t' and l_1 are determined which are used to calculate the fracture energy as shown in equation (4.11).

$$G_f = l_1 f_t'^2 / E \tag{4.11}$$

Performing this non-linear regression results in the fracture energy values shown in Table 4.5 and the familiar normalized fracture energy plot shown in Figure 4.15 for the experimental data, the Hashin damage law simulations, and cohesive elements simulations where equations (4.10) and (4.11) are now used. It is observed that the CSEC results are close and comparable to the results obtained from the Bažant SEL although, the simulated fracture energy values now trend towards behaviors that are more expected. That is, the cohesive element simulations predict a constant fracture energy which is anticipated due to the reduced tensorial damage law that effectively reduces the crack band to a line crack. And, it has been shown based on the logic of Figure 1.4 that a line crack is incapable of considering the influence of a crack parallel compression and hence constant fracture energy is predicted via the simulations. For the fully tensorial Hashin damage law, the simulated fracture energy based on the CSEC expression predicts a strong monotonic decrease in fracture energy, in agreement with the experimental trend, but the magnitude of the simulated fracture energy values is now much closer to the experimental values when compared to the Bažant SEL analysis. Thus, the conclusions drawn from the Bažant SEL and CSEC analysis are identical however, the CSEC expression in equation (4.10) does a superior job of matching the simulated results to the experimental results.

Note that the CSEC expression used presently, which is based on isotropic and linear softening assumptions, is only loosely appropriate for the present study where orthotropic materials are used which exhibit a bi-linear softening behavior. Rederiving equation (4.10) for orthotropic and bi-linear softening materials was not conducted presently due to time

constraints for the author and is left for future works. But, due to the agreement of the calculated fracture energy values from the Bažant SEL (Table 4.4) and the current CSEC expression (Table 4.5) it is likely that such a rederivation of equation (4.10) will not lead to significant changes that would function to impugn the results introduced in this section.

Additionally, the underlying assumptions of cohesive size effect curves are based on cohesive zone modeling (CZM) which is not discussed at length in the present paper due to CZM and CSEC being used only in a very limited capacity from which no unique conclusions are drawn. Nonetheless, work pioneered by Barenblatt initially introduced the cohesive zone model and it is a common fracture mechanics theory that is applied to composites which augments the size effect law which is used extensively here. For detailed definition of cohesive zone modeling the interested reader is directed towards [53, 67, 68].

	G_f (N/mm)		
ξ	Experiment	Hashin Damage	Cohesive Elements
0	112.79	113.51	112.88
0.29	74.42	89.79	112.71
0.44	69.09	77.24	112.88

Table 4.5 Calculated fracture energy Gf for the experimental and simulated Gap Test data using the CSEC expression of equation (4.10).

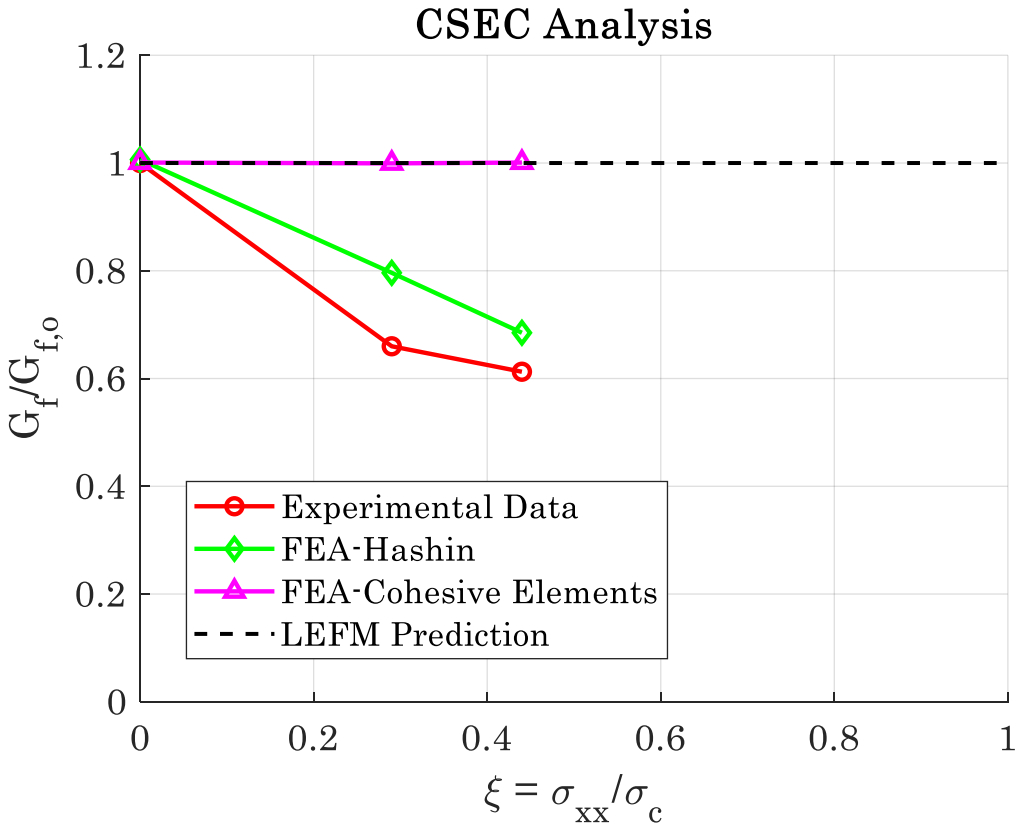

Figure 4.15 Normalized fracture energy plotted as a function of ξ including experimental and simulation results. $G_{f,o}$ is the fracture energy measured for no crack parallel stress which is assumed to be constant per LEFM. Shown fracture energy values are calculated per the CSEC expression in equation (4.10).

Chapter 5 Conclusion

This thesis studied the effect of a crack parallel compression on the global Mode I fracture behavior of a carbon fiber polymeric matrix composite. Which, until the present work, was an area of composite structures completely devoid of study. To accomplish such an avant-garde experimental technique, originally coined elsewhere as *The Gap Test,* was designed, developed, and its nuances thoroughly documented for applicability to composites. To extend the experimental results a computational effort was also undertaken that provides a framework capable of capturing the crack parallel compression effects. Based on these endeavors the following conclusions are made:

1. For cross ply composites the presence of a crack parallel compression leads to a reduction in the structural strength and fracture energy. Specifically, as the crack parallel compression is increased the structural strength and fracture energy monotonically decreases. This weakening effect is explained in three separate but intertwined ways:
2. (1) the Gap Test features 2 distinct, statically determinant loading regimes that unequivocally shows a reduction in peak load when a crack parallel compression is present, i.e., the structures ability to resist fracture is diminished;
3. (2) using photo-microscopy, a clear change in fracture morphology is induced when crack parallel compression precedes a bending, crack opening force. That is, splitting cracks develop at the crack tip which expedite catastrophic crack propagation. For no crack parallel compression splitting cracks are not present at the crack tip and instead fiber breakage and tensile matrix failure are the dominant failure mechanisms – which is the expected response;
4. (3) leveraging digital image correlation to analyze the experimental results, the magnitude of the maximum principal strain field at the crack tip is lesser for the case of crack parallel compression than for no crack parallel compression. Indicating that crack parallel compression causes failure at smaller strain intensities at the crack tip.
5. Composites exhibit a non-negligible fracture process zone that significantly affects their structural behavior in the presence of a crack/defect. This is phenomenological

and hence the line crack assumptions that Linear Elastic Fracture Mechanics are founded upon are inappropriate to apply to composites. Quasi-Brittle Fracture Mechanics are necessary to predict a cracked composites response and specifically, the size effect scaling of structural strength that is inherent to Quasi-Brittle materials must be accounted for.

6. The ability of a crack parallel compression to reduce structural strength indicates that cracks in a composite may open in a non-traditional mode that is not defined by the standard Mode I, II, or III loading. This is explained by the non-negligible fracture process zone which has finite dimensions that are normal to the crack parallel compression force vector.
7. The reduction in the global Mode I fracture energy that is observed experimentally in the Gap Test challenges the century old hypothesis that fracture energy is a constant material property. This complicates the use of fracture energy as a single parameter description of fracture, which is used in many design settings.
8. To computationally capture the effects of crack parallel compression in composites a crack band modeling approach must be used and further, the crack band must be defined by a fully tensorial damage law. If a reduced tensorial damage law is used, that does not allow for the influence of a crack parallel compression, specious results will be obtained that overpredict the true structural strength.
9. The experimental configuration presented in this study is feasible for composites, but the author has 2 main lessons learned to share:
10. (1) the use of lateral stability columns is compulsory for experimental success when loading the thin composite test specimens in compression. Had this design choice been made initially, approximately 4 weeks of experimental development would have been avoided. Stability columns additionally simplify the buckling analysis and permit testing on thinner specimens that are easier to manufacture;
11. (2) lower compressive loads generally lead to less cumbersome testing and analysis as the yield plateau is reached faster, densification of the polypropylene pads is avoided, and damage to the test fixture does not occur. In the Gap Test design phase, the lowest compressive loads that permit testing of the desired ξ values should be used.

Remark

The experiments defined herein demonstrate the criticality of a crack parallel compression, particularly due to the observed weakening effect which would prove very dangerous in a real-world structure. But the results are too limited to immediately warrant drastic changes in composite fracture theory or tools used by practicing engineers. Different layup sequences, material systems, and geometries must be tested and further, the individual effects of crack parallel tension and shear, both in-plane and out-of-plane, need to be evaluated. The behavior under fatigue and mixed mode loading will also require attention, evaluated based on all the aforementioned conditions. Clearly, a substantial amount of resources, financing, and ambitious researchers are necessary to fully define the behaviors observed by the present study.

Bibliography

[1] "Percent Composition," University of Arkansas at Little Rock, 24 May 2020. [Online]. Available: https://chem.libretexts.org/@go/page/50438. [Accessed 29 March 2022].

[2] M. E. Tuttle, Structural Analysis of Polymeric Composite Materials, CRC Press, 2012.

[3] S. Rana and R. Fangueiro, "Advanced composites in aerospace engineering," in *Advanced Composite Materials for Aerospace Engineering*, Woodhead Publishing, 2016, pp. 1-15.

[4] D. Chortis, Structural Analysis of Composite Wind Turbine Blades, Springer, 2013.

[5] A. Elmarakbi, Advanced Composite Materials for Automotive Applications: Structural Integrity and Crashworthiness, Wiley, 2013.

[6] P. Miller and D. Dillon, "The International Sailing Canoe: A Technical Review," *Marine Technology and SNAME News,* vol. 31, no. 04, pp. 296-304, 1994.

[7] C. Ceccato, M. Salviato, C. Pellegrino and G. Cusatis, "Simulation of concrete failure and fiber reinforced polymer fracture in confined columns with different cross sectional shape,," *International Journal of Solids and Structures,* vol. 108, pp. 216-229, 2017.

[8] V. Giurgiutiu, Structural Health Monitoring of Aerospace Composites, Academic Press, 2016.

[9] "Advanced Composites Advance U.S. Air Force Aviation," Sampe, [Online]. Available: https://www.nasampe.org/page/MilitaryAircraft. [Accessed 29 March 2022].

[10] A. Griffith, "The phenomena of rupture and flow in solids," *Philosophical Transactions of the Royal Society of London,* pp. 163-198, 1921.

[11] A. Wells, "The Condition of Fast Fracture in Aluminum Alloys with Particular Reference to Comet," British Welding Research Association Report, 1955.

[12] M. Shank, "A Critical Review of Brittle Failure in Carbon Plate Steel Structures Other than Ships," National Academy of Science-National Research Council, 1953.

[13] J. Duga, W. Fisher, R. Buxbaum, A. Buxbaum, A. Burh, E. Honton and S. McMillan, "The Economic Effects of Fracture in the United States," U.S. Department of Commerce, 1983.

[14] M. Williams and G. Ellinger, "Investigation of structural failures of welded ships," *Welding Journal,* vol. 32, pp. 498-528, 1953.

[15] T. Anderson, Fracture Mechanics: Fundamentals and Applications, 3E, CRC Press , 2005.

[16] Z. Bažant and J. Planas, Fracture and Size Effect in Concrete and Other Quasibrittle Materials, Routledge, 1998.

[17] Z. Bazant, I. Daniel and Z. Li, "Size Effect and Fracture Characteristics of Composite Laminates," *Journal of Engineering Materials and Technology,* vol. 118, no. 3, pp. 317-324, 1996.

[18] Y. Qiao, A. Deleo and M. Salviato, "A study on the multi-axial fatigue failure behavior of notched composite laminates," *Composites Part A: Applied Science and Manufacturing,* vol. 127, 2019.

[19] M. Salviato, K. Kirane, Z. Bazant and G. Cusatis, "Mode I and II Interlaminar Fracture in Laminated Composites: A Size Effect Study," *Journal of Applied Mechanics,* vol. 86, no. 9, 2019.

[20] Z. Bazant, J.-L. Le and M. Salviato, Quasibrittle Fracture Mechanics and Size Effect: A First Course, Oxford University Press, 2021.

[21] M. Salviato, K. Kirane, S. Ashari, Z. Bazant and G. Cusatis, "Experimental and numerical investigation of intra-laminar energy dissipation and size effect in two-dimensional textile composites," *Composites Science and Technology,* vol. 135, pp. 67-75, 2016.

[22] S. Ko, J. Davey, S. Douglass, J. Yang, M. Tuttle and M. Salviato, "Effect of the thickness on the fracturing behavior of discontinuous fiber composite structures," *Composites Part A: Applied Science and Manufacturing,* vol. 125, p. 105520, 2019.

[23] S. Ko, J. Yang and M. Tuttle, "Effect of the platelet size on the fracturing behavior and size effect of discontinuous fiber composite structures," *Composite Structures,* vol. 227, p. 111245, 2019.

[24] Y. Kumagai, S. Onodera, M. Salviato and T. Okabe, "Multiscale analysis and experimental validation of crack initiation in quasi-isotropic laminates," *International Journal of Solids and Structures,* Vols. 193-194, pp. 172-191, 2020.

[25] W. Li, Y. Qiao, J. Fenner, K. Warren, M. Salviato, Z. Bazant and G. Cusatis, "Elastic and fracture behavior of three-dimensional ply-to-ply angle interlock woven

composites: Through-thickness, size effect, and multiaxial tests," *Composites Part C: Open Access,* vol. 4, p. 1000098, 2021.

[26] K. Otsuka and H. Date, "Fracture process zone in concrete tension specimen," *Engineering Fracture Mechanics,* vol. 65, no. 2-3, pp. 111-131, 2000.

[27] Z. Bažant and M. Kazemi, "Size Effect in Fracture of Ceramics and Its Use To Determine Fracture Energy and Effective Process Zone Length," *Journal of the American Ceramic Society,* vol. 73, no. 7, pp. 1841-1853, 1990.

[28] M. Aliha, A. Bahmani and S. Akhondi, "Determination of mode III fracture toughness for different materials using a new designed test configuration," *Materials and Design,* vol. 86, pp. 863-871, 2015.

[29] B. McGinty, "Fracture Mechanics," [Online]. Available: https://www.fracturemechanics.org/modes123.html. [Accessed 30 March 2022].

[30] H. Nguyen, M. Pathirage, G. Cusatis and Z. Bažant, "Gap Test of Crack-Parallel Stress Effect on Quasibrittle Fracture and Its Consequences," *Journal of Applied Mechanics,* vol. 87, no. 7, 2020.

[31] H. Nguyen, M. Pathirage, M. Rezaei, M. Issa, G. Cusatisa and Z. Bazant, "New perspective of fracture mechanics inspired by gap," *PNAS,* vol. 117, no. 25, 2020.

[32] M. Gupta, R. Alderliesten and R. Benedictus, "A review of T-stress and its effects in fracture mechanics," *Engineering Fracture Mechanics,* vol. 134, pp. 218-241, 2015.

[33] Z. Bazant, "Size effect," *International Journal of Solids and Structures,* vol. 37, pp. 69-80, 2000.

[34] "ASTM E399-20a Standard Test Method for Linear-Elastic Plane-Strain Fracture Toughness of Metallic Materials," ASTM International, 2021.

[35] M. Salviato, S. Ashari and G. Cusatis, "Spectral stiffness microplane model for damage and fracture of textile composites," *Composite Structures,* vol. 137, pp. 170-184, 2016.

[36] J. Rice, "A Path Independent Integral and the Approximate Analysis of Strain Concentration by Notches and Cracks," *Journal of Applied Mechanics,* vol. 35, no. 2, pp. 379-386, 1968.

[37] R. Barsoum, "A degenerate solid element for linear fracture analysis of plate bending and general shells," *International Journa for Numerical Methods in Engineering,* vol. 10, no. 3, pp. 551-564, 1976.

[38] E. Barbero, Finite element analysis of composite materials using Abaqus, CRC Press, 2013.

[39] Abaqus, "Eigenvalue Buckling Problem," [Online]. Available: https://abaqus-docs.mit.edu/2017/English/SIMACAEANLRefMap/simaanl-c-eigenbuckling.htm. [Accessed 2 April 2022].

[40] P. Straznicky, M. Worswick and O. Majeed, "Impact Damage in Composite Laminates," *ICCM/9 Composites Behavior,* vol. 5, pp. 386-393, 1993.

[41] Composite Materials Handbook Volume 2 - Revision G, SAE International, 2012.

[42] "ASTM D7264/D7264M-21 Standard Test Method for Flexural Properties of Polymer Matrix Composite Materials," ASTM International , 2021.

[43] "ASTM D695-15 Standard Test Method for Compressive Properties of Rigid Plastics," ASTM International , 2016.

[44] "Composite Materials Research Laboratories," Toray, [Online]. Available: https://www.toray.com/global/technology/organization/laboratories/lab_004.html. [Accessed 5 April 2022].

[45] Composite Materials Handbook Volume 3, SAE International , 2017.

[46] B. Strong, Fundamentals of Composites Manufacturing: Materials, Methods and Applications, Second Edition, Society of Manufacturing Engineers, 2008.

[47] M. Dunn, W. Suwito and S. Cunningham, "Fracture initiation at sharp notches: Correlation using critical stress intensities," *International Journal of Solids and Structures,* vol. 34, no. 29, pp. 3873-3883, 1997.

[48] "ASTM D5045-99 Standard Test Methods for Plane-Strain Fracture Toughness and Strain Energy Release Rate of Plastic Materials," ASTM International, 2014.

[49] K. Willie and A. Naaman, "Fracture energy of UHP-FRC under direct tensile loading," in *FraMCoS-7 international conference*, 2010.

[50] K.-Y. Chang and F.-K. Chang, "A Progressive Damage Model for Laminated Composites Containing Stress Concentrations," *Journal of Composite Materials,* vol. 21, no. 9, 1987.

[51] Z. Bažant and J.-L. Le, Probabilistic Mechanics of Quasibrittle Structures: Strength, Lifetime, and Size Effect, Cambridge University Press, 2017.

[52] S. Tsai and E. Wu, "A General Theory of Strength for Anisotropic Materials," *Journal of Composite Materials,* vol. 5, no. 1, pp. 58-80, 1971.

[53] G. Cusatis and E. Schauffert, "Cohesive crack analysis of size effect," *Engineering Fracture Mechanics,* vol. 76, no. 14, pp. 2163-2173, 2009.

[54] S. Ko, K. Chan, C. Lynch, M. Nguyen, N. Pekhotin, N. Stokes, J. Yang and M. Salviato, "Experimental and Numerical Characterization of the Intra-laminar Fracturing Behavior in Discontinuous Fiber Composite Structures," in *33th ASC Conference*, Seattle, WA, 2018.

[55] R. Talreja, "Assessment of the fundamentals of failure theories for composite materials," *Composites Science and Technology,* vol. 105, pp. 190-201, 2014.

[56] Y. Qiao, Q. Zhang, T. Nakagawa and M. Salviato, "A Size Effect Study on the Splitting Crack Initiation and Propagation in Off-axis Layers of Composite Laminates," in *36th American Society for Composites Conference*, 2021.

[57] T. Okabe, H. Imamura, Y. Sato, R. Higuchi, J. Koyanagi and R. Talreja, "Experimental and numerical studies of initial cracking in CFRP cross-ply laminates," *Composites Part A: Applied Science and Manufacturing,* vol. 68, pp. 81-89, 2015.

[58] J. Rice and G. Rosengren, "Plane strain deformation near a crack tip in a power-law hardening material," *Journal of the Mechanics and Physics of Solids,* vol. 16, no. 1, pp. 1-12, 1968.

[59] Z. Bazant, "Crack Band Model for Fracture of Geomaterials," in *Fourth International Conference on Numerical Methods in Geomechanics*, Alberta, 1982.

[60] Z. Hashin, "Failure Criteria for Unidirectional Composites," *Journal of Applied Mechanics,* vol. 47, no. 2, pp. 329-334, 1980.

[61] R. Lopez, M. Luersen and J. Souza de Cursi, "Optimization of hybrid laminated composites using a genetic algorithm," *Journal of the Brazilian Society of Mechanical Sciences and Engineering ,* 2009.

[62] "Cauchy stress tensor," Wikipedia, [Online]. Available: https://en.wikipedia.org/wiki/Cauchy_stress_tensor. [Accessed 18 April 2022].

[63] "Modeling with cohesive elements," Abaqus, [Online]. Available: https://abaqus-docs.mit.edu/2017/English/SIMACAEELMRefMap/simaelm-c-cohesiveusage.htm. [Accessed 19 April 2022].

[64] "Defining the constitutive response of cohesive elements using a traction seperation description," Abaqus , [Online]. Available: https://abaqus-

docs.mit.edu/2017/English/SIMACAEELMRefMap/simaelm-c-cohesivebehavior.htm. [Accessed 19 April 2022].

[65] T. Hughes, The Finite Element Method: Linear Static and Dynamic Finite Element Analysis, Courier Corporation , 2012.

[66] A. Hillerborg, M. Modeer and P. Petersson, "Analysis of crack formation and crack growth in concrete by means of fracture mechanics and finite elements," *Cement and Concrete Research,* vol. 6, no. 6, pp. 773-781, 1976.

[67] C.-T. Sun and J. Zhihe, Fracture Mechanics Chapter 9: Cohesive Zone Model, Academic Press, 2011.

[68] G. Barenblatt, "The Mathematical Theory of Equilibrium Cracks in Brittle Fracture," *Advances in Applied Mechanics,* vol. 7, pp. 55-129, 1962.